T.R.
BOLU ABANT İZZET BAYSAL UNIVERSITY
INSTITUTE OF GRADUATE STUDIES
DEPARTMENT OF PHYSICS

INVESTIGATION OF CHEMICAL PRESSURE EFFECT ON MAGNETO-ELECTRICAL PROPERTIES IN $La_{1.4}Ca_{1.6}Mn_2O_7$ MANGANITES

DOCTOR OF PHILOSOPHY

NEVİN SOYLU KOÇ

ACADEMIC SUPERVISOR
Prof. Dr. Cabir TERZİOGLU

BOLU, JUNE - 2021

APPROVAL OF THE THESIS

INVESTIGATION OF CHEMICAL PRESSURE EFFECT ON MAGNETO-ELECTRICAL PROPERTIES IN $La_{1.4}Ca_{1.6}Mn_2O_7$ MANGANITES submitted by **Nevin SOYLU KOÇ** and defended before the Examining Committe Members listed below in partial fulfillment of the requirements for the degree of **DOCTOR OF PHILOSOPHY** in **DEPARTMENT OF PHYSICS, Institute of Graduate Studies of Bolu Abant Izzet Baysal University in 21.06.2021** by

Examining Committee Members	**Signature**
Supervisor Prof. Dr. Cabir TERZİOGLU Abant İzzet Baysal University	.....
Member Prof. Dr. Osman GÖRUR Abant İzzet Baysal University	.....
Member Prof. Dr. ÖZTURK Kastamonu University	.....
Member Doç. Dr. Elif AŞIKUZUN Kastamonu University	.....
Member Dr. Ögr. Uyesi Erhan BUDAK Abant İzzet Baysal University	.....

Prof. Dr. Osman GÖRÜR

Director of Instıtute of Graduate Studies

ETHICAL DECLARATION

In this thesis dissertation that was properly prepared according to the Thesis Writing Rules of Bolu Abant İzzet Baysal University of the Institute of Graduates Studies, I hereby declare that;

- All data, information, and documents presented in the thesis were obtained in accordance with the academic and ethical rules,
- All data, documents, assessments, and results were presented in accordance with the scientific ethical and moral rules,
- All works that were benefitted in the thesis were appropriately cited,
- No alteration was made in the data used,
- Study presented in this thesis is original,

Otherwise, I declare that I accept the loss of all my rights in case any contradiction that may arise against me.

Based on the plagiarism report that was generated on the date of 29/07/2021 by using predetermined filtrations set by Directorate of Institute of Graduate Studies of the Turnitin programme, a plagiarism detection sofware, the rate of plagiarism detected was 25 %.

_____

Nevin SOYLU KOÇ

ABSTRACT

INVESTIGATION OF CHEMICAL PRESSURE EFFECT ON MAGNETO-ELECTRICAL PROPERTIES IN $La_{1.4}Ca_{1.6}Mn_2O_7$ MANGANITES
PHD THESIS
NEVİN SOYLU KOÇ
BOLU ABANT IZZET BAYSAL UNIVERSITY
INSTITUTE OF GRADUATE STUDIES
DEPARTMENT OF PHYSICS
(SUPERVISOR: PROF. DR.CABİR TERZİOGLU)

BOLU, JUNE 2021
xv + 115

In this study, a detailed study was done about the doped-layered perovskite structure under the influence of chemical pressure as the formation of $(La_{1-y}RE_y)_{1.4}Ca_{1.6}Mn_2O_7$. The effect of chemical pressure was examined by altering the A-site radius, $\langle r_A \rangle$, by doping with the Rare Earths (RE) (Gd, Sm, Nd, Pr) in different proportions (y) and three series of compounds were prepared, with three different $\langle r_A \rangle$, 1.3213, 1.3353, 1.3423 Å, by solid-state reaction method.
The micro-structural characterization was studied by using X-ray powder diffraction (XRD), Rietveld structural refinements, scanning electron microscopy and X-ray analysis (EDX). The electrical transport properties were determined in the temperature range of 5-300 K under a 0.4 T magnetic field. The metal-insulator (M-I) transition temperature (T_{M-I}) and magnetoresistance (MR) values were determined. The A.C susceptibility measurements were performed to obtain the ferromagnetic (FM)-antiferromagnetic (AFM) phase transition temperature (Tc).
All samples were crystallized in the *I4/mmm* space group in the tetragonal structure and a nonlinear increase in unit cell volume with increasing $\langle r_A \rangle$. The particle size distribution is almost homogenous and the EDX spectrum confirmed that all elements present in all samples without any loss of integrated elements. All samples execute the typical M-I and FM-AFM phase transition and with increasing $\langle r_A \rangle$, T_{MI} and Tc shift towards higher values. The largest MR (55.09 % at 73K) was observed on the LPCMO material within the group with the smallest $\langle r_A \rangle$.
The results indicated that the chemical pressure could affect electromagnetic transfer properties by altering the strength of the carrier localization effect.

KEYWORDS: Double layered manganites, Chemical Pressure, Electro-magnetic transport, Magnetoresistance.

ÖZET

$La_{1.4}Ca_{1.6}Mn_2O_7$ MANGANİTLERDE KİMYASAL BASINCIN MANYETO-ELEKTRİKSEL ÖZELLİKLER ÜZERİNDEKİ ETKİSİNİN İNCELENMESİ
DOKTORA TEZİ
NEVİN SOYLU KOÇ
BOLU ABANT İZZET BAYSAL ÜNİVERSİTESİ
LİSANSÜSTÜ EĞİTİM ENSTİTÜSÜ
FİZİK ANABİLİM DALI
(TEZ DANIŞMANI: PROF. DR. CABİR TERZİOGLU)

BOLU, HAZİRAN - 2021
xv+ 115

Bu çalışmada katkılı-tabakalı perovskit yapılarda $(La_{1-y}RE_y)_{1.4}Ca_{1.6}Mn_2O_7$ formunda kimyasal basınç etkisi ele alınmıştır. Kimyasal basıncın etkisi, farklı oranlarda (y) bazı nadir toprak elementleri (RE) (Gd, Sm, Nd, Pr) ile doping yapılarak A-bölgesi yarıçapı $\langle r_A \rangle$ değiştirilerek incelenmiş ve katıhal reaksiyon yöntemi ile üç seri bileşik hazırlanmıştır. Her bir serinin yarıçapı 1.3213, 1.3353, 1.3423 Å olarak belirlenmiştir.

Mikro yapısal karakterizasyon için, X-ışını kırınımı (XRD), Rietveld yapısal analizleri, taramalı elektron mikroskobu ve X-ışını analiz (EDX) ölçümleri yapılmıştır. Metal-Yalıtkan (M-I) geçiş sıcaklığı (T_{M-I}) ve manyetoresistans (MR) değerlerini belirlemek için 0.4 T manyetik alan altında 5-300 K sıcaklık aralığında direnç-sıcaklık ölçümleri yapılmıştır. Ferromanyetik(FM)-antiferromanyetik (AFM) faz geçiş sıcaklığını (Tc) elde etmek için A.C duyarlılık ölçümleri yapılmıştır.

Tüm numunelerde, tetragonal yapıda *I4/mmm* boşluk grubunda kristalizasyon vardır. Birim hücre hacimleri artan $\langle r_A \rangle$ ile lineer olmamakla birlikte bir artış göstermiştir. Partikül boyutu dağılımı homojendir ve EDX spektrumu, tüm elementlerin tüm numunelerde herhangi bir kayıp olmaksızın mevcut olduğunu doğrulamıştır. Tüm örnekler tipik M-I ve FM-AFM faz geçişini gerçekleştirir ve daha büyük $\langle r_A \rangle$ yarıçaplı gruplarda T_{MI} ve T_C değerlerinin yüksek değerlere kaydığını gözlemleyebiliriz. En büyük MR değeri (73K'da% 55.09), en küçük $\langle r_A \rangle$ değerine sahip grup içindeki LPCMO örneğinde gözlendi.

Sonuçlar, kimyasal basıncın taşıyıcı lokalizasyon etkisinin gücünü değiştirerek elektromanyetik transfer özelliklerini etkilediği şeklinde yorumlanabilir.

ANAHTAR KELİMELER: Çift tabakalı manganitler, Kimyasal Basınç, Elektro-manyetik Geçiş, Manyetodirenç.

TABLE OF CONTENTS

LIST OF FIGURES

Page

LIST OF TABLES

Page

LIST OF ABBREVIATIONS AND SYMBOLS

A.C **:** Alternating Current

AE : Alkaline Earth

AFM **:** Antiferromagnetic

CAF **:** Canted Antiferromagnetic Phase

CE **:** Charge-Exchange

CFS **:** Crystal Field Splitting

CMR **:** Colossal Magnetoresistance

CO **:** Charge Order

DE **:** Double Exchange

DL : Double-layer

EDXS : Energy-Dispersive X-Ray Spectroscopy

EDX **:** Energy-Dispersive X-Ray Spectroscopy

FM **:** Ferromagnetic

GMR **:** Giant Magnetoresistance

JT **:** Jahn -Teller

M-I **:** Metal-Insulator

MR **:** Magnetoresistance

MRAM **:** Magnetoresistive Random Access Memory

OO **:** Orbital Order

OMR :Ordinary Magnetoresistance

PM : Paramagnetic

RE **:** Rare Earths

RP : Ruddlesden –Popper

TMR **:** Tunneling Magnetoresistance

XRD **:** X-Ray Diffraction

M ***:*** Magnetization

χ **:** Magnetic Susceptibility

ACKNOWLEDGEMENTS

The author wishes to express his deepest gratitude to her supervisor Prof. Dr. Cabir TERZİOGLU for his guidance, advice, criticism, encouragement, and insight throughout the research.

The author would also like to thank Dr. Sevgi POLAT ALTINTAŞ for her suggestions and comments.

The author would like to express her endless thanks to her FAMILY, whose moral support she always felt.

This study was supported by the funding of Bolu Abant Izzet Baysal University, Grant No: 2017.03.02.1238 research project.

1. INTRODUCTION

The various studies from the 1950s to the present day have revealed that perovskite manganites have a wide range of physical and structural properties (superconductivity, ferroelectricity**,** and enormous magnetic resistance). These are materials that can be used in many topical areas, such as information technology, for further storage and processing of digital information. They are also at the centre of a new science: spin electronics or spintronic. In addition to the technological applications that these compounds have studied are being carried out all over the world to understand and develop the complex structure of these materials. Their properties are tried to be explained with a wide variety of physical phenomena, i.e., superconductivity, ferroelectricity, huge magnetoresistance. Among these materials, which are classified as very interesting, magnetoresistive manganites are currently the subject of much of the work in the concentrated substance community and are gaining more and more popularity compared to cuprate-superconducting. Identification of various basic physical concepts in these compounds and an in-depth understanding of transitions (ferromagnetism-FM, anti-ferromagnetism-AFM, charge order-CO, orbital order-OO, isotopic effects, metal/insulator-M/I transition) are still a major challenge for solid-state physicists.

The original Perovskite mineral ($CaTiO_3$) was first discovered and named by Gustav Rose in 1839 to dedicate Russian mineralogist LevPerovski (1792-1856) (1).

The perovskite is a common class of oxide materials and has the general formula ABX_3, where “A is usually an alkali earth (Ca, Sr, Ba, ...) or a rare-earth (La, Gd, Pr, Sm, ...) and B could be 3d, 4d, and 5d transitional metal elements (Mn, Fe, Co, Ti, ...) and “X” is an anion such as (O, F, Cl) and was firstly identified by Jonker and van Santen. If B is a manganese atom, the compound is also called “Manganites” (2).

Among the manganites, the mixed valance perovskites are the most interesting and technologically advanced ones as the chemical composition of $RE^{+3}_{1-x}AE^{+2}_{x}MnO_3$. Here, RE is present as a generally trivalent rare earth element (La, Ce, Pr, Sm, Nd, Gd, Eu etc) and divalent alkaline earth ions for AE (Sr, Ca and Ba). The larger-sized RE trivalent ions and AE divalent ions are located in the A-side of perovskite with a 12-fold coordination number. The smaller Mn ions, (a mixed form of Mn^{3+}-Mn^{4+}) occupy the B region at the centre of an oxygen octahedron, with 6-fold coordination.

These materials could be used in many research fields such as information technology, with a huge capacity for digital information, magnetic storage cells for magnetoresistive random access memory (MRAM) (3), thermal or infrared detectors for use in infrared bolometers (4), new materials in photo / X-ray detectors (5) and; spin electronics or spintronics (6), a new scientific discipline. This field relies on the use of electron spin rather than its characteristic charge for conventional electronics. This practice led to the realization of revolutionary applications in today's technology world with the discovery of giant magnetoresistance (GMR) in the late 80's. (7).

The authors discovered that by replacing the Lanthanum with a divalent cation, it is possible to change the physical properties of these materials. And indeed, depending on the substitution rate, these materials can be insulators, semiconductors or even metal. Depending on the degree of displacement, they may also be ferromagnetic or antiferromagnetic.

There is a strong correlation between the electronic transport properties, the magnetic properties, and the crystal structure of these compounds. One of the most striking properties is the value of the Mn-O-Mn angles, which can promote or prevent ferromagnetic interactions through the double-exchange mechanism (8,9). The other important factor that determining physical properties is the average size of cations in the A-site, $\langle r_A \rangle$. For example, the antiferromagnetic insulating character dominates in systems with a low $\langle r_A \rangle$ value (case, for example, compounds Y/CaMnO3) where the ferromagnetic conductive character is

predominant in the systems with a large $\langle r_A \rangle$. (In the case of La/BaMnO3 compounds) (10,11).

A lot of profound studies were also been studied for the other variations of perovskites manganites compounds that are named as the Ruddlesden –Popper (RP) family of the $A_{n+1}Mn_nO_{3n+1}$. The double-layer (DL) RP phase, with *n*=2 members along the c-axis of an iterative layered as a double layer of (MnO_2), inserted between two single layers of a non-magnetic mixture of (AO) (A alone could be La, Sr, Ca or a mixture of them). The layered perovskite manganites can be regarded as a natural "ferromagnetic metal layer-insulator layer-ferromagnetic metal layer" (9),(12).

While cubic perovskites (*n*=∞) have a three-dimensional (3D) crystal structure, layered manganites have a quasi-two-dimensional (2D) crystal structure, and are distinctly from 3D manganites. RP phase displays a two-dimensional Mn-O-Mn network and anisotropic magnetotransport properties (9). Accordingly, the properties of DL manganites are extremely sensitive to the change in magnetic field, internal or external pressures. These interesting features of these materials allow the technology to be applied in some systems or storage technology, spin-based devices, magnetic sensors, and bolometers (9,12).

Unlike simple ABO_3 perovskite materials, layered perovskite materials have high sensitivity to very small changes in structure and composition due to their anisotropic structure formed by the nature of layered materials (Hur, 1998).

Besides, the number of *n* layers and the differences of the elements separating the layers greatly change the physical properties. In a study by Moritomo et al., They found that $La_{1-x}Sr_{1+x}MnO_4$ manganite compound having n = 1 layer number and K_2NiF_4 type layered perovskite structure has 2-dimensional antiferromagnetic and insulating properties (Moritomo, 1995). In another study by Mohan Ram et al., They found that $La_{2-2x}Sr_{1+2x}Mn_2O_7$ compound having n = 2 layer perovskite structure has conductive and ferromagnetic properties (Mohan Ram,1988).

Doping by different doping elements or changing doping concentration is one of the ways that tune the structure of manganites. This process induces on the A-site atom size $\langle r_A \rangle$ and so affects the structure by causing to change in the bandwidth (13)(14). Any change on A-site atom size $\langle r_A \rangle$ causes a mismatch between the A-site and Mn site ion size, and therefore the magnetic ordering changes (15,16).

Some different results have been reported in the literature regarding the determination of the structure of layered perovskite manganites by the XRD method. In the study conducted by Asano (1996) et al., the structure of the $La_{1.5}Ca_{1.5}Mn_2O_7$ compound was examined by the Rietveld treatment method and it was shown that the structure had tetragonal symmetry (17). In the following years, Guangly (2000) and his colleagues brought criticism to this study and stated that the structure has orthorhombic symmetry in their own XRD treatment.

Intensive studies have also been performed for the other variations of perovskites manganites compounds that are named as the Ruddlesden –Popper (RP) family of the $A_{n+1}Mn_nO_{3n+1}$ (18). The double-layer (DL) RP phase, with *n*=2 members along the c-axis of an iterative layered as a double layer of (MnO_2), inserted between two single layers of a non-magnetic mixture of (AO) (A alone could be La, Sr, Ca or a mixture of them). The layered perovskite manganites can be regarded as a natural "ferromagnetic metal layer-insulator layer-ferromagnetic metal layer" (19–21).

The subject of this work is the double perovskite manganites structure with the basis of Lanthanum (La) and Calcium (Ca) as a form of $La_{1.4}Ca_{1.6}Mn_20_7$ which is prepared by conventional solid-state reaction method. In this study, we aim to investigate the chemical pressure effect which is varied by changing the mean A-site radius, $\langle r_A \rangle$, substituting different rare-earth ions with La. The Rare Earths are chosen as Gd, Sm, Nd and Pr of in Lanthanides in the chemical composition of $(La_{1-y}RE_y)_{1.4}Ca_{1.6}Mn_20_7$ and we get three different $\langle r_A \rangle$ which is 1.3213, 1.3353, 1.3423 (Å) via different variations of (y) fractional ratio. The structural and electro-magnetic transport properties were investigated in the doped perovskites $La_{1.4}Ca_{1.6}Mn_20_7$ manganites.

2. AIM AND SCOPE OF THE STUDY

Our goal in this work is to carry out research to improve the properties of these materials for their application areas in technology.

The presented systems have been carefully chosen to meet the need for understanding the phenomena encountered in the study of the compounds of this thesis

The thesis dissertation is presented in four main chapters. In the first three titles, it has been tried to give a basic theoretical background for the thesis topic as the detailed presentation of the chemical, electronic, structural, and magnetic composition of single and double perovskite manganites. The various magnetic couplings, exchange interactions and properties as well as main models (metal-insulator transition, magnetoresistance, etc.) of these compounds have been presented in detail.

In the experimental part, the different characterization techniques used in this thesis. For the structural study, the X-ray diffraction technique was presented in detail. For the microstructure and the study of the purity of the compounds elaborated, a presentation of the scanning electron microscopy has been shown. The magneto-transport characterization was carried out by the four-point technique using a cryostat equipped with a superconducting system to produce the magnetic field.

In the third part, we present and analyze the experimental results. In the first part of this section, the structural and microstructural analyses were presented. In the second section the magneto-electrical analysis was performed.

In the fourth part; the results and analyzes of the experimental studies are presented. The results were tried to be correlated with each other. The best features of our samples were tried to be determined.

Thesis work; It is aimed to increase the applicability of manganite materials, which have many new technological application areas in technology and to be useful for new studies.

3. PEROVSKITE MANGANITES

Structurally there are three types of manganese compounds namely Perovskite manganites, layered manganites and pyrochlore manganites (18), (22),(23,24).

The perovskite is a common class of oxide materials that has the general formula ABX_3, where "A is usually an alkali earth (Ca, Sr, Ba, ...) or a rare-earth (La, Gd, Pr, Sm, ...) and B could be 3d, 4d, and 5d transitional metal elements (Mn, Fe, Co, Ti, ...) and "X" is an anion such as (O, F, Cl) and was identified by Jonker and van Santen (25,26).

In general, Perovskites have a cubic structure with a space group of $Pm\bar{3}m$, (except mineral Perovskite $CaTiO_3$); central position is occupied by the A-site cation (La) (0,0,0); the body-centred positions the B ions (Mn, Co) sits (1/2, 1/2, 1/2), sits inside an octahedral cage of oxygen octahedron and the anion O, Oxygen (X) is at face-centred positions (1/2, 1/2, 0) and bonds them together as shown in Figure 3.1. The ionic radius of an atom is larger than the ionic radius of B. In the ideal perovskite structure, A cation is in 12-fold Cubo- octahedral coordination, 6-fold coordinated B ions and 2-fold coordinated O ions (27).

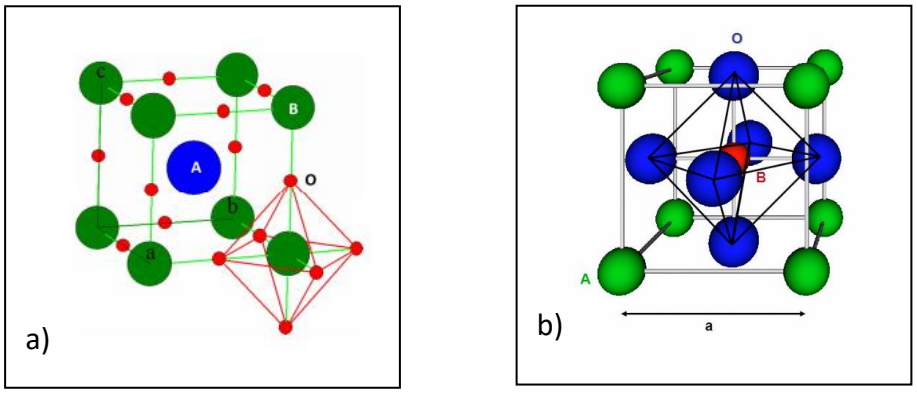

Figure 3. 1. Schematic view of cubic perovskite structure of ABO_3 a) Central position is occupied by the A-site cation with corner-sharing BO_6; b) BO_6 octahedral sits inside an octahedral cage of oxygen octahedron and the anion O.

Manganites ($REMnO_3$) with Rare Earth elements La for A site, $LaMnO_3$, it is called “Lanthanum Manganite” with three dimensional (Mn-O-Mn). Most of the electrical, optical, and magnetic properties of perovskite manganites inspire by the octahedral structure formed by 6 Oxygen ions located around Mn ions (Figure 3.1.b). This structure is in the form of a 3-dimensional bond formed by the Oxygen ions in the corners with the B region ion in the centre and BO_6.

3.1 Electronic Structure of Perovskite Manganites

To understand the transport mechanism in manganites, we must consider the electronic configuration. Firstly, Manganese (Mn) is a transition element with the outer electronic configuration of five $3d^5$ $4s^2$ with degenerate 3d and 4s levels, and its atomic number is 25. In nature it is not found as a free element, generally occurs in the Mn (II), Mn (III), Mn (IV), oxidation states (28).

The 5 orbital states on 3d shell are breached down of degeneracies of as the ↑-spin e_g and ↓-spin t_{2g} lover-energy sub-bands due to a static electric field produced by a surrounding charge distribution (anion neighbours). Since the electrons have to spend more energy to settle in the *eg* band, they fill firstly the t_{2g} band. Without any substitution of the form $REMnO_3$ phase, the cations RE and Mn exist in a +3 oxidation state. When we substitute a part of RE site with a divalent cation (usually an alkaline –earth or alkaline element) the doped material results in a mixed composition with general formula $(RE^{3+}_{1-x}AE^{2+}_{x})(Mn^{3+}_{1-x}Mn^{4+}_{x})O^{2-}_{3}$ (RE = La^{+3}, Pr^{+3}, Nd^{+3}, etc.; AE = Ca^{2+}, Sr^{2+}, Ba^{2+}, etc.). These materials are called also “mixed-valent manganites” since Mn ions are formed both Mn^{3+} and Mn^{4+} in a mixed-valence state in region B (29).

It should be noted that the A- B cations of ABO_3 must allow the electroneutrality of the compound, that is, the sum of the charges of cations A and B must be equal to the total charge of the anions. There are three types of triple oxides: A cation, monovalent ($A^{1+}B^{5+}$ O_2^{-3}), divalent ($A^{2+}B^{4+}O_2^{-3}$) or trivalent (A^{3+} $B^{3+}O_2^{-3}$).

For example, the chemical formula of the compound is formed in the case of the addition of x amount Ca^{2+} instead of valence La^{3+}, the compositions become

like $(La^{3+}_{1-x}Ca^{2+}_{x})$ $(Mn^{3+}_{\alpha}Mn^{4+}_{\beta})O_3^{-2}$. Where α indicates the amount of Mn^{+3} ion to be formed by addition, β is the amount of Mn^{+4} ions and x is the amount of doping (30).

When we write the conservation of the charge statement to determine these quantities,

$$(1-x).(+3)+x.(+2)+\alpha.(+3)+\beta.(+4)+3(-2)=0 \quad (3.1)$$

And for 1mole of B-site;

$$(\alpha+\beta)=1 \quad (3.2)$$

Using Equation (2.1) and Equation (2.2), α = 1-x and β = x is found.

And so, the chemical formula of the manganites becomes a mixed valency as shown below when 2+ cation is substituted.

$$(La^{3+}_{1-x}Ca^{2+}_{x})(Mn^{3+}_{1-x}Mn^{4+}_{x})O_3^{2-} \quad (3.3)$$

This result can be interpreted as follows: by displacing 3+ rare-earth elements with some 2+ valence elements, Mn^{+4} ions occur of as much as the amount of 2+ valence elements. This causes a change of the electric charge on the A site is compensated by Mn cations. It means that a part of Mn^{3+} (equal to x) converts in Mn^{4+} valance state. We can say that the interesting physical properties are seen in perovskite manganites are precisely attributed to these Mn^{3+} and Mn^{4+} balances.

If no alkaline element is added to the Lanthanum side, i.e., x = 0 (Mn^{3+}:$4s^0 3d^4$) perovskite manganite structure as a form as 3d shell with four elements ($3d^4$) and each manganese is surrounded by six O^{-2} ($La^{3+}Mn^{3+}O_3^{-2}$). In this case, the Mn ion has 4 unpaired electrons in the 3d orbital. In contrast to this case, when the structure is completely doped with an alkaline element, in the case of x=1, perovskite manganite structure is in the form of ($AE^{2+}Mn^{4+}$ O_3^{-2}) and all the manganese atoms in the structure are in the state of Mn^{4+} with 3 electrons in 3d shell. (Mn^{4+}:$4s^0 3d^3$). Both x=0 and x=1 situation shows antiferromagnetic properties corresponding because the total magnetic moments of the electrons which the outermost shell of Mn atoms located in 3d, are zero.

3.2 Structure of Ruddlesden-Popper (RP) Perovskite Manganites

The other variation of Perovskite manganites is the Layered Perovskite Manganites that have the general formula as $A_{n+1}B_nO_{3n+1}$ is related to the member of the series of Ruddlesden-Popper (RP) phases. The RP phase is based on comprised of *n* sequential two-dimensional perovskite-like layers (ABO_3) are sandwiched between two rock-salt layers (AO) along the crystallographic ***c***-axis direction. "*n*" varies from 1 to ∞. Its formula can be reformed like $(AO)(ABO_3)_n$, where *n* represents the number of connected peak corner layers sharing BO_6 octahedra (31). (Figure 3.2.)

This type of manganite generally crystallizes in the space group *I4/mmm* of the tetragonal system. In layered compounds, the c-axis is perpendicular to the layers, and the a and b axes are parallel to the layers. The first member of the RP family *n*=1 monolayer is (AO) ($AMnO_4$) with only one layer of corner-sharing MnO_6 octahedral along the c direction. With *n*=2 double-layered manganese-based (AO) $[(AMnO_3)]_2$ can be thought as of double layers MnO_6 octahedra, along the c axis separated by the rock salt type AO layers. The schematic view of the crystal structure of the Ruddlesden-Popper series of manganites is shown in Figure 3.2. n=∞ has an infinite number of layers of MnO_6 with the cubic perovskite structure. In the regime where the monolayer is insulating and the n=∞ layer is metallic, the double layer has an intermediate behaviour, with insulating properties above a critical temperature and metallic below (32).

In this study we will discuss on for n=2 layer of $(La,Ca)_3Mn_2O_7$ in the special case of $(La,RE,Ca)_3Mn_2O_7 \longrightarrow (La_{1-y}RE_y)_{1.4}\ Ca_{1.6}\ Mn_2O_7$ (RE: Gd^{3+} ,Sm^{3+} ,Nd^{3+} ,Pr^{3+}).

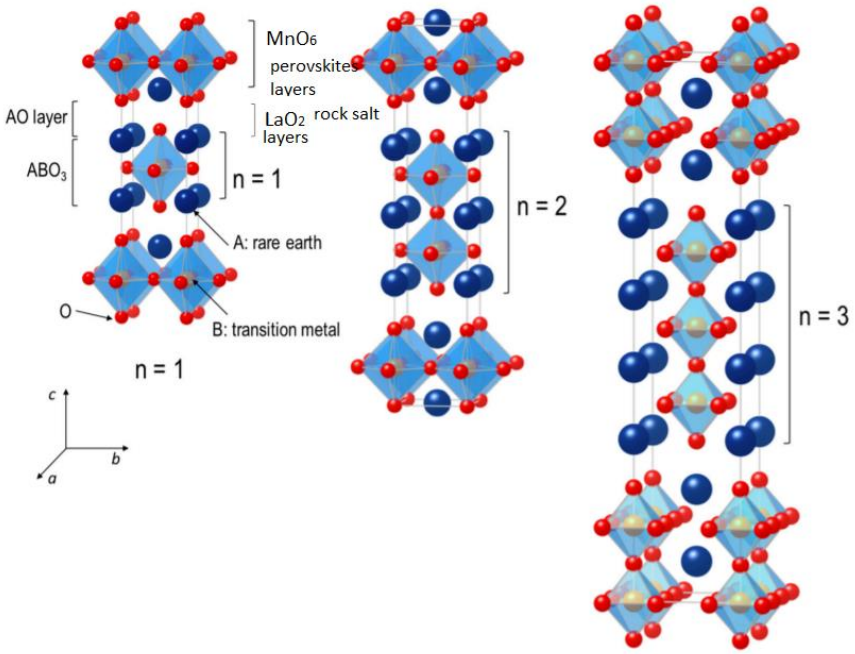

Figure 3. 2. Schematic crystal cell-structure of Ruddlesden-Popper oxides for n=∞ has an infinite number of layers of BO_6, (MnO_6), to the cubic perovskite structure; n=1 (AO)($AMnO_4$) with only one layer of corner-sharing MnO6 octahedral; n=2 (AO) $[(AMnO_3)]_2$ can be thought as of double layers MnO_6 octahedra (33).

3.3 The Distortions of the Perovskites Structure

Perovskite structures often deviate from the ideal structure in different ways as a distortion of the unit cell (elongation in a certain crystallographic direction) shift of the A-ion from the centre of the cuboctahedron, the B-ion from the centre of the octahedron; rotation of octahedrons around an axis; deformation of octahedral.

3.3.1 Distortions Due to Size Effects: Goldschmidt Factor and Stability of the Structure

The substitution with different cations or anions at different sites entails deformations of the perovskite structure and hence changes the crystal parameters of the structure. For example, the ideal cubic crystal structure of ABO_3 is, however, can be formed as orthorhombic and tetragonal Bravais lattices by filling the different radii of RE and AE ions as distortions of the oxygen octahedral. Rare-

earth ions (La, Gd and Dy etc.) with large ionic radius can crystallize in an orthorhombic structure (distorted perovskite) while small ionic radius rare-earth ions (Ho-Lu and Y, Sc) show hexagonal crystal structure. The distortion of the structure is commanded by a geometric factor, the Goldschmidt Tolerance factor (34,35).

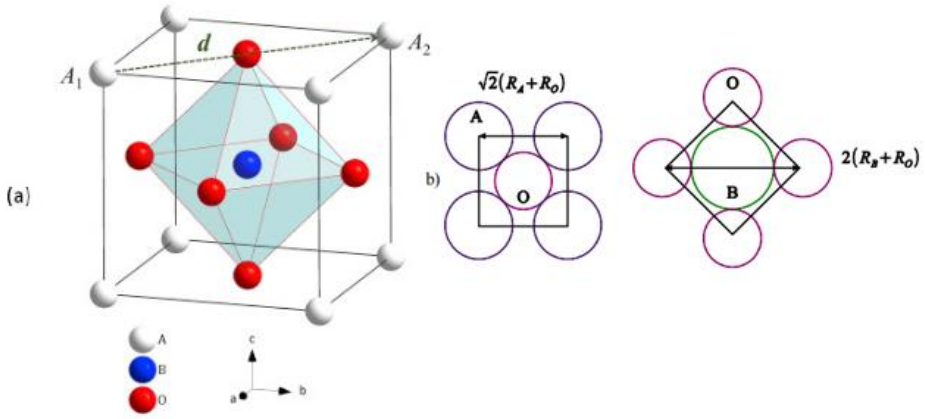

Figure 3. 3. The schematic diagram for an ideal cubic perovskite structure for equilibrium bond lengths.

In the ideal cubic perovskite structure, the equilibrium bond lengths between the A, B and O ions have the ratio $d_{A-O}/d_{B-O} = \sqrt{2}$, where $d_{A-O}$is the distance between the A site and the nearest oxygen ion, and d_{B-O} is the distance between the B site and the closest oxygen ion (Figure-3.3). In the ionic model, the bond lengths are defined by the ionic radii and where this equation forms as $(r_A + r_O)/(r_B + r_O) = \sqrt{2}$ where, $\langle r_A \rangle$, $\langle r_B \rangle$ and r_O are the average A-site, average B-site cation and anion ionic radii (purely ionic bonding is assumed) respectively (36,37).

$$t = \frac{(<r_A>+r_O)}{\sqrt{2}(<r_B>+r_O)} = \frac{d\langle A-O\rangle}{\sqrt{2}\, d\,\langle B-O\rangle} \tag{3.4}$$

$$\langle r_A \rangle = \sum_i x_i\, r_i \tag{3.5}$$

r_i is the ionic radius of the cation *i*, x_i is the occupancy fraction of the cation *i* with radius r_i.

We can say that this factor characterizes the qualification between the two sub-networks "AO" and "BO". The perovskite structure is stable when 0.75 <t <1.02. The structure would be undistorted, ideally cubic, t=1, when the A-site cation was to exactly fill the interstice and the Mn-O-Mn bond angle would be 180° as illustrated in the figure. When small A-site cations are selected, $d_{(A-O)}$ decreases; the A atom is too small for the structure and cannot effectively bond with neighbouring O atoms and oxygen move to the centre. This leads to phases with tilts of the oxygen octahedra or A-type driven ferroelectricity. The tolerance factor becomes smaller than one, t<1, Mn-O-Mn bond angle gets smaller than 180° and as θ decreases, the electron hopping amplitude is reduced, and the material becomes less conductive. The reason is that; the overlap between manganese *d* and oxygen *p*-orbitals decreases thereby weakens the Double Exchange (DE) interaction between Mn ions and oxygen ions that localization of charge carriers (38).

Different types of structures are distinguished according to the value domains of the Goldschmidt factor. We can summarize as the structure is as a form when t<0.75 ilmenite (titanium-iron oxide mineral with the idealized formula FeTiO3); for the scale of 0.75<t<0.96 orthorhombic distortions; 0.96 <t <0.99 rhombohedral distortions; t >1.06 hexagonal distortion. When the tolerance factor is t>1 this means that; B atom is too small for the oxygen octahedron and so the B atom has the freedom to move. These perovskites tend to be B-type ferroelectrics as a small polar distortion is developed. As a result of these, we can say chemical substitution may tilt and strengthen the oxygen octahedrons. It is through the oxygen in the structure to give the electron mobility feature. The Mn-O-Mn angle is a very important factor for the structure and determines its characteristic properties. Electron transfer through oxygen is known as double-exchange interaction (39).

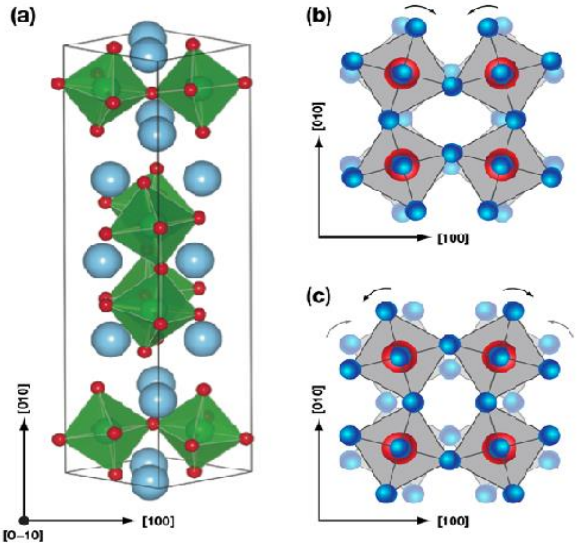

Figure 3. 4. $Ca_3Mn_2O_7$ structure in its distorted ferroelectric state. Mn ions (green) are surrounded by oxygen octahedra (green with red O ions) with Ca ions (blue) interspersed. (b) Octahedral rotation (R) in $Ca_3Mn_2O_7$, showing the oxygen (blue) and manganese (red) sites. The undistorted structure is shown in grayscale. (c) Octahedral tilt (T) of the same. The combination of the tilt and rotation combine to produce ferroelectric order (40).

3.3.2 Distortions of Electronic Origins: John-Teller (JT) Type Lattice Distortions

The electronic configuration of the neutral manganese atom is as $1s^2 2s^2 2p^6 3s^2 3p^6 3d^5 4s^2$. The MnO_6 octahedron, hybridization and electrostatic interaction with oxygen *2p* electrons will create a crystal field for the outer *3d* electrons and this crystal field lifts the fivefold degeneracy of d electrons as two different lower shells; one of them is triple degenerate t_{2g} (d_{xy}, d_{xz}, d_{yz}) shells with lower energy and other has higher energy eg ($d_{x^2-y^2}$, $d_{3z^2-r^2}$) with dual degeneracy as seen in the figure (41). We mentioned earlier that it is available that two different ion states of Mn in mixed-valence manganites. When the Mn^{+4} state is considered, it contains 3 electrons in the d orbitals, these three electrons are placed t_{2g} orbitals one by one to make the spins parallel to each other due to the Electrostatic Repulsion and Hund Rule. (Cullity, 2009). The Mn^{+3} states are somewhat more complex. In the $LaMnO_3$ compound, the Mn atom is in Mn^{+3} state and the *3d* shells in Mn ions have fivefold degenerate and these levels are filled according to the Hund rule (42).

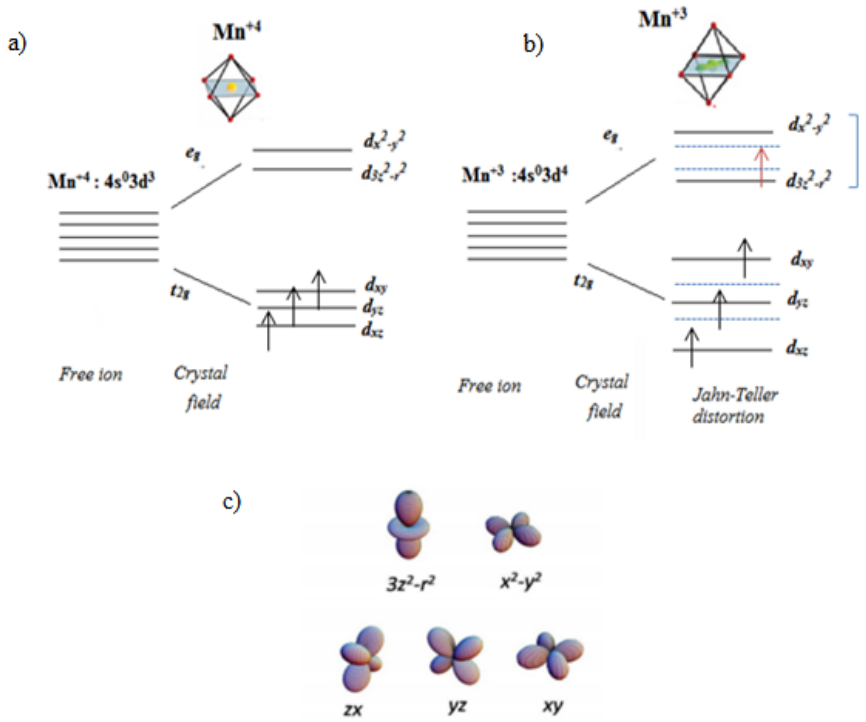

Figure 3. 5. Mn level split into t_{2g} (d_{xy}, d_{yz} *and* d_{xz}) and eg ($d_{x^2-y^2}$, $d_{3z^2-r^2}$) sublevels. a) The electron-spin configuration for Mn^{+4} b) The electron-spin configuration for Mn^{+3} and distortion because of Jahn-Teller effect c) The shapes of these *3d* orbitals.

However, there are 4 electrons at d orbital in the Mn^{+3} ion, and this excess fourth electron cannot settle at the t_{2g} level due to the Pauli Exclusion and Coulomb Repulsion Effect. This electron is placed at the level e_g by giving energy as much as Δc_F (The energy difference due to crystal field splitting (CFS) between t_g and e_g). The electron reaching the upper level is set to one of the levels of $d_{x^2-y^2}$ or $d_{3z^2-r^2}$. There is a degeneracy between these two levels and the system reduces its symmetry to destroy the degeneration. This symmetry change is called Jahn-Teller distortion (Figure 3.5). Thus, the degeneracy of the Mn^{+3} state is removed by splitting energy levels in the e_g band. "Any non-linear molecule having a degenerate fundamental electronic level will undergo a geometric distortion which will lift this degeneration, which will have the effect of decreasing the total energy of the molecule " (H. A. Jahn and E. Teller,1937) (41). The disruption of this symmetry can occur in two ways. First, as the oxygen in the z-direction in the octahedral structure moves away from each other, while the oxygen in the x-y direction

approaches each other; and the second one is that when the oxygen in the z-direction approaches each other, the oxygen in the x-y direction moves away from each other. Because of the Jahn-Teller distortion, the Mn-O bond decreases gradually at the c and a-b planes (Figure 2.5). This effect causes the Mn-O-Mn bond angle to change and as a result, the physical properties of the compound also change considerably. (Charpman, 2005). It remains to be noted that the electrons of the manganese ion, in the solid, are subjected to a crystal field potential and the atomic orbitals are strongly hybridized with the 2p levels of the ligand oxygen. It is therefore rather suitable to speak of the bands e_g and t_{2g} separated by an energy gap (≈ 1.5 eV) (42). The t_{2g} band is the valence band, and the band e_g is that of conduction; although they are not metallic.

For octahedral complexes, it occurs that when weak Jahn-Teller effect if t_{2g} is unevenly occupied and strong Jahn-Teller effect if e_g is unevenly occupied.

3.4 The Phase Diagram of $La_{1-x}Ca_xMnO_3$

In mixed valent manganites, the relationships between spin, charge, orbital degrees of freedom, and subtle displacements in the crystal lattice are the cause of many complex and interesting features. Although the phase diagram of each composition is different due to the different sizes of the different atoms involved, they have some things common properties. The Ca-doped $LaMnO_3$, i.e., $La_{1-x}Ca_xMnO_3$ (LCMO), is the prototype of the mixed-valance medium-bandwidth Perovskite-Manganite since the ion size of Ca (~ 1.16 Å) is almost identical to the ion size of La (~ 1.18 Å) and thus a real solid solution is formed in the entire range of the Ca concentration. Also, in contrast to other perovskite manganites, the structure remains orthorhombic in the total doping concentration below ~ 700 K. La1-xCaxMnO3 (LCMO) is, therefore, a good candidate material for basic understanding, and therefore its phase diagram has been described in detail (43–47).

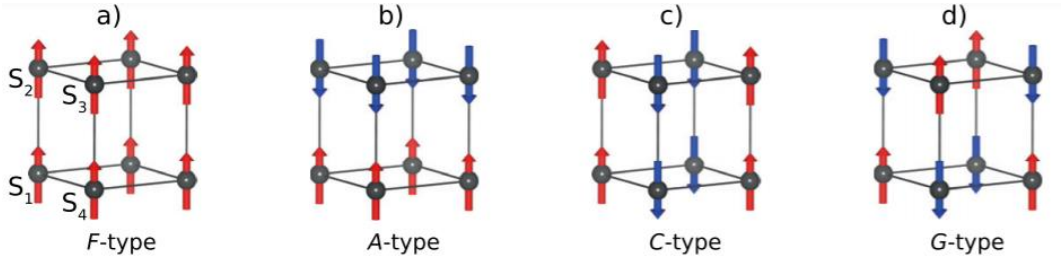

Figure 3. 6. Four types F, A, C, G of spin arrangement in the manganites, respectively. (spins-S are directed along the z-axis.) (48)

The mixed valent system of $La^{+3}_{1-x}Ca^{+2}_{x}Mn^{+3}_{x-1}Mn^{+4}_{x}O^{-2}_{3}$ produces a very rich variety of structural, electronic and magnetic phases with a dependence on temperatures changes and together of doping rate (x). As we said before in the perovskite structure; the transition metal Mn cations take in charge transfer and magnetic interactions whereas the A cations (La^{3+}, Ca^{2+}) and O^{2-} have the noble gas configuration, remain electronically inactive, they show magnetic moment; do not participate directly in the system's magnetism or electrical conduction.

3.4.1 Insulating A-Type Antiferromagnet

For x = 0, $La^{3+}Mn^{3+}O^{2-}_{3}$, all manganese ions are in Mn^{3+}, and the structure is distorted by cooperative Jahn-Teller effects. Thus, its magnetic structure depends only on how the spins of Mn^{3+} are ordered because of the only magnetic atom in this compound (49). So, we need to consider the spin alignments on the manganese ions. A strong correlation between orbital order and spin order is required because of the rules of Goodenough (50) and Kanamori (51). Precisely the rule applied is pronounced as follows: the two orbitals $d_{x^2-y^2}$, $d_{3z^2-r^2}$ oriented at 90° create a ferromagnetic coupling orbital in the (x,y) plane, while they are directed away from each other in the z-direction, and two parallel orbitals create antiferromagnetic coupling orbitals order in the z-direction, yielding a ferromagnetic coupling in this plane (50,52) as shown in Fig. 3.6. This results in a layered antiferromagnetic state denoted as A-type. The electrons are localized on the Mn^{3+} sites, and the phase is insulating. The antiferromagnetic structure appears only below the temperature of Neel T_N. Above this temperature, the compound is paramagnetic.

3.4.2 Canted Antiferromagnet Insulator

When some Mn^{4+} replace Mn^{3+} ions in a small fraction ($0 < x < 0.1$), the orbital ordering is not seriously perturbed, and the state remains insulating. However, the spin angle between the ferromagnetic planes (of A-type phase) decreases. As a result, a canting of the spins appears, and a gradual recovery of the average spin takes place (Fig 3.7). Thus a canted antiferromagnetic phase (CAF) appears (53).

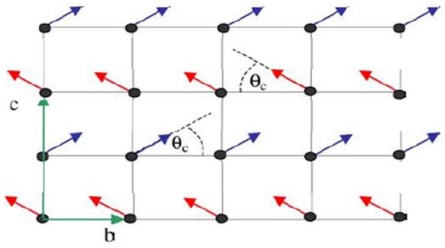

Figure 3. 7. Projection of the type A antiferromagnetic structure canted along the c-axis, in the plane (b, c). θ_c is the average cant angle. The spins in red and blue correspond respectively to the two antiferromagnetic sub-networks.

Ferromagnetic insulator: When x increases from 0.1, $0 < x < 0.5$, as Mn^{4+} ions increase (less than 50%), leads to some empty eg orbitals which allow the electrons to have some degree of mobility. In this situation, charge carriers are "holes" because of empty e_g orbital and therefore manganites are called "hole-doped" compounds. The hole-doped compounds show ferromagnetic metallic (FM) behaviour below a certain critical temperature and after a certain minimum threshold amount (x) of hole density.

The gradual increase in the doping rate continues to straighten the spins in direction c until a ferromagnetic phase is obtained. This development of orientation begins along the b axis for x = 0.11 and ends along the c axis for x = 0.185, as has been found by Xiong and colleagues for compounds doped with strontium (54). It should be noted that this ferromagnetic phase is insulating. To elucidate the insulation condition, it is important to consider the lattice distortions present up to some finite doping. Although these distortions are ferromagnetic in nature, they direct electrons to an insulating phase (55).

3.4.3 Ferromagnetic Metal (FM)

A metal-insulator transition occurs at x = 0.22. Thus, a ferromagnetic-metallic phase appears and continues until x=0.5. The compound in question is entirely ferromagnetic, below the Curie temperature, at x = 0.35 or at x = 0.3 (56). For the FM phase, e_g electrons per unit cell, which are free to move through the crystal, subject to a strong Hunds coupling to the localized spins. The kinetic energy is minimized by making all the spins parallel.

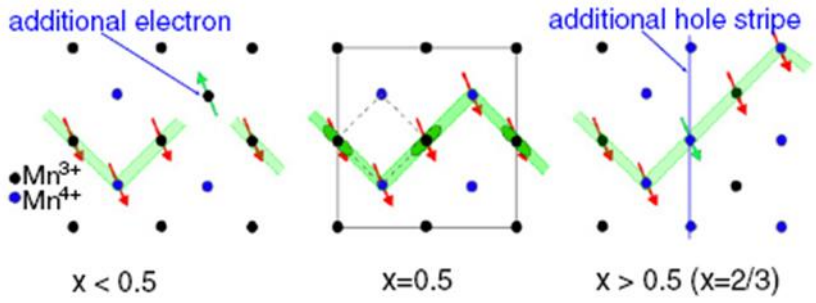

Figure 3. 8. Schematic representation of the charge- and orbital-ordered states of underdoped (x < 0.5), half-doped (x = 0.5) and overdoped (x > 0.5) crystals, showing the magnetic arrangement within the zig-zag chains of the CE-type magnetic structure.

The orbital order involves staggered $3x^2$- r^2/$3y^2$-r^2 orbitals of the e*g*-like electrons of Mn^{3+}, represented as green (dark grey) lobes in the figure. The spins, represented with red (dark grey) arrows, order ferromagnetically along zig-zag chains, a fragment of which is highlighted in light green (light grey) in the figure. The squares in the x = 0.5 panel represent the magnetic (continuous line) and *I4/mmm* (dashed line) unit cells, respectively (57).

3.4.4 The Charge-Ordered (CO) Phase

At x=0.5, for the name is used the half-doped systems when there are equal amounts of Mn^{3+} and Mn^{4+} ions, the antiferromagnetic charge-ordered insulating phase (AFI) coexists with the ferromagnetic phase. A Half-doped system is also a 'checker-board-type' order that represents the simplest case where there is an equal number of sites that differ in charge by one unit. The magnetic structure forms as FM zig-zag chains. Between the planes, spins are combined antiferromagnetically

(58). Electrons can jump along the zigzag chains, as spins are ferromagnetically linked. Although electrons can be delocalized in zigzag chains, the overall system is insulating. Figure Generally for doping concentration close to x ~ 0.50 the CE-type magnetic (Charge-Exchange) structure is stable with the formation of the charge-ordered state which is charge and orbitals are stacked in the z-direction (59). Figure 3.8.

3.4.5 Metallic A-Type Antiferromagnet

Mn^{+3} ions, as the number of electrons decreases the compound turns into antiferromagnetic in the range $0.5<x<0.625$. In this case, the c-axis (along z) is pressed and forms smaller than a and b (*x, y*), and the $dx^2 - y^2$ orbital sequence is appropriate. It is still possible to skip electrons in each (x, y) plane, but it is not perpendicular to the plane due to the shape of the $dx^2 - y^2$ orbitals that do not overlap in the z-direction. Therefore, the situation is metallic, but it is anisotropic and half two-dimensional (59).

3.4.6 Insulating C-Type Antiferromagnet

When x exceeds 0.625, the CE-type antiferromagnetic sequence with the row $d3z^2 - r^2$ appears. It corresponds to the extension of the orbit on the z-axis. Electrons can jump in the z-axis and is ferromagnetic in the z-direction, while in the x and y direction it is antiferromagnetic. The resulting form is insulating. Its orthorhombic structure turns into the monoclinic structure during the transition from the ferromagnetic phase to the load order phase. This arrangement is accompanied by an ionic order and an orbital order (OO) which leads to an insulating phase called charge order (CO).

3.4.7 Insulating G-Type Antiferromagnet

As increasing of Mn^{4+} in compounds, the G-type antiferromagnetic arrangement occurs as the Mn^{4+} are antiferromagnetically coupled to their Mn^{4+} neighbours. The small amounts of Mn^{3+} couple ferromagnetically to the Mn^{4+}, but the associated electrons cannot migrate freely through the lattice, and the state is insulating. The more Mn^{4+} is added, the more the magnetic structure is transformed into a canted antiferromagnetic configuration of type-G, where the manganese spins

are coupled antiferromagnetically in all directions. This structure is described for compounds with 0.9 <x <1. Between the two structures, type-C and type-G, a mixed structure probably settled in the compounds at 0.85 <x <0.9 (50). Experimentally, Wollan and Koehler concluded that the type-G structure is stable for compositions with x> 0.8. In the x = 1 limit, all Mn^{4+} are antiferromagnetically coupled to their neighbouring Mn^{4+}.

It should be noted that the compound $La_{1-x}Ca_xMnO_3$ is paramagnetic insulating above the temperature of Neel or Curie all depends on the value of x. A basic understanding of the different phases present in the manganites can be achieved by looking at the magnetic interaction (Super exchange, Double exchange).

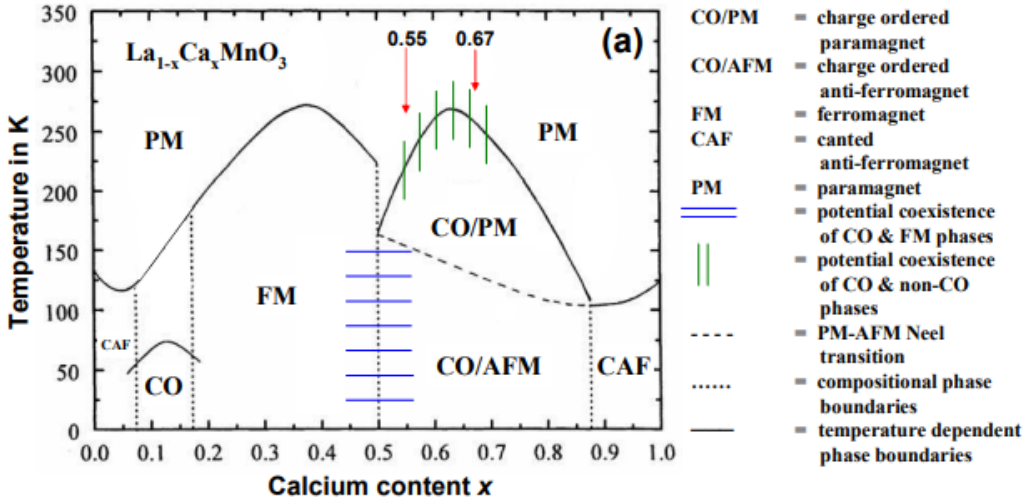

Figure 3. 9. Phase diagram of the LCMO system

3.5 Size Variance Effect at A-Site and B-Site

The disorder is found everywhere in manganites and they are not perfect crystals. Manganites are strongly correlated electron systems and therefore their properties are very affected by the change in structural stresses (60). The ionic incompatibility because of the doping of divalent, alkaline earth cations or trivalent

rare-earth cations at A-site and transition metal ion at B-site causes various interesting properties in manganites (61).

This factor was first described by L.M. Rodriguez-Martinez and J.P. Attfield (62) and are associated with the ionic mismatch in the A-Site or B site. This is quantified as,

$$\sigma^2 = \sum y_i \, r_i^2 - \langle r_{A/B} \rangle^2 \qquad (3.6)$$

Where $\langle r_{A/B} \rangle$ defined as $\langle r_{A/B} \rangle = \sum y_i \, r_i$, in which r_i is the ionic radius and y_i is the fractional occupancy of the i^{th} atoms of A site or B site. The size variance effect, σ^2, is the quantified state of the random disorder of cations (RE^{+3}, AE^{+2}) with different sizes distributed over the A-site of manganites. The variation of at A-site cation in ABO_3 perovskites causes a variation in the distance and the angle of B-O-B by originating a disorder of positions on the oxygen (63). And these orientation effects constitute the distortion of BO_6 octahedra by narrowing the eg electron bandwidth affecting electronic transport properties. There is a simple model in Figure 3.10 to show oxygen displacement (Q).

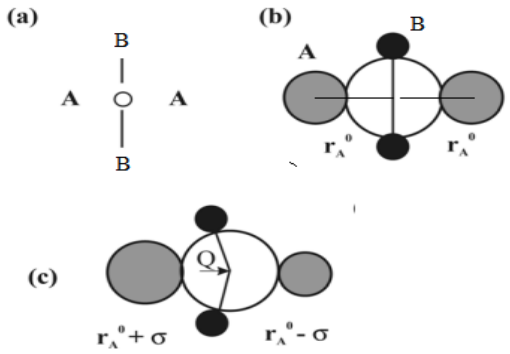

Figure 3. 10. Model for local oxygen displacements in ABO3 perovskites (64).

As seen in figure 3.10; any cation size disorder by a substitution bigger/smaller cation (b) gives, (c)rise to random oxygen displacements as an increase or decrease of Q on ideal value r_A^0; $r_A^0 + \sigma$ and $r_A^0 - \sigma$, respectively. It should be noted that this type of disorder, induced by the use of these three methods, is called "intrinsic disorder" (64).

The substitution on B-site is not easy for especially control of the hole concentration i.e Mn^{3+}–Mn^{4+} ratio and hence, there occurs an exchange interaction between mixed Mn ions. This mismatch on the B site directly changes the valance of the Mn ions. It so produces a strong scattering potential in the conduction network, by disturbing the local magnetic state and so directly affects the magnetic behaviour. It causes of weakens the ferromagnetic interactions due to the decrease of manganese ions and a reduction in double exchange interaction. And also any minor change Mn–O bond length and Mn–O–Mn bond angle cause like A-site variance effect (64). Unlike, the A site case this cannot be quantified purely by a size variance. The mismatch of ionic radius between B-site also affects the lattice parameters.

In general, in manganites, the disorder is expected, the suppression of the mobility of electrons, and consequently the decrease in T_C and/or an increase in residual resistivity, or even the suppression of magnetoresistance (65,66). As an example, Zhou et al. studied the effect of disorder in the $Nd_{0.7}$ (Ca, Sr, Ba) $_{0.3}MnO_3$ system, while setting $\langle r_A \rangle$ = 1.21Å. they found that the residual resistivity increases dramatically and the transition temperature, as well as the Curie temperature, systematically decreases with the increase in the cation disorder of site A.

4. EXCHANGE INTERACTIONS

The magnetic moments of the ions interact with each other due to their quantum nature. These are called exchange interactions.

Manganites, as transition metal oxides, play an important role in the determination of their magnetic properties, as they show the properties of these exchange interactions. The determination of the type of interactions is influenced by various factors related to the richness of the orbital structure.

Magnetic material is the result of two competing effects: thermal energy, which tends to disrupt the magnetic moments of atoms, and an order effect that depends on the type of magnetism. As the temperature decreases, thermal stimulation decreases and a cooperative magnetic order is established automatically. These exchange interactions can be direct, super or double-exchange.

4.1 Direct Exchange Interaction -Simple Exchange Interaction

The direct exchange (or simple exchange) interaction is a direct coupling via the chemical band between two magnetic atoms, close enough to have an overlap of their wave functions. Its origin is the electrostatic interaction of Coulomb. It results from energy conservation due to more distant charge distribution. This type of interaction is very weak to produce a long-lasting magnetic order. For this, and in the majority of cases, other interactions occur (67).

4.2 Indirect Interactions -Super Exchange Interaction (SE)

It is a relationship between orbital order (OO) and magnetic order purposed by Hendrik Kramers- (1934) and Phillip Anderson (1950). It explains why some ionic solids (which are insulators) have antiferromagnetic ground states (68). The exchange interaction is normally very short-ranged so that the longer-ranged interaction that is operating, in this case, must be in some sense “super”.

As mentioned in the previous paragraph, direct interaction is insufficient. It is a coupling between two magnetic ions, which are very distant from each other, that can take place via a non-magnetic anion intermediate element (Oxygen) with a

closed shell. Its origin comes from a mixture of cations in excited states with an anion in a ground state. The excited state is the result of a displacement of an electron from an oxygen ion to a half-full orbital of a cation. The relevant orbitals are the vacant Mn eg orbital and the occupied O-2p orbital, and so it is the O-2p electron that is 'shared' between the two ions. Superexchange can lead to either a ferromagnetic or an antiferromagnetic alignment of the spins, depending on the occupancy of the Mn orbitals, as shown in Figure. John B. Goodenough and Junjiro Kanamori in the 1950s developed semi-empirical rules which make it possible to determine the type of coupling between two Mn ions as a function of the orbital configurations of eg localized electrons (68). Today these rules are known by Goodenough-Kanamori-Anderson rules (69) and can be summarized as follows: (1) The coupling will be antiferromagnetic, If both orbitals on metal sites are either half-filled or when both are empty, (a). (2) The coupling will be ferromagnetic, (c) i) If the exchange is due to overlap between an empty orbital and the other half-filled ii) one orbital is half-filled and the other is complete fille. In the case where several types of these interactions occur simultaneously, the result is a set of varied antiferromagnetic structures.

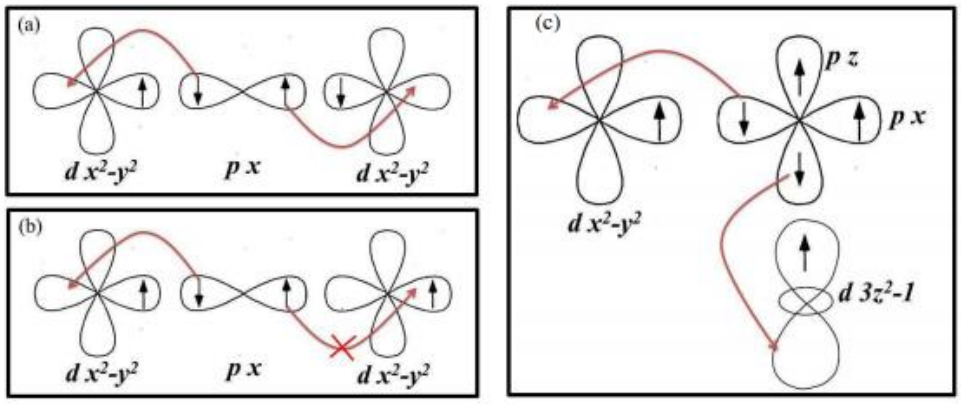

Figure 4. 1. Schematic explain of superexchange of (a) how two cations become antiferromagnetic through an anion (p_x orbital) and (b) how ferromagnetic arrangement cannot be achieved; (c) how ferromagnetic interaction can occur with 90° interaction.

4.3 Double Exchange Theory (DE)

Zener (1951) firstly offered a "Double Exchange Mechanism" (DE) that explain the correlation between magnetic (ferromagnetism) and electronic

properties in doped manganites (69). The theory was developed by Anderson and Hasegawa (1955) (55), Goodenough (1955) (50) and Gennes (1960) (70).

The doping process causes the compound to become mixed-valence electron configuration in the manganese ions and this mixed valance state gives a degeneracy of two spatially different manganite states. It is a process that contains two simultaneous motions, namely the electron moving from the Mn^{+3} to the oxygen and the electron moving from the oxygen to the Mn^{+4}. It is an indirect ferromagnetic interaction, involving oxygen as an intermediate element. It will only take place in an environment containing ions in more than one oxidation state (Mn^{3+} and Mn^{4+} for example).

If we explain it more extensively the Hund's coupling within between the incompleted *d-shell* (t_{2g}) and the conduction electrons (e_g) is strong when the spins of the charge carriers are parallel to the local ion spin. The charge carriers do not change their spins when moving from one neighbouring site to another. According to Hund's rule, it forbids a hopping process when neighbouring atoms obtain anti-parallel spins. But this exchange mechanism allows this process. DE proposed that one electron 3d $_{eg}$ orbital are converted from Mn^{+3} (t_{2g}^3 eg^1) to Mn^{+4} (t_{2g}^3 eg^0) via O-2 p orbital as depicted in figure 3-2. In this way, the e_g electrons can move throughout the lattice. This leads to a ferromagnetic arrangement of the e_g electrons. The 2p orbitals of the O^{2-} are assumed to be filled. Hence DE is considered to take place in two steps. First, the e_g electron from the O^{2-} moves to the empty Mn^{4+} orbital. Then an e_g electron from the Mn^{3+} is transferred to the vacant O^{2-} 2p orbital. This could also happen in another manner where the holes from the Mn^{4+} can move instead of the electrons from the Mn^{3+}. The result is high electrical conductivity (metallicity) and ferromagnetism as the hopping electron leads to the alignment of the spins of neighbouring Mn atoms.

The net result is one electron moving from one manganese atom to the next. So this electron transfer causes an increase in the conductivity of the passive structure, and at the same time causes the magnetic moments of the electrons to be arranged in parallel. This is called "double exchange interaction" since the junction of electron transfer and magnetic exchange interactions.

This electron jump will not occur unless the spins of the electrons of the level t_{2g} of the two ions Mn^{3+} and Mn^{4+} are aligned ferromagnetically. If these spins are aligned anti-electromagnetically, the jump is excluded according to the Pauli exclusion principle and the Hund rule which prohibits the anti-alignment of odd electrons. This is why Ziner suggested that this interaction is the mechanism responsible for ferromagnetism in manganites of perovskite structure with mixed valences like $(La_xCa_{1-x})(Mn_x^{3+}Mn_{1-x}^{4+})O_3$ (71).

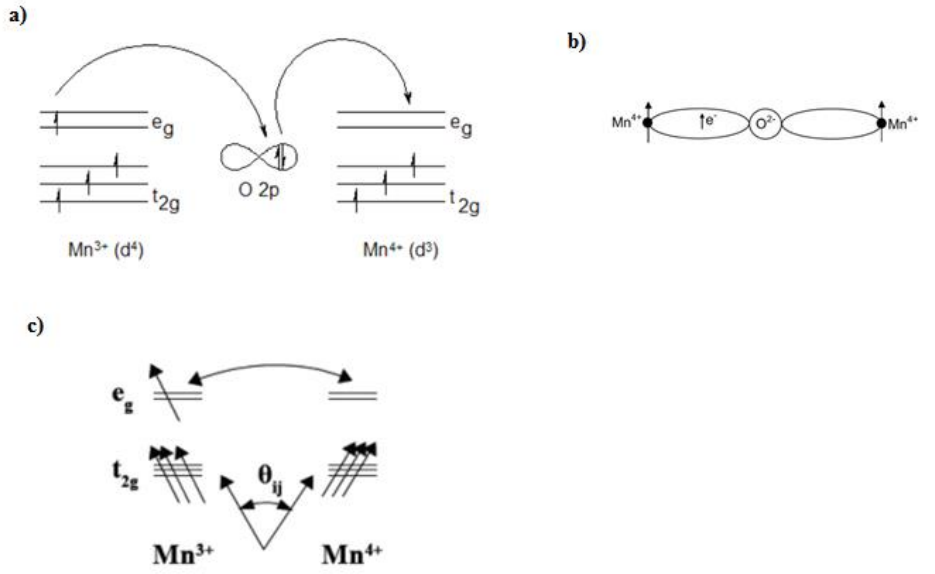

Figure 4. 2. The schematic diagram for Double-exchange interaction (a) transfer of an electron between two Mn3+ and Mn4+ ions, accompanied by ferromagnetic coupling (b) an electron is delocalized over the two Mn ions and gives rise to an effective ferromagnetic coupling. (c) The double exchange interaction between an Mn^{3+} cation and an Mn^{4+} cation, whose core spins make an angle θ_{ij} between them.

As a result of this interaction, the electron eg of Mn^{3+} jumps from a neighbouring ion of the same energy level to an empty location, thereby contributing to electrical conductivity. This jump will not occur unless the spins of the electrons of the level t_{2g} of the two ions Mn^{3+} and Mn^{4+} are aligned ferromagnetically. If these spins are aligned anti-electromagnetically, the jump is excluded according to the Pauli exclusion principle and the Hund rule which prohibits the anti-alignment of odd electrons (fig. 4.2). This is why Ziner suggested that this interaction is the mechanism responsible for ferromagnetism in manganites

of perovskite structure with mixed valences like $(La_xCa_{1-x})(Mn_x^{3+}Mn_{1-x}^{4+})O_3$ [14]. The DE model neglects to couple with phonons and the Coulomb interaction between electrons *eg* as approximations. Hasigawa and Anderson refined Ziner's proposition while establishing that the probability of the transfer of the electron t*ij (*effective hopping) from one site to another depends on cos θ/2; with θ the angle between the localised spins of the two neighbouring sites of the same compound. (Figure c) [28,30]. The effective hopping t*ij* is given by (55,72)

$$t_{ij} = t_{ij}^0 \cos\left(\frac{\theta}{2}\right) \qquad (4.1)$$

It says that effective hopping is dependent on the relative orientation of the magnetization on the two neighbouring Mn ions. If θ = 0 the probability of the jump will be maximum whereas if θ = π (180°) it will be zero. The electron delocalization will be all the easier when the spins are parallel. Below the Curie temperature, all the spins of Mn3 + and Mn4 + have the same direction for an ideal ferromagnetic compound. This is the case where the kinetic energy of the jump of the conduction electrons is maximum (θ = 0). The electron *eg* can move and a ferromagnetic state will be favoured. So, it's the ferromagnetic-conductive state that sets in. When the temperature increases towards an ideal paramagnetic regime, all the spins will be completely disordered which prevents the electrons from moving. Thus a paramagnetic-insulating state is installed. Around the Tc, the spins can be aligned easily by applying an external magnetic field, which improves the effective jump of the electrons and consequently decreases the resistivity, and the phenomenon of magnetoresistance appears (73).

DE indirect coupling is fundamentally different from super-exchange whereas both are indirect as the mechanism of interaction is different. Also for both, a non-magnetic element acts as an intermediary (oxygen in this case). However, for the first, the coupling is mediated by a non-magnetic ion via a virtual jump process, while for DE, it is the conduction of the carriers which produces the coupling. The mechanism proceeds as follows: an electron of a magnetic cation (Mn3 + for example) delocalizes from an orbital 3d to an orbital 2p of oxygen, from where an electron jumps simultaneously to an orbital 3d of the second cation. As the two processes take place at the same time, the interaction is called "double exchange".

This jump is accompanied by a preservation of the spin sign because the electron spin does not change significantly during the jump, this is why the double exchange leads to a ferromagnetic order (71,72,74). Besides, it is the jump of the electrons which is responsible for the metallic properties and lasts only about 10ps (75). Although the interaction of double exchange could explain the correlation between ferromagnetism and the metallic character of the compounds and explain qualitatively the phenomenon of magnetoresistance, it remains as even insufficient to explain the amplitude of the CMR (76).

4.4 Electron-Phonon Interaction

In the qualitative calculation of $La_{1-x}Sr_xMnO_3$ ($x \approx 0.2$ to 0.4) CMR, theoretical and experimental data did not comply because of the decrease in resistance at temperatures below T_C and that so the magnetoresistance was positive values above Tc (47). It was found that the DE interaction was inadequate and Millis et al. updated the model, considering adding the electron-phonon interaction.

This interaction originates from the distortion of the MnO6 octahedron by the Jahn-Teller effect (76,77). It represents a coupling between the e_g-electron and the distortion of MnO_6 which is caused by the presence of this same electron on e_g. In fact and as a reaction, this distortion causes the degeneration of eg. It is this action-reaction relationship that is at the origin of the electron-phonon coupling.

Since the MnO_6 octahedra are linked together, the distortion propagates in the crystal lattice, which leads to a collective deformation of these octahedra. In addition to the Jahn-Teller distortion, there is a vibration mode corresponding to a back-and-forth movement (breathing) of the oxygen atoms relative to the manganese ion (which is at the centre of the octahedron). Thus the electron-phonon coupling involves the interaction of the electron eg with successively the Jahn-Teller type phonons and the Breathing type phonons (78).

The direct consequence of the electron-phonon coupling is the lowering of the kinetic energy of the charge carriers around T_C, while creating structural polarons so that each electron is covered by a Jahn-Teller type distortion. This leads to a sharp decrease in the Curie temperature and localization of the charge carriers (79).

By changing ^{16}O by ^{18}O in $La_{0.8}Ca_{0.2}MnO_3$, we vary the vibration frequency of the phonon mode (due to the change of the mass of the atoms of the network), Zhao and al found a decrease in Tc of 21K (80). Other work by Fontcuberta et al. (81) and de Zhao (82) confirm the crucial effect of the electron-phonon interaction for the interpretation of the magneto-transport properties of manganites.

It should be noted that the charging order is considered to be a manifestation of the electron-phonon coupling. This amounts to accompanying a cooperative distortion (of the Jahn-Teller type) of the associated network of orbital order, with the transition to the charging order .

4.5 Disorder and Restriction (strain)

The disorder is found everywhere in manganites. They are not perfect crystals. The mixed-valence property allows them to be very suitable compounds for a study of the effect of disorder. Also, manganites are highly correlated electron systems and therefore their properties are highly affected by the change in structural constraints (83).

To fully understand the mechanism of disorder, it is necessary to pay attention to the introduced method. There are three main ways to control this: by changing the doping ratio to modify the ionic valences of the A site to control the electronic density.

Using different growth modes including oxygen annealing for different substrates. This can induce different structural symmetries and/or strain in the structure (84).

By varying the size of the cations on site A, with a fixed doping rate (x constant), which causes a variation in the distance and the angle of Mn-O-Mn. In this case, the disorder can be quantified using the variance σ^2 as follows (84,85).

$$\sigma^2 = \sum y_i \, r_i^2 - \langle r_A \rangle^2 \qquad (4.2)$$

Each i atom has a radius r_i and an occupancy rate y_i; $\langle r_A \rangle$ is the average ionic radius of these “i” atoms.

This variance leads to differences in the A-O bonds, which creates a disorder of positions on the oxygen. It should be noted that this type of disorder, induced by the use of these three methods, is called "intrinsic disorder".

In general, in manganites, it is expected of disorder, suppression of electron mobility, and consequently reduction of T_C and/or increase of residual resistivity, or suppression of magnetoresistance (65). For example, Zhou et al.(86) studied the effect of disorder in the $Nd_{0.7}(Ca, Sr, Ba)_{0.3}MnO_3$ system, while fixing $\langle r_A \rangle$ = 1.21Å. They found that the residual resistivity increases dramatically and the transition temperature, as well as the Curie temperature, decreases systematically with the increase of the site A cation disorder.

4.6 Complex Ordering Phenomena

One of the essential points in the structural characterization of manganites lies in the understanding of the phenomenon of ordering charges, charge ordering (CO). The order of the charges is observed when the electrons are localized due to the strong correlation effect. These phenomena include charge order, orbit order, and spin order, and often accompany magnetic, structural and metal-insulator phase transitions, etc.

4.7 Charge Ordering and Orbital Ordering

Charge ordering (CO) is an order of charges is observed experimentally, when the temperature is lowered, by a sudden increase in the resistivity at the charge order temperature (T_{CO}) In Figure 1.7. It was discovered for the first time by observation of superstructural peaks that have no relation to magnetism for $La_{0.5}Sr_{0.5}MnO_3$, in neutron diffraction data (56).

The charge-ordered phases in manganites result from interactions between the charge carriers and phonons where the Jahn–Teller distortions play a significant role.

Charge order frequently occurs in mixed-valence perovskites because it needs electron/hole asymmetry. This interaction promotes the charge localization at specific sites below a certain temperature, T_{CO}, that causes a rise to order off the

$Mn^{3+/}Mn^{4+}$ ions throughout the crystal structure, at the same time to rise of orbital ordering (OO). This makes the substance insulating.

In Figure 4.4 two examples of compounds having a charge order transition are shown. The compound $Nd_{0.5}Sr_{0.5}MnO_3$ first has a ferromagnetic state and then goes into the charge order domain, whereas the compound $Sm_{0.5}Ca_{0.5}MnO_3$ goes directly from the paramagnetic phase to the phase order of charges. Various studies have shown that the order of charges was sensitive to the application of a magnetic field. The effect of the magnetic field is to align the t_{2g} spins of the manganese ions thus favouring the delocalization of the electrons by double exchange, and thus modifying the order of the charges (87).

We showed before CO model for the half-doping level leading to the lattice period doubling of the crystal. The CO has a simple AFM type even though the magnetic correlation lengths of each sub-lattice are different. Along the c-axis FM spin chains are observed (88).

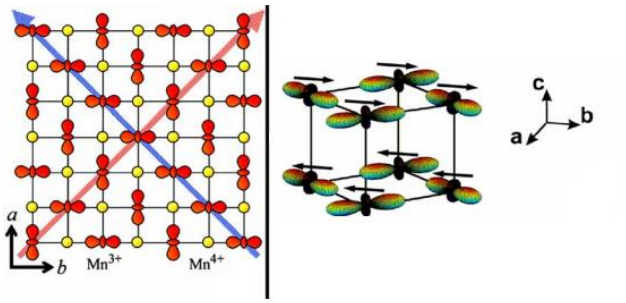

Figure 4. 3. Left- $Pr_{0.5}Ca_{0.5}MnO_3$: orbital order $3d_{3x^2-r^2}$ / $3d_{3y^2-r^2}$and charge order of the CE type projected on the MnO_2 sheet (a-b plane). Right- LaMnO3: orbital order $3d_{3x^2-r^2}$ / $3d_{3y^2-r}$ and A-type AFM spin order.

Orbital ordering (OO) (polaron ordering) is the arrangement of the long axis of octahedra with Mn^{3+} ions (or arrangement of doped holes surrounded by local JT distortions) in the ab-plane (88). It favours when the *d* electron occupies an asymmetric orbital ordering. The direct electrostatic repulsion of the charged clouds, coupled with cooperative JT distortions, stabilizes the effect generating an ordered sublattice of orbitals. The OO phenomenon is often indirectly linked to the JT effect, which consists of distortions of the orbital order and vice versa (15).

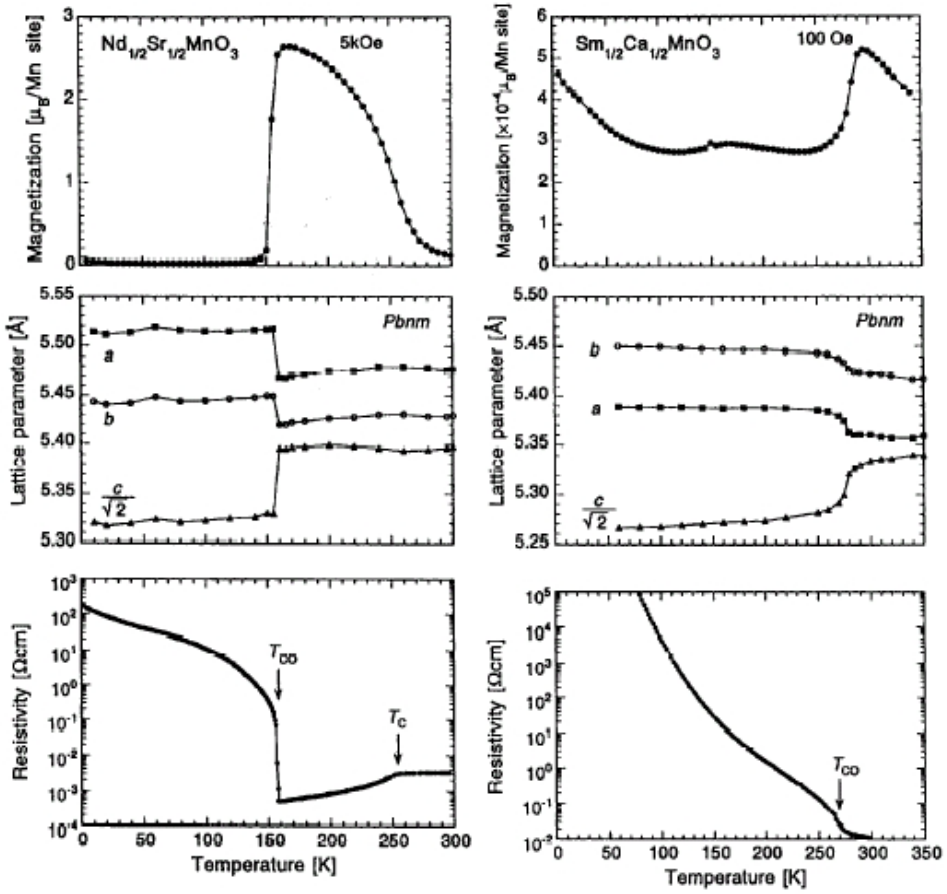

Figure 4. 4. Measurement of magnetization and electrical resistivity and evolution of cell parameters, as a function of temperature, for the compound $Nd_{0.5}Sr_{0.5}MnO_3$ (left) and $Sm_{0.5}Ca_{0.5}MnO_3$ (right).

4.8 Phase Diagram of Layered Manganites

Simple cubic perovskite $La_{1-x}(Ca,Sr)_xMnO_3$ with 3-D structural Mn-O networks, as we mentioned before show ferromagnetic conducting properties at doping concentrations of x>0.2. Many experimental studies showed that MnO_6 octahedra take on an important task in the spin-charge dynamics, which is responsible for the magnetic and electrical properties of the compounds. The studies examining structural factors and magnetic phase diagrams have indicated that the

more deterioration in Mn-O-Mn bond angles or bond lengths, that is, the more the MnO6 octahedra distortion, the greater the insulating behaviour, the reduction of magnetic Tc and improved magnetoresistance effects occur.

Experimental analyses on layered RP phase having the general formula $(AA')_{n+1}B_nO_{3n+1}$ also showed structures with two or quasi-two-dimensional Mn-O networks with n=1 (K_2BO_4 type) $La_{1-x}Sr_{1+x}MnO_4$ have shown a two-dimensional antiferromagnet feature (25,26).

Studies on $La_{2-2x}Sr_{1+2x}Mn_2O_7$ (x=0.4) single crystals,[27] $La_{2-2x}Ca_{1+2x}Mn_2O_7$ (x=0.25)[28] polycrystalline bulk and (x=0.3) [29] thin films also have showed two-dimensional ferromagnetic phases. H. Asano and et all (1997) also found $La_{2-2x}Ca_{1+2x}Mn_2O_7$ thins films becomes a metallic ferromagnet for doping concentration $0.22<x<0.5$.

When considering spin-charge coupling for layered perovskites, we should consider the DE model by taking account of their anisotropic nature. As we know to describe electron hopping between Mn sites, we use the equation of $t_{ij} = t_{ij}^0 \cos\left(\frac{\theta}{2}\right)$, the t_{ij}^0 matrix element manages the hopping between mobile electrons and local electrons, so ferromagnetic transition temperature and electronic conductivity. In the layered perovskite, the motion of doped holes and hence the exchange interaction would be anisotropic in the a-b axis (in-plane) and c-axis (out-of-plane) directions. The in-plane (in a-b axis) exchange interaction is stronger than the out-of-plane (c-axis) exchange interaction and so that the probability of electron hopping (hole transfer) in the in-plane direction is much higher. We can summary this phenomenon as for the anisotropic exchange energy $J_{ab}>J_c\gg J'$ (J_{ab}, Jc, J', represent for the in-plane, inter-single-layer, and inter-bilayer exchange interaction, respectively) in the quasi-two-dimensional ferromagnetic system (21, 22).

We can assume for the electron hopping the other parameters also affect the in-plane and out of plane directions. It can be said that the lower critical temperature (T_{c1}) results from the out-of-plane exchange interaction, and the higher critical temperature (T_{c2}) results from the in-plane exchange interaction.

H. Asano, J. Hayakawa, and M. Matsui analyzed the double-octahedral perovskite $La_{2-2x}Ca_{1+2x}Mn_2O_7$ compound (89) (Figure 4.5). In the range of $0< x<0.2$ a canted ferromagnetic insulator; for $x\geq 0.22$ ferromagnetic metal is observed for low temperatures. Between the value of $0.22<x<0.5$; two different transitions are detected as from a paramagnetic insulator (PI) to a ferromagnetic insulator (FI) and finally to a ferromagnetic metal (FM). They are divided into four different parts according to the a) $T\ll T_{c1}$, b) $T\leq T_{c1}$, c) $T_1<T_c<T_{c2}$ d) $T>Tc_2$. At $T\ll T_{c1}$ there is increased spin fluctuation in the c-axis between neighbouring double MnO_2 layers, whereas spin ordering in the a-b axis direction is still preserved. Finally, at $T>T_{c2}$, spin ordering completely disappears.

The main difference between the single-layer and layered perovskites is that existing of the ferromagnetic insulating state over the wide range ($0<x<0.5$) in the $La_{2-2x}Ca_{1+2x}Mn_2O_7$ system for low hole concentration. The $T_1<T_c<T_{c2}$, range, where two-dimensional ferromagnetic alignment is observed, is also a prominent feature in double-layer perovskite manganite disappears. This is a distinctive feature because is it polycrystals or single crystals. Because of the 2-D ferromagnetic arrangement and the anisotropic carrier motion with an intrinsical insulator like transport is in the c-axis direction and metallic transport is in the ab-axis direction.

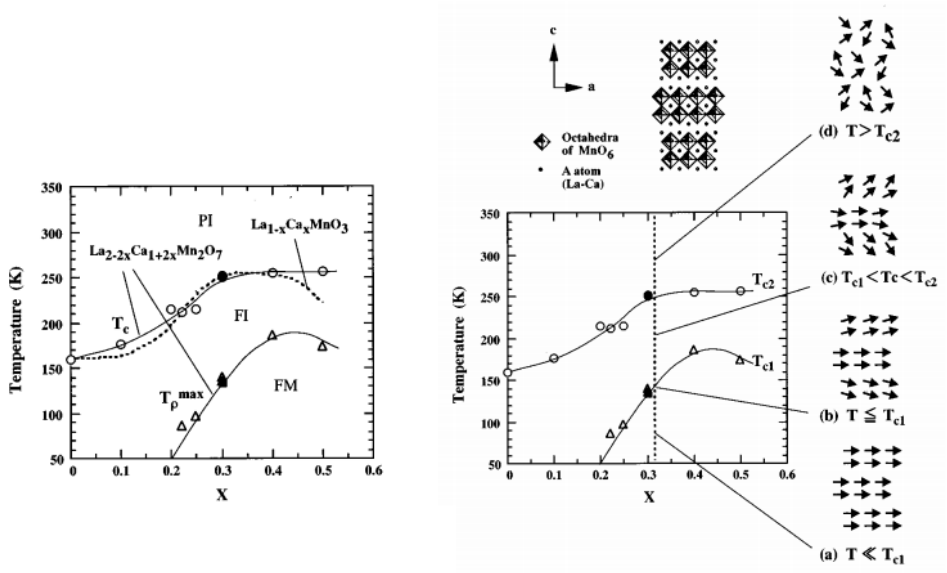

Figure 4. 5. (left)Magnetic phase diagram of bulk La_{2-2x} Ca_{1+2x} Mn_2O_7. The triangles denote the peak temperature in resistivity $T_{p\text{-}max}$. The circles denote the magnetic transition temperature T_c. (right) Proposed model of temperature-dependent spin alignment for the double-perovskite ferromagnet La_{2-2x} Ca_{1+2x} Mn_2O_7, (T_{c1} and T_{c2} are determined from the M-T curve in a magnetic field of 1 mT) and the higher ordering temperatures (taken from ref (15)).

T. Kimura And Y. Tokura showed a wide variety of magnetic structures even within the limited carrier concentration region for $La_{2-2x}Sr_{1+2x}Mn_2O_7$ ($0.3 \leq x \leq 0.5$)(Figure 4.5) (90). They described the direction magnetic moment of the MnO_2 interlayer and the magnetic orientation of a bilayer unit. The connection between the respective MnO_2 layers and bilayer unit and between two adjacent MnO2 layers depends on the doping level. As seen in the figure, for low values of $x \sim 0.3$, the magnetic moments of interlayer single MnO_2 couple ferromagnetically within a bilayer and align along the c-axis. For $x \geq 0.33$ the magnetic moments direct along the ab-plane and the constituent single MnO_2 layers become into the canted AF one beyond $x \sim 0.4$. The canting angle θ gradually increases with the increase of x and finally, for x= 0.5, the A-type AF order occurs ($\theta = 0$) (13, 17).

5. MAGNETO-TRANSPORT CHARACTERIZATIONS

5.1 Metal-Insulator Transition

Mixed valance manganites $Ln_{1-x}A_xMnO_3$ (A: divalent ion) as an electrical transition from insulator to metal transition (T_{MI}) accompanied by magnetic transition from paramagnetic to ferromagnetic transition (T_C). Most of the manganites are in paramagnetic - semiconducting or insulating (P_{MI}) state at room temperature. When the temperature is reduced below T_C, electrical resistivity increases and insulator-metal (I-M) transition occurs in the near of paramagnetic to ferromagnetic transition. In the case of half doped manganites, at low temperature, below T_{MI} one can observe an increase in the resistivity along with a decrease in magnetization at temperature T_N known as Neel's temperature.

Some models were established to qualitatively explain the metal-insulator transition observed at that time in several oxides. The dual exchange model is the one that explains the complex relationships in the mixed manganites with many oxides that include many factors (91). (Coulomb interactions, the Hund Coupling, Pauli exclusion Principle, structural distortions, the crystal field, the Jahn-Teller effect magnetic exchange couplings, etc.)

The double exchange (DE) model takes this reality into account. It has been reported that the magnetotransport properties of manganites, the metal-insulator transition, are governed by the Zener double exchange interaction (71), while basing on the mixed-valence state Mn^{3+}/ Mn^{4+} In the optics of the DE model, at $T > T_C$ the system is in paramagnetic state PM and the resistivity follows a behaviour of an insulator ($d\rho/dT<0$). This behaviour is due to a disorder of the directions of the spins. At $T < T_C$, the interaction of DE between Mn^{3+}/ Mn^{4+} involves the FM

coupling which promotes the transfer of charge carriers between the adjacent Mn ions, which leads to a metallic transition. This means that the MI transition (and therefore the MR) is magnetic in nature (92).

Some studies have shown that T_{MI} is controlled by the size of the ion at site A since it affects the Mn-O-Mn bond. J. Fontcuberta et al (93) concluded that the size of the lanthanide in the compound $L_{1-x}Ca_xMnO_3$ controls the T_{MI} temperature, via the modification of the Mn-O-Mn bond. They found that the T_{MI} decreases when the tolerance factor decreases, as a result of the variation in the size of the La-ion.

5.2 Magnetoresistance (MR)

Magnetoresistance is defined as the variation of the resistivity of material under the influence of a magnetic field. Two ways can affect this feature:

• Directly by acting on the conduction electrons.

• Indirectly by affecting the magnetization (thus the resistivity depends on the magnetic state of the system).

This property was discovered by William Thomson (Lord Kelvin) in 1857 (94). It is called thereafter ordinary magnetoresistance (OMR). However, at that time, it was impossible to vary the resistance by more than 5%. More recently, research on materials has led to the discovery of different types of magnetoresistance: giant magnetoresistance, colossal magnetoresistance and tunnelling magnetoresistance. More details are given in the next sections.

Magnetoresistance (MR) can be given by the expression:

$$MR(H) = \frac{\rho(H)-\rho(0)}{\rho(0)} \quad (5.1)$$

With ρ (0) the resistivity without application of a magnetic field; ρ(H) the resistivity under a magnetic field.

In some cases, it has been noticed that the shape of the MR-(T) curve is very similar to that of the resistivity ρ(T) at H = 0. The authors deduced that this suggests that MR and MI transition have the same basis as the physical origin.

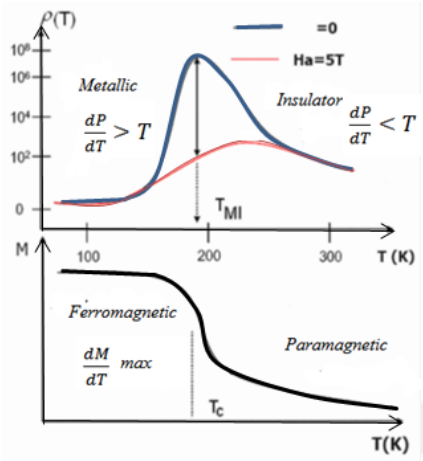

Figure 5. 1. Resistance and phase change of $La_{1-x}Ca_xMnO_3$ single crystal under magnetic field with temperature.

Despite the very high number of scientific studies devoted to the study of the magneto-transport properties of manganites, the scientific community remains unable to establish a general theory. This is because manganites (which are highly correlated materials exhibit strong structure-charge-spin-orbital coupling (95). Also the number of interactions and mechanisms involved, round the explanation, the various phenomena observed, very complicated.

However, the results already obtained allow us to conclude that four essential parameters are affecting the magneto-transport of manganites and therefore are essential for the understanding of magnetoresistance. These are; the Mn^{+3}/ Mn^{+4} rate; the average radius $\langle r_A \rangle$ of the cations at site A; the disorder associated with the difference in the size of the cations at site A; the intergranular effects in the case of granular manganites. These parameters involve the one-electron orbital e_g, so this orbital is considered as the critical parameter governing MR and related properties (96). The different interactions that govern magneto-transport; namely the double exchange interaction, the super-exchange interaction,

the electron-phonon, electron-magnon interactions, etc. are essentially affected by these three parameters (97).

Figure 4.5 of the phase diagram (FM-M, AFM-I, PM-I, OC, etc.) of the manganites is directly related to x. This relationship is related to the balance of Mn^{+3}/ Mn^{+4}. Therefore, since magnetoresistance is largely dependent on these conditions, it depends on x.

The mean radius of site A, $\langle r_A \rangle$ is directly associated with structural deformations, which influence magnetic interactions. Indeed, the double-exchange and super-exchange interactions depend on the angle Mn-O-Mn and are influenced by the size of the ionic radius (Re, A) in all the systems $(Re, A)_{(n+1)}\ Mn_n\ O_{(3n+1)}$. The interaction of ferromagnetic order decreases with the decrease of $\langle r_A \rangle$ This decrease can occur at a point where the compound loses its ferromagnetic state (98). J. Fontcuberta et al concluded that the La^{3+} lanthanide radius in the La1-xCaxMnO3 compound controls the MR and the TMI temperature since it affects the Mn-O-Mn bond. Increasing the distortion of this link decreases T_{MI} and improves MR. The improvement in MR is due to the decrease in T_{MI}, the reduction in the mobility of doping holes and an increase in the coupling between itinerant and localized electrons (93).

The occupation of the same site by elements of different sizes while keeping $\langle r_A \rangle$ constant induces a disorder σ^2 (eq 4.2). Compounds with the same $\langle r_A \rangle$ and different σ^2 have different properties. Magnetic interactions are strongly affected by the disorder, whereas $\langle r_A \rangle$ affects the structural symmetry. Also, it has been shown that the disorder acts on the Curie temperature. It decreases when the disorder increases beyond a certain threshold (98,99).

In the case of granular manganites, numerous studies show that the effect of grain boundaries plays a very important role in the transport of electrons and the MR, especially at low temperatures (81,100,101).

In the 1970s , the scientific community of the field focused on the study of the effect of grain boundary on the magneto-electric transport in such compounds. They concluded that each grain creates an electric field in its surroundings and

behaves like a capacitance micro-capacitor C and energy are stored (102,103). It is easily deduced that the stored energy becomes very important for very small grains. Thus the activation of the transport becomes more and more difficult as the reduction of the grain size decreases when the temperature decreases. This situation may evolve to a point where load transport is stuck. This explains the growth of the resistivity at very low temperatures where the electron localization effect will take place. Such a mechanism has been observed for all granular metal thin films and certain oxides(102,104). Also, at low temperatures, it is expected that the Mn-O-Mn bonds will be destroyed at the grain surface; this may reduce DE transfer and therefore lead to an insulating state in a ferromagnetic phase. It is found that the resistivity depends largely on the size of the grains.

5.3 Giant Magnetoresistance (GMR):

The phenomenon of Giant magnetoresistance (GMR) was first discovered in 1988 with Fe-Cr-Fe superlattice structure (105,106). This subject to very important technological applications and Fert and Grunberg obtained European Nobel Prize in 2007 as controlling of magnetisation. They focused on the magnetoresistance study of monocrystalline layers. As the nature of the meaning of “giant," GMR means a significant and sudden decrease in the resistivity under the magnetic field system. It is a quantum effect observed in the structures composed of alternating ferromagnetic layers of ferromagnetic materials (such as Iron or Nickel) and non-magnetic layers commonly known as multilayers (107,108). (Ferromagnetic /nonmagnetic-conducting / Ferromagnetic). It is manifest as a difference in electrical resistance between a configuration where the magnetizations of the ferromagnetic layers are parallel, and a configuration where the magnetizations are antiparallel. Giant magneto-resistance is given by the following relationship:

$$GMR = \frac{R_{\uparrow\downarrow} - R_{\uparrow\uparrow}}{R_{\uparrow\uparrow}} \qquad (5.2)$$

; where $R_{\uparrow\downarrow}$ and $R_{\uparrow\uparrow}$ are the resistivity for the antiparallel and parallel configuration, respectively.

It is based on the fact that the electron spins do not move at the same speed depending on the orientation of the magnetization of the material as well as the fact that the conductivity of a material is directly related to the speed of the electrons passing through it.

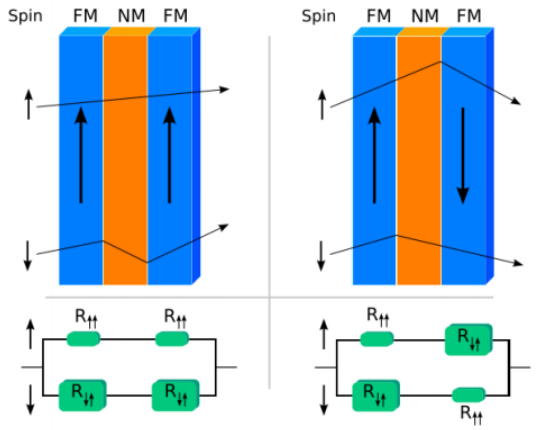

Figure 5. 2. Principle of the giant magnetoresistance: by reversing the magnetization of a layer employing an external magnetic field, one affects the circulation of the electrons of spin "up" and "down" and thus the resistance of the multilayer component (107).

The GMR phenomenon has had an enormous technological impact on the computer hard drive industry. Especially GMR sensors come from the physical domain of spin electronics. Typically, a GMR sensor is composed of several layers; two ferromagnetic layers separated by a conductive layer. The orientation of one of the two ferromagnetic layers is forced while the other layer has a variable magnetization. When an external magnetic field is applied, the magnetization aligns with this field; otherwise, it aligns itself parallel to the magnetization of the hard layer. The resistance of the GMR thus varies according to the external magnetic field (107).

GMR sensors are used to measure the magnetic field, electric current, position and velocity linear or angular. They are also widely used as a read head in hard drives. They have a wide detection bandwidth that ranges from continuous to MHz with a detection resolution of around 8A/m (109).

R. von Helmolt et al. found a magnetoresistance of 60% at 300K for a thin film of $La_{2/3}Ba_{1/3}MnO_3$ in 1993 (110). Thus, manganites regained interest in the early 1990s and researchers have extended their work to other series such as $La_{1-x}Ca_xMnO_3$. These compounds with $0.25 \leq x \leq 0.4$ also have important magnetoresistances that can reach more than three orders of magnitude.

The compounds mentioned above have a magnetoresistance around TC accompanied by a low-temperature FM-M order for x <0.5. The MR, in this case, is due to the influence of the magnetic field on the critical fluctuations of the FM-M phase. In addition to the GMR, another type of Colossal MR originates from other causes.

5.4 Colossal Magnetoresistance (CMR)

The colossal magnetoresistance is since its values can reach 1011%. It originates from causes different from that of GMR. The colossal magnetoresistance originates, for the $Pr_{1-x}Ca_xMnO_3$ type compounds, in the transition from the paramagnetic and insulating charge order phase (CO-PM-I) to the ferromagnetic and metallic phase (FM-M), by the application of the external magnetic field. It is observed at low temperature which limits its technological application. Despite the very high number of research work done, no model can explain magnetoresistance in all materials. No complete theory is established until today. Moreover, very recent work suggests that colossal magnetoresistance is managed by the same mechanism that manages the GMR (111).

5.5 Tunnelling Magnetoresistance

If we replace the nonmagnetic metal layer required for the GMR effect with a thin nonmagnetic insulating layer; we can see the tunnel magnetoresistance (TMR) in the newly formed system. The thin insulating layer (typically a few nanometers) constitutes barrier energy for the conduction electrons, these electrons can nevertheless cross the barrier by tunnel effect depending on the configuration of ferromagnetic materials: this is the principle of TMR (Figure 4.3) the tunnelling of electrons through the insulator layer can be explained based on quantum mechanics because it is prohibited in classical physics. This effect had been observed at low temperatures by Michel Jullière in 1975 for the first time (112) in

semiconductor magnetic junctions, using iron as the ferromagnetic layer and germanium as an insulator. In 1995, tunnel junctions were saw renewed interest and exploded after observing room temperature tunnelling magnetoresistance in amorphous alumina junctions. Since then, the materials constituting the tunnel barriers have made enormous progress, used in current technologies such as magnetic sensors, inductive read heads of modern hard drives, and they are also behind MRAM, a new type of non-volatile memory(113).

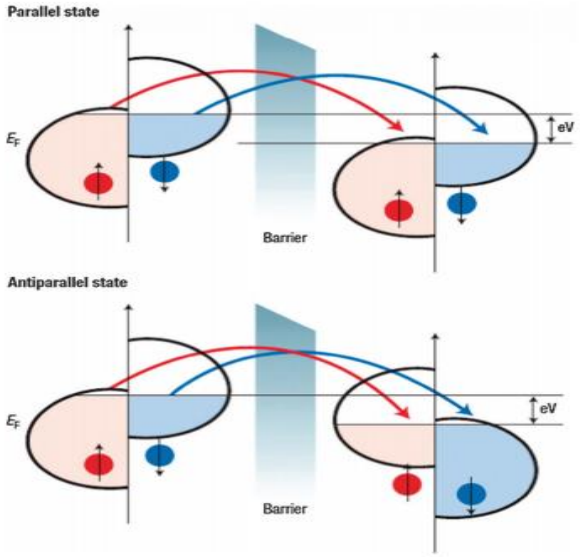

Figure 5. 3. The schematic diagram for the principle of tunnel magnetoresistance (TMR) for a tunnel junction (114).

5.6 Magnetoresistance on Layered Manganites

The La-based DL manganites have gained much importance since Moritomo et al. discovered CMR (115). These materials (RP series) show large MR values which are required for technological systems. Layered manganites have a natural array of ferromagnetic-insulator-ferromagnetic junctions that forms the framework of tunnelling structures and spin valves in a single chemical phase, as opposed to the larger-scale structures obtained by thin-film deposition. The RP series has low dimensionality (2D) compared to simple perovskites (3D) and the crystal lattice of ferromagnetic metal layers incorporating MnO_2 bilayers that are far apart by a rock salt nonmagnetic $(La, Sr)_2O_2$ insulating layer (115) (Kimura 1996) leads anisotropic characteristics in charge-transport and magnetic properties.

The crystal structure of $La_{1.2}Sr_{1.8}Mn_2O_7$ consists of double layers of corner shared ferromagnetic-metallic MnO6 octahedra (perovskite structure-type) in the ab-plane of the crystal, separated by a single rock-salt-type nonmagnetic-insulating (La, Sr)O layer along the c-axis giving it 2D character. Exploring these opportunities, Kimura et al. (115,116) have recently reported the observation of spin-polarized interlayer conductivity and high CMR in the naturally layered materials $La_{2+2x}Sr_{1+2x}Mn_2O_7$, x=0.3 ($10^4$ % at 50 kOe and 90 K)

Doping by Eu in the $La_{1.2-x}Eu_xSr_{1.8}Mn_2O_7$ system (x = 0-0.4) has been studied by J. Zhang et al. (117). For x = 0-0.2, doping gradually removes the ferromagnetic-metallic state. The metallic character disappears completely for x = 0.2 and x = 0.3. For x> 0.2, no magnetic order is observed. Practically the same results was obtained for doping with dysprosium (Dy) in the $La_{1.3-x}Dy_xSr_{1.7}Mn_2O_7$ system (x = 0.0,0.05, 0.1, and 0.2) (118). The MI transition is only observed for x = 0 and x = 0.05. With doping, the metallic character gradually disappears and the T_{MI} decreases. Besides, the resistance increases with the rate of doping. The authors attributed these results to the structural distortion due to the substitution of La by the smaller element Dy. The magnetoresistance is greater for doped compounds when compared with the undoped ones.

5.7 Magnetization, Susceptibility and Curie Temperature

All materials are consist of a series of a set of atoms that can be either magnetic or non-magnetic. In the free state, an atom is magnetic if it carries a permanent magnetic moment represented by a vector of constant modulus. In the case of the magnetic assembly, the direction and sometimes the modulus of the magnetic moments can depend on the particular environment of each atom (nature and position of neighbouring atoms, temperature and applied magnetic field). These magnetic moments can be aligned by applying a magnetic field which produces a magnetization *(M*) proportional to the induction field (*H*). The magnetization thus reflects the change in energy associated with the presence of an applied magnetic field.

$$\overrightarrow{M} = \chi \overrightarrow{H} \qquad (5.3)$$

Where χ denotes the coefficient of proportionality called magnetic susceptibility. It could be explained as the response of a system to a magnetic field (*H*). The magnetic susceptibility of ferromagnetic substances is given by the Curie-Weiss law as; $\chi = \frac{C}{T-T_C}$ where *C* is a material-specific Curie constant, *T* is the absolute temperature and T_C is the Curie temperature. Beyond the T_C the structure loses all magnetic organization and becomes paramagnetic.

Rodriguez-Martinez and Attifield (63,65) were the first studied researchers that the behaviour of magnetic susceptibility gradually deviates from the Curie-Weiss law with the increasing disorder (σ^2). In the same period, Oseroff et al. (119) showed the coexistence of a ferromagnetic signal and a paramagnetic signal above T_C by electron paramagnetic resonance spectroscopy (EPR). These authors have highlighted the presence of short-distance interactions and the formation of spin clusters above T_C. All these observations support the idea that disorder can induce nanometric inhomogeneities in manganites above T_C (120).

In a paramagnetic material, atoms have a non-zero magnetic moment and disorder in all directions because of their thermal agitation. Under the action of an external field, these magnetic moments are oriented and increase the applied H field strength in the sample. As with diamagnetism, it is a weak and temporary phenomenon. Unlike diamagnetism, the response of a paramagnetic material aims to reinforce the action of the external *H* field. Note that this phenomenon decreases with the increase in the temperature since thermal agitation disorients the elementary magnetic dipoles.

The magnetization of a ferromagnetic material corresponds to the orientation of the elementary dipoles in the same direction. Unlike the paramagnetic, this orientation can occur spontaneously, in the absence of an external *H* field. In general, the total magnetic moment is zero because the different domains have different orientations, and their effects cancel each other out. In a ferromagnetic material, three types of interactions coexist exchange interactions, interactions with the network and magnetic dipole interactions. The magnetic susceptibility of ferromagnetic substances is given by the Curie-Weiss law as; $\chi = \frac{C}{T-T_C}$ where *C* is a material-specific Curie constant, *T* is the absolute temperature

and T_C is the Curie temperature. Beyond the T_C the structure loses all magnetic organization and becomes paramagnetic. (Figure 5.4) (121).

For ferromagnetism, the magnetic susceptibility χ is very high around 10^5 amperes per meter and varies with H. As a result, the spontaneous magnetization is very high.

In antiferromagnetic substances, the moments of the atoms are strongly linked with a particular coupling characterized by antiparallel arrangement. The alternation of the direction of the moments of the sub-networks generates a resultant moment zero and there is no spontaneous magnetization in the absence of applied field. The expression of the magnetic susceptibility of the antiferromagnetic compounds is given by the law of Néel: $\chi = \frac{C}{T+T_N}$ with T_N is the transition temperature, called Néel temperature; When the temperature increases the magnetic susceptibility decreases to at the Neel T_N temperature and it is a transition temperature of which an antiferromagnetic material becomes paramagnetic.

However, the problem of magnetic susceptibility is not so simple, several models have been proposed to explain the anomaly observed in susceptibility at high temperatures.

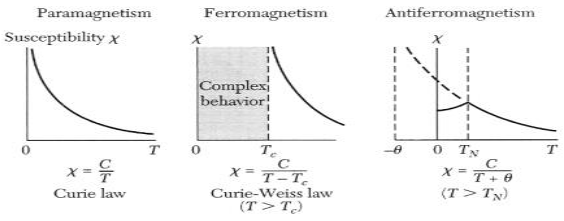

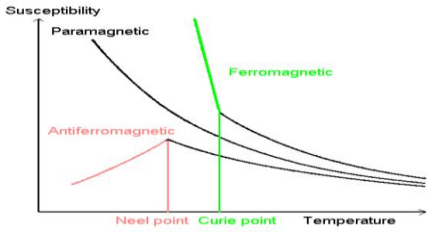

Figure 5. 4. The representation of phase transition, (upside shows partially down one is on one graph.

Determining Curie temperature is an important experimental research subject to interpret the phase transitions and mixed phenomena of the item. The two important interactions between Mn ions, double exchange FM interaction (DE); and antiferromagnetic (AFM) interactions (superexchange, SE) are responsible for the observed transport and magnetic properties of manganites. The strength of exchange interactions depends on interionic distances and bond angles (Θ) of Mn-O-Mn. As the structure changes from the cubic to rhombohedral and to orthorhombic, the bond angle becomes smaller and the magnetic interaction becomes negative. ($\Theta_p < 0$) for $\Theta < 150$). Hwang et al. (122) studied $La_{0.7-x}Pr_xCa_{0.3}MnO_3$ and $La_{0.7-x}Y_xCa_{0.3}MnO_3$ at constant electron concentration to investigate the tolerance factor and bond angle by neutron scattering. As the Mn-O- Mn angle fell from the ideal 180°, a serious decrease was observed in T_C (123,124).

The power of double change (and hence T_C) depends precisely on the orbital overlap between manganese and oxygen. Also, the magnetization of samples with reduced Mn-O-Mn angles are more difficult to saturate. This can be attributed to the rivalry between double-exchange and super-exchange interactions, which can lead to canting manganese magnetic moments. However, the bond angle is just one of the factors affecting Curie temperature. The range of Mn-O- Mn angles examined is quite limited ($156.5° < \Theta < 168.5°$), and the generalization of T_C correlation with cation substitutes is controversial. As the radius of the added alkali ion increases (the atomic weight decreases), there is a certain increase in Tc (125) concerning the bandwidth eg. (126). Similarly, there is a tendency in Tc to increase and then to saturation with increasing the A-region cations' tolerance factor or mean size of the A-site cations (30,122,127). This is probably a reflection of changing the Mn-O-Mn bond angle. However, there is no clear trend associating T_C with the atomic weight, size or electronegativity of the alkali ion.

Typically low-T_C samples show a hysteretic behaviour on magnetic and resistive transitions, for T_C <100 K (30,122). This behaviour may be related to the magnetic degrees of freedom associated with the nonlinear ferromagnetic order. The Tc is reduced by non-magnetic trivalent B-site substitutions such as aluminium, gallium, iron, or indium (30,128).

This may be due to the magnetic-domain-based mechanism coupled either with the dispersion of spin at the grain boundaries or with the tunnelling effect of polarized spin at the grain boundaries.

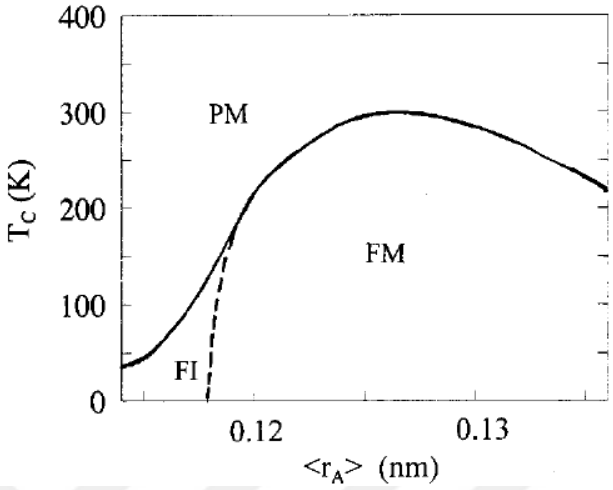

Figure 5. 5. The change in Curie temperature T_C of $R_{0.7}A_{0.3}MnO_3$ compounds as a function of the average A-site atomic radius ($R_{0.7}A_{0.3}$) (30), (Reprinted from page 204 of ref(130).

6. EXPERIMENTAL METHODS

In the first part of this section, the details of the preparation of the double perovskite manganites used in the thesis are given. Then, general information about the measurement systems and methods used to determine the structural, electrical and magnetic properties of the produced samples were given. The choice of the method directly depends on the type of compound that we plan to synthesize. Also, each synthesis method has its limitations and imposes its conditions. Using the same method, the production conditions, namely the temperature, the atmosphere, the number of repetitions of certain stages (grinding, sintering for example, etc.) play a very important role in the stability and properties of the final product.

Before proceeding to the characterization of the magneto-transport properties, it is essential to go through the structural and microstructural characterization. Generally, X-ray diffraction XRD is used for structural characterization and for scanning microstructural characterization is scanning electron microscopy and X-ray energy dispersion microanalysis (EDX).

To prepare perovskite manganite compounds, solid-state reaction and sol-gel method are the most widely used ones. Both techniques are preferred due to their advantages such as easy production processes, cheap costs, achieving the desired particle sizes and obtaining a homogeneous compound. Homogeneous compounds are prepared by heat treatment at high temperatures following the method selected as the production technique. While solid-state synthesis is an easy and high-temperature technique; the sol-gel method requires some chemical synthesis procedures. In this thesis, samples were prepared by a solid-state reaction method.

6.1 Solid-State Synthesis Method (SSR)

Solid-State Synthesis Method (SSR), the most common, basic, and well-known fabrication method for synthesizing polycrystalline solids (powders), oxide ceramics, such as manganites. The solid-state reaction method has advantages according to the other methods in terms of the availability of the starting materials and the low cost of production. This method includes a repeated series of grinding,

pelletizing and heat treatment processes. Starting materials are generally oxides of the cations and carbonates, etc. As we know solids do not react with each other at room temperature (RT), so SSR consists of heat treatments which to overcome the kinetic barriers and to form the required product at elevated temperatures for the proper reaction. According to Tamman's law, a temperature of about two-thirds of the melting point is required to supply sufficient thermal energy that causes the ions to jump out of their normal lattice regions and diffuse through the crystal. Even at these temperatures, diffusion lengths are usually quite short. To avoid this situation, the starting materials are generally made into a fine powder; this reduces both the length of time that the ions must pass and increases the surface area for the reaction.

The purity of the starting materials is a prerequisite for obtaining appropriate results. This method includes a repeated series of grinding, pelletizing and heat treatment processes. For the process of manganites, the oxides and carbonates are firstly mixed and finely ground for good homogenization and to increase the inter-grain contact area. Then the mixture is subjected to a calcination step, in which the volatile constituents will be removed (carbon for example). The calcination temperatures are generally of the order of 1000 to 1400 °C. Then grinding, followed by palletization of the powder before sintering at a slightly higher temperature. The pelletizing process aims to ensure intimate contact of the grains. The sintering-milling cycle is generally repeated up to three times to obtain a good homogeneity in the composition of the material.

This very simple system requires some conditions to succeed in the synthesis as good control of the stoichiometry, careful monitoring, and determination of the temperature. This technique also has some disadvantages such as time dependency, high annealing temperature and excess contamination during the grinding and pelletizing process. We can obtain the grains in a millimetric dimension with this technique; additional applications to this technique are needed to obtain particles of smaller sizes (nanoscale).

All chemicals La_2O_3, $CaCO_3$, Gd_2O_3, Sm_2O_3, Nd_2O_3, Pr_2O_3, and MnO_2) were obtained commercially (>99.9 %, Alfa Aesar) and used without any purification. The highly purified oxides powders were mixed in stoichiometric ratios. Each mixture was ground and calcined at 900 °C for 14 hours for de-carbonation. After

a new grinding, the powder was compacted in the form of pellets 13 mm and a height of about 2 mm using a uniaxial press exerting a pressure of about 3 ton/cm². Then they were treated at 1050 °C for 20h, under air.

The same process was repeated for a temperature of 1100 °C and 1150 °C. To finish annealing at 800 °C for 20h was performed. The details of the preparation procedure of our samples are summarized in Figure. The samples were prepared in a high alumina combustion boat (Sigma Aldrich) using a high-temperature furnace (Protherm, PLF 150/5) which has controlled heating and cooling options with temperature stability of ±1 ℃.

Our research consists of twelve different double layer perovskite materials with different A-site radii and four samples in each group, with four Rare Earth (RE)substitution to A-site for the form of $A_3Mn_2O_7$- $(La_{1-y}RE_y)_{1.4}Ca_{1.6}Mn_20_7$ (RE: Pr, Nd, Sm, Gd). We determine three different A-site radii as $\langle r_A \rangle$ ≈1.3213, 1.3353, 1.3423 (Å). RE trivalent ions and AE divalent ions occupy the A-site perovskite together with "12-fold coordination, the smaller Mn ions (for mixed manganites Mn^{3+} -Mn^{4+}) is located in the centre of an oxygen octahedron, with a 6-fold coordination on the B side." In line with this information, we created 3 different groups using Shannon 12 cn ionic radius data (129). The radii of the elements we used can be displayed in Table 6.1.

Table 6. 1. Ionic radii for elements involved in the perovskite structure of manganites with 12 cn.

RE ions	**Radius (Å)**	**AE ions**	**Radius (Å)**
La^{+3}	1.36	Ca^{+2}	1.34
Pr^{+3}	1.29		
Nd^{+3}	1.27	**Mn ions**	
Sm^{+3}	1.23	Mn^{+3}	0.645
Gd^{+3}	1.21	Mn^{+4}	0.530

The first series consisting of 4 samples designated as Group I; the A-site radius is $\langle r_A \rangle$ ≈1.3213 (Å) and the compositions are as:

$(La_{0.6}Gd_{0.4})_{1.4}Ca_{1.6}Mn_2O_7$, $(La_{0.5}Sm_{0.5})_{1.4}Ca_{1.6}Mn_2O_7$, $(La_{0.34}Nd_{0.66})_{1.4}Ca_{1.6}Mn_2O_7$, $(La_{0.142}Pr_{0.857})_{1.4}Ca_{1.6}Mn_2O_7$.

The second series consisting of 4 samples designated as Group II; the A-site radius is $\langle r_A \rangle \approx 1.3353$ (Å) and the compositions are as;

$(La_{0.8}Gd_{0.2})_{1.4}Ca_{1.6}Mn_2O_7$, $(La_{0.75}Sm_{0.25})_{1.4}Ca_{1.6}Mn_2O_7$, $(La_{0.67}Nd_{0.33})_{1.4}Ca_{1.6}Mn_2O_7$, $(La_{0.57}Pr_{0.43})_{1.4}Ca_{1.6}Mn_2O_7$.

The last one also consisting of 4 samples and is denoted Group-III; the A-site radius is $\langle r_A \rangle \approx 1.3423$ (Å) and the compositions are as;

$(La_{0.9}Gd_{0.1})_{1.4}Ca_{1.6}Mn_2O_7$, $(La_{0.875}Sm_{0.125})_{1.4}Ca_{1.6}Mn_2O_7$, $(La_{0.833}Nd_{0.167})_{1.4}Ca_{1.6}Mn_2O_7$, $(La_{0.786}Pr_{0.214})_{1.4}Ca_{1.6}Mn_2O_7$.

6.2 Structural Analysis

The structural properties and magnetic properties of perovskite manganites are closely related to each other. Since the changes in the structural properties will also affect the magneto-electrical properties, the structural properties need to be examined in detail.

6.2.1 The X-Ray Technique

Following the discovery of X-rays by Roentgen in 1895, the first applications were oriented towards the study of crystals because it was hoped to highlight the constituent atoms of the molecules and would confirm both the accuracy of the Avogadro number. In 1912, the physicist Laüe determined with a crystal lattice the wavelength of X-rays. It, therefore, became possible to do the opposite.

X-rays are electromagnetic radiation with a high frequency of $3\ 10^{16}$ Hz to 10^{19} Hz and a wavelength of 10^{-11} m to 10^{-8} m. The energies vary from eV to several tens of MeV. The most popular applications are medical imaging and crystallography. The X-ray technique is very powerful in determining the crystal symmetry, the lattice parameters and the distribution of the atoms in the cell with very satisfactory precision, which creates a "valuable" set of structural information.

Table 6. 2. Detailed composite formulas to compare the materials used in the experiment between groups and their name abbreviations.

	$A_3Mn_2O_7$			
	Sample-1	**Sample-2**	**Sample-3**	**Sample-4**
	$(La_{1-y}Gd_y)_{1.4}Ca_{1.6}Mn_2O_7$	$(La_{1-y}Sm_y)_{1.4}Ca_{1.6}Mn_2O_7$	$(La_{1-y}Nd_y)_{1.4}Ca_{1.6}Mn_2O_7$	$(La_{1-y}Pr_y)_{1.4}Ca_{1.6}Mn_2O_7$
Gr-I	$(La_{0.6}Gd_{0.4})_{1.4}Ca_{1.6}Mn_2O_7$ Gr-I L**G**CMO	$(La_{0.5}Sm_{0.5})_{1.4}Ca_{1.6}Mn_2O_7$ Gr-I L**S**CMO	$(La_{0.34}Nd_{0.66})_{1.4}Ca_{1.6}Mn_2O_7$ Gr-I L**N**CMO	$(La_{0.142}Pr_{0.857})_{1.4}Ca_{1.6}Mn_2O_7$ Gr-I L**P**CMO
Gr-II	$(La_{0.8}Gd_{0.2})_{1.4}Ca_{1.6}Mn_2O_7$ Gr-II L**G**CMO	$(La_{0.75}Sm_{0.25})_{1.4}Ca_{1.6}Mn_2O_7$ Gr-II L**S**CMO	$(La_{0.67}Nd_{0.33})_{1.4}Ca_{1.6}Mn_2O_7$ Gr-II L**N**CMO	$(La_{0.57}Pr_{0.43})_{1.4}Ca_{1.6}Mn_2O_7$ Gr-II L**P**CMO
Gr-III	$(La_{0.9}Gd_{0.1})_{1.4}Ca_{1.6}Mn_2O_7$ Gr-III L**G**CMO	$(La_{0.875}Sm_{0.125})_{1.4}Ca_{1.6}Mn_2O_7$ Gr-III L**S**CMO	$(La_{0.833}Nd_{0.167})_{1.4}Ca_{1.6}Mn_2O_7$ Gr-III L**N**CMO	$(La_{0.786}Pr_{0.214})_{1.4}Ca_{1.6}Mn_2O_7$ Gr-III L**P**CMO

Besides, it can provide us with information about the internal stresses representing textural information.

The general method is to irradiate the sample with X-rays and look at the intensity which is diffused in different directions in space and analyze the resulting diffractograms. The scattered rays interfered to give maxima and minima in definite directions. This is the phenomenon of "diffraction". The recorded diffractograms make it possible to identify the present phases and to verify the purity of the samples.

Once X-rays are produced, we focus on a beam that strikes the surface of a crystalline or polycrystalline sample and interacts with its atoms. X-ray diffraction is established with destructive and constructive interference. This occurs only if Bragg's law is verified (eq.6.1)

$$2\,d\sin(\theta) = n\,\lambda \qquad (6.1)$$

λ: wavelength, n: integer, d (diffraction order): the distance between the crystal planes (see figure 5.1).

• If these waves arrive in phase opposition, their effects offset each other. The interference is destructive. It is reflected in the diffractogram by the bottom line of the signal.

• If these waves arrive in phase, their effects are added: the interference is constructive. It results in a peak in the diffractogram. The directions in which the interferences are constructive can be determined by the formula known as Bragg's law.

The result of multiple constructive diffractions is a diffractogram that contains a series of peaks. Each peak reflects a plan as shown in Figure.

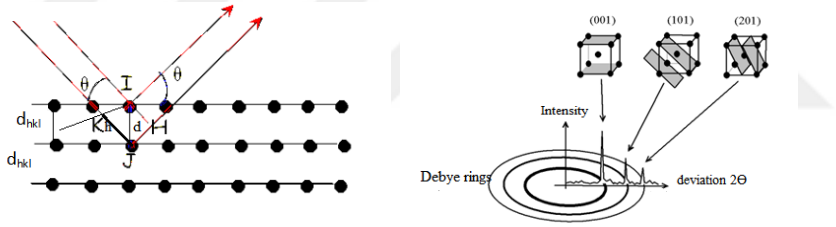

Figure 6. 1. Bragg's law and the association of a diffraction peak and a plane (*hkl*)

As for the X-ray source, it is formed by a vacuum tube associated with a device (filter + monochromator) allowing the selection of a single wavelength. The device contains three parts: the X-ray tube, the sample holder and the sensor. X-rays are produced by the impact of electrons accelerated by an electric field on a target called an anode. In the best cases, 1% of the incident energy is transformed into X-rays and the remaining 99% is transformed into heat, which requires the installation of an adequate cooling system. At the exit of the tube, the X-rays are channeled through a slit to prevent the sensor from considering the non-diffracted rays. Subject to rotate around the sample irradiated by a divergent beam, the sensor scans an angle whose measurement varies between 0 and 180 °. The records obtained are graphs where the intensity of the measured radiation is plotted as a

function of its position (θ or 2θ) and this according to the type of powder diffractometer used: "θ −θ" and "θ - 2θ".

• Diffractometer: "θ −θ": the sample holder is generally horizontal but necessarily immobile. The tube and the detector move symmetrically at the same angle.

• Diffractometer: “θ - 2θ” in this configuration, the X-ray emitter tube is kept fixed while the sample holder and the detector rotate in the same direction. However, when the first turn is by an angle θ, the second one turns by a measurement angle of 2θ.

In this thesis, we used the Rigaku powder X-ray diffractometer with Cu-Kα radiation (λ = 1.5418Å) type diffractometer. The samples were scanned with the conditions that an angular range between 20-80 ° in steps of 0.02 ° with a scan rate of 3◦/minute. Rietveld refinement was used to calculate the unit cell parameters.

6.2.2 Analysis and Exploitation of XRD Patterns

For analyzing data recording to the Rietveld method, we used the free software JANA2006 (130) to correct our results. It is software for analyzing crystallographic structures. This software can analyze multi-phase diffractograms. The Rietveld method is a powerful tool for structural analysis from powder diffraction data (Rietveld, 1967, 1969). The method allows the peak shapes of the Bragg reflections to be analytically defined and the width variations (FWHM) to be used with the diffraction angle 2θ. The analysis can be divided into separate steps that some of the ones depending on the correct completion of the previous one (s), often constitute an independent task to be completed by experimental methods. It can perform LeBail composition and assign to each peak the corresponding Miller indices (h, k, l). It presents the experimental curve superimposed on the calculated curve and gives on the same figure the difference between the two curves and the positions of the peaks of each phase. It refines the values of the approximate cell parameters entered initially (a, b, c, α, β, □). The refinement must be carried out a few times until the stability of the parameters of the refinement R_p and R_{wp}. A good refinement corresponds to Rp <10% and Rwp <20%. For such a value, the

calculated curve will be superimposed on the points observed and the difference between the experimental and calculated curves will be less than 10% in intensities.

6.2.3 Scanning Electron Microscope Imaging

A scanning electron microscope (SEM) is used for studying the surface topography microstructure, and chemistry of metallic and nonmetallic specimens based on electron-matter interaction. It can be producing high-resolution 3D images of the surface of a solid sample. The system is based on the principle of scanning with an electron beam at magnifications from 50 up to ~ 100, 000 X, with a resolution limit < 10nm (down to ~ 1nm), analyzing with different detectors and reconstructing an image of the surface.

Due to the interaction between the accelerated electron beam and the sample, the electron slowly decays in the solid and emits backlight in various ways. Low-energy Auger electrons arise because of non-elastic interference of the high-energy electrons beam with the outer orbiting electrons of the sample atoms. These electrons carry information about the surface of the sample and form the working principle of Auger Spectroscopy. Again, as a result of the interactions with the orbital electrons, electron beams emitted from their orbit or reduced in energy travel to the surface of the sample and accumulate on the surface. These electrons are called seconder electrons. The secondary electrons are collected in the scintillator in the sample chamber and converted into a secondary electron image signal (SEI). Secondary electrons are used to obtain a high-resolution topographical image of the sample as the sample surface comes from a depth of 10 nm or less.

Besides, in the sample, the characteristic X-rays and continuous rays also occur due to the non-elastic interactions between the sample atoms and the electron beam. Characteristic compositions provide information about the chemical composition of the sample when evaluated in wavelength or energy-dispersive X-ray analytical systems. (Figure 6.2). This method is known as Electron Microscope Analysis.

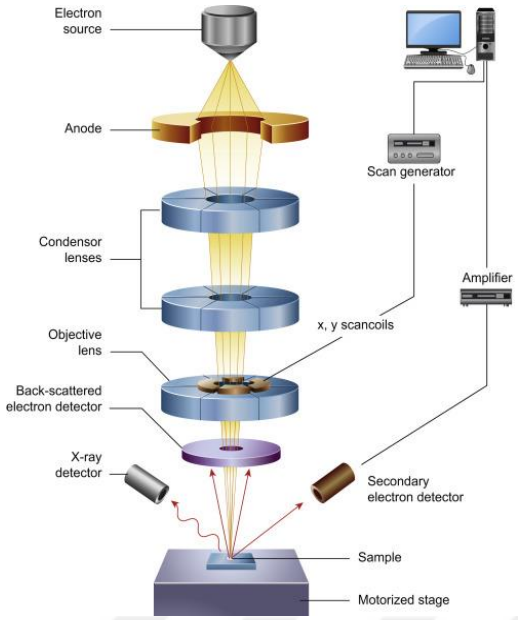

Figure 6. 2. Schematic diagram of the constitution of SEM

The electron beam focusing on the sample may also be inelastic interactions with the sample atoms. In these interferences, the beam electrons are scattered back from the sample surface by deflecting with the attraction force of the nuclei of the sample atoms. These electrons are called backscattered electrons (BSE). Such an image is referred to as the backscattered electron image. The number of electrons scattered back is proportional to the atomic number of the sample. The backscattered electrons come from the deeper region of the sample surface relative to the secondary electrons, so the diffraction power of the view is lower.

In this study for analyzing surface morphology and the grain size we used The JSM 6390 LV-JEOL model microscope at an acceleration voltage of 20 kV

6.2.4 X-Ray Spectroscopy (EDS)

The inelastic interaction (primary electron) - (sample atom) produces excited ionized atoms, called secondary electrons. These excited atoms return to the equilibrium state by rearranging their electronic procession. Meanwhile, when an electron passes from the outer layer to the other, an intense energy photon is emitted in the form of X-rays. This photon is a prominent feature of an atom because it corresponds to an energy difference between the two layers of this atom.

By equipping the SEM with a suitable detector, this radiation can be detected, recorded and analyzed. Thus, the chemical composition of the sample will be determined. As shown in Figure, it is noted that the X-ray penetration is deeper when compared to the electrons emitted backwards, so that this technique provides other information in the sample on the local constitution. The X-ray recording gives a diagram from which one can access a calculation of the proportions in the mass of each constituent. This calculation is based on the determination of the area under each peak.

For our samples, we used the same SEM equipped with an x-ray detector to investigate the basic composition and homogeneity of all samples utilizing quantitative energy-dispersive x-ray spectroscopy (EDS) with corresponding energy at 20.0 kV.

6.2.5 Magneto-Transport Character Analysis

The electrical resistance measurements as a function of the temperature or the magnetic field make it possible to determine the conduction mode of the materials, in particular, to characterize the insulating or conductive state. It is also possible to measure other important properties such as the density and nature of charge carriers, their mobility, the evolution of resistance and resistivity in the presence of a magnetic field. Magnetoresistance (MR) is the main characteristic studied in the field of manganites. It is calculated from resistances under or without a magnetic field. These measurements are fundamental to determine the conduction mechanism.

As an important feature, resistance-temperature measurements are also used to determine the phase transition temperatures. Due to the small resistance of the samples, the low contact resistance is desirable. To accomplish this requirement, we chose the standard four-probe method for measuring the resistance of the samples.

This technique consists of maintaining a continuous current at the edges of the sample and measuring the voltage. Subsequently, we deduce the resistance. To

measure resistance using this technique, the specimens were cut into rectangular bars. Silver paint is used for the electrical contacts of the probes with the sample. This silver paste is applied to the ends for current and voltage contacts. Because of much less resistance, thin copper strands are attached to the sample with silver paint. (Figure 6.3)

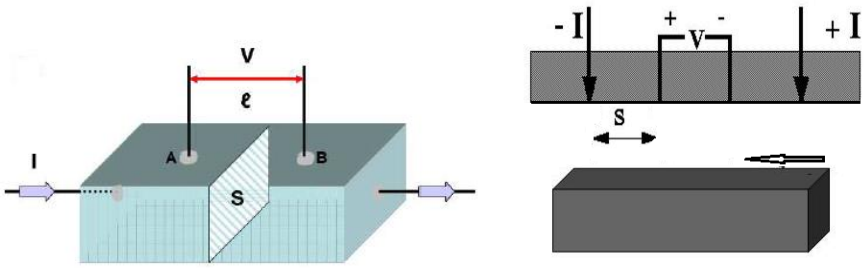

Figure 6. 3. Representation diagram of the 4-point method.

The resistance and magnetoresistance measurements of the materials at low and room temperatures were taken using a closed helium cryostat with a superconducting magnet solenoid (CRYO Industries - Model CF-2376-RTB). The magnet is a close-cycle cryocooled Nb_3Sn superconducting magnet and can apply a magnetic field of up to 7T. The temperature was controlled using Cryogenic Control Systems (Model 32B) with a stability of 3 mK at 300 K. The vacuum inside the cryo-cooler system was maintained with the Varian Vacuum Pumping System Model 969-8227.

The basic homemade ac susceptibility system consists of a coil system comprised of a primary field coil (solenoid) and two secondary pickup coils kept coaxially, which are used to measure the ac susceptibility signal. These pickup coils are made identical and connected in series opposition. In this case, if a sinusoidal current is passed through the primary coil the voltage induced across the pick-up coils is nearly zero. If the sample is placed in one of the pick-up coils a net voltage having the same frequency as the primary current will appear which is measured employing a lock-in amplifier. We have used the Stanford research system lock-in amplifier (SR850 DSP) for voltage measurement. We used the voltage across a resistor connected in series with the primary coil as the reference voltage of the

lock-in amplifier. Susceptibility is measured as a function of temperature for the materials. The samples under the present investigations were also characterized by this technique to determine the magnetic transition temperature.

To determine the magnetic phase and phase transition of the compounds, a hand-made ac-susceptibility system was used. This system consists of basically a primary field coil (solenoid) and two secondary pickup coils held coaxially. The Zero Field Cooling (ZFC) process was used to identify the phase transitions. For the ZFC process, the material is initially cooled to 20K from about room temperature without any field. Then susceptibility is measured as a function of temperature for the materials under a low voltage value (5mV). We have used the Stanford research system lock-in amplifier (SR850 DSP) for voltage measurement.

7. RESULTS AND DISCUSSION

This chapter is devoted to the presentation and analysis of the experimental results obtained for the three series of manganese oxides $(La_yRE_{1-y})_{1.4}Ca_{1.6}Mn_20_7$ (Re: Pr, Nd, Sm, Gd) with various ionic A-site radius, which is $\langle r_A \rangle$ ≈1.3213, 1.3353, 1.3423 (Å). The samples are in the same groups with the same $\langle r_A \rangle$ ionic radius by different fractional occupancy (1-y). It was attempted to obtain the same radius compounds by taking four different elements at different ratios within each group. Due to lanthanide contraction, the stable decrease in the size of the atoms and ions of the rare earth elements with increasing atomic number from lanthanum through gadolinium. Also, the ionic radii for La^{+3}, $Pr^{+}3$, Nd,$^{+3}$ Sm^{+3}, and Gd^{+3} were found as 1.36, 1.29,1.27, 1.23, and 1.21 (Å), respectively according to Shannon. For our compositions, the "big" La^{+3} ions were replaced with smaller ones. The calculations indicated that to obtain an equal A-site radius $\langle r_A \rangle$, a small amount of Gd^{+3} ion concerning Pr^{+3} ion was needed. For example, for Group-II compounds, Gd ratio is smaller than the Pr ratio (Chemical formulas for radius 1.3353 (Å) in Group-II as $(La_{0.8}Gd_{0.2})_{1.4}Ca_{1.6}Mn_2O_7$ and $(La_{0.57}Pr_{0.43})_{1.4}Ca_{1.6}Mn_2O_7$). (Table 6.2)

The analysis of purity, microstructure and magneto-transport properties were made by different methods. The purity of the compounds will be verified by the EDAX technique, the structural analysis by the XRD and the microstructure analysis by the SEM imaging. Then, by applying a magnetic field of 0.4 Tesla, electrical resistance measurements and magneto-transport characterization will be examined. The main characteristic of MR magnetoresistance will be calculated by analyzing these results. Finally, the mechanism and the interactions behind the different magneto-electrical behaviours were investigated.

7.1 Microstructural Analysis: X-Ray Diffraction (XRD)

XRD results of $(La_{1-y}RE_y)_{1.4}Ca_{1.6}Mn_2O_7$ samples were given in Figure 7.1-7.3-7.5. All diagrams were taken at room temperature, with a variation of 2Θ between 20° and 80° by a step of 0.03°. The diffractograms indicated that $La_{1.2}Ca_{1.8}Mn_2O_7$ has a tetragonal perovskite structure with a quadratic space group I4/mmm when the obtained results were compared to ICDD card no 095542 and JCPDS card no.41-1488.

The refinement of these high-resolution diffraction peaks was carried out by the Jana2006 software, based on the Rietveld method. The refinement results were also shown in Figures 7.2-7.4-7.6.

On each figure: the experimental points, the modelled curve, the difference between the experimental points and the calculated Bragg positions were presented. A summary table of the results of the refinements present, from one by the cell parameters of a, c and V with their uncertainties, and on the other hand, the factors R_P, R_{wp} and the GOF (goodness of fit) which estimate the quality of the refinement (Table 7.1). It can be said, these refinements; a very good superposition of the calculated curve is on the experimental points. This is confirmed by the values of R_p less than 10 (except Group-I LNCMO and Group-III LNCMO sample), R_{wp} less than 20 (except Group-I LNCMO sample) and those of goodness of fit (GOF) very close to 1 for all the compounds.

The very small peaks or the impurity phases were detected by refinement are mentioned in FIG. The X-ray diffraction patterns exhibit predominantly a single phase with tetragonal symmetry, still, a trace amount of minor impurity perovskite (La,Ca) MnO_3 phase. The X-ray diffraction patterns obtained at ambient conditions for $LaSr_2Mn_2O_7$ exhibited predominantly a single phase with tetragonal symmetry, still, a trace amount of minor impurity perovskite (La,Sr) MnO_3 phase (3%) was inferred, and it was excluded in the refinement cycles. These traces are usually encountered in this type of compound known by their difficulty of synthesis.

In the $La_{2-2x}Ca_{1+2x}Mn_2O_7$ system with a $Sr_3Ti_2O_7$-type structure, double perovskite layers are interleaved with La(Ca)O layers and Mn-O-Mn bonds in the c-axis direction are separated from one another by La(Ca)O layers.

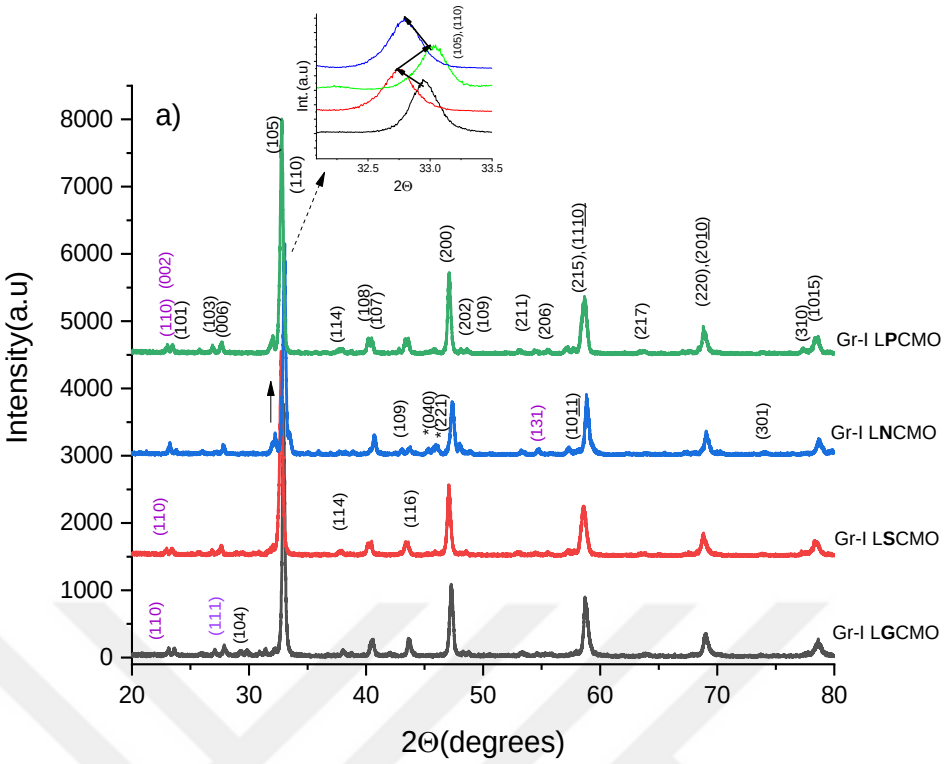

Figure 7. 1. X-ray diffraction pattern of the Group-I samples LGCMO, LSCMO, LNCMO, LPCMO. The enlarged view of the diffraction peaks of (105), (110) with maximum intensity located at 32°–34° degrees is showed to observe the shift occurring at the top.

Figure 7.1,7.3,7.5 indicates the XRD patterns of Group-I, Group-II and Group-III samples and the miller indices of the major Bragg reflections. They were drawn over each other to observe the harmony and incompatibility with each other. The XRD patterns were consistent with the previous reports and all samples shows characteristic main peaks near with miller index at $2\Theta = 23.5°$ (101), 27.07° (103), 27.8° (006), 32.89° (110), 32.90° (105), 37.3° (008), 37.9° (114), 40.3° (107), 43.6° (116), 47.21° (200), 47.22° (0010), 48.2° (202), 48.7° (109), 50.6° (118), 51.1° (204), 53.4° (211), 55.2° (213), 55.68° (206), 57.4° (00$\underline{12}$), 57.8° (1011), 58.74° (215), 58.75° (11$\underline{10}$), 61.7° (208), 63.7° (217), 68.89° (220), 69.09° (20$\underline{10}$), 72.4° (224), 73.79° (301), 78.69° (1015).

The reflections of Bragg position of secondary phase peaks were illustrated as the purple colour line.

In the upper part, the expanded peaks of (105) - (110) between 32-24° are to examine the shift in the diffraction pattern. This shift is not only for the widened part but behaves the same over the entire range.

Figures 7.2,7.4,7.6 display the Rietveld-refined XRD patterns of Group-I, Group-II- Group-III. Rietveld profiles have been drawn considering *I4/mmm* space group. It was shown as the observed (blue line), calculated (pink line). At the bottom, vertical bars represents the Bragg positions (black); and the (light blue) line shows the difference between the calculated and the observed diagram.

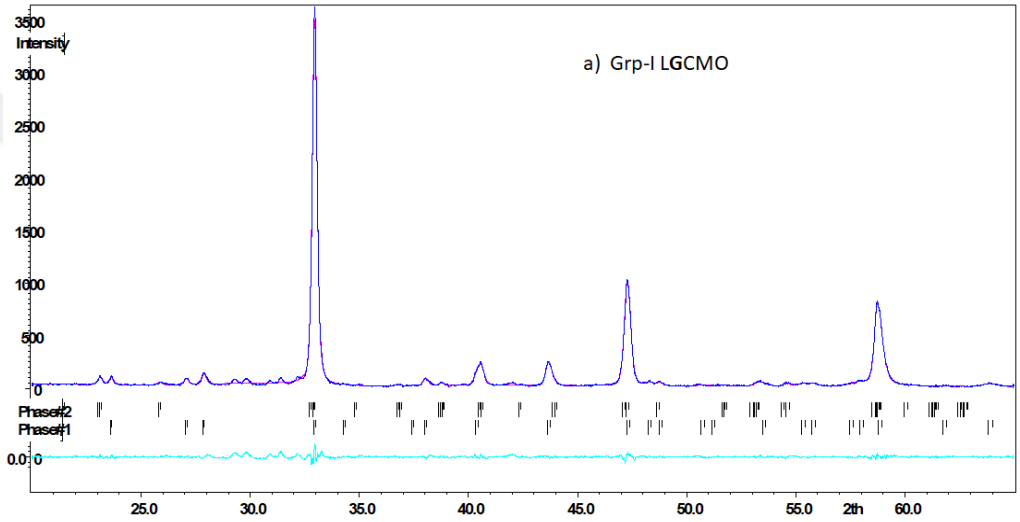

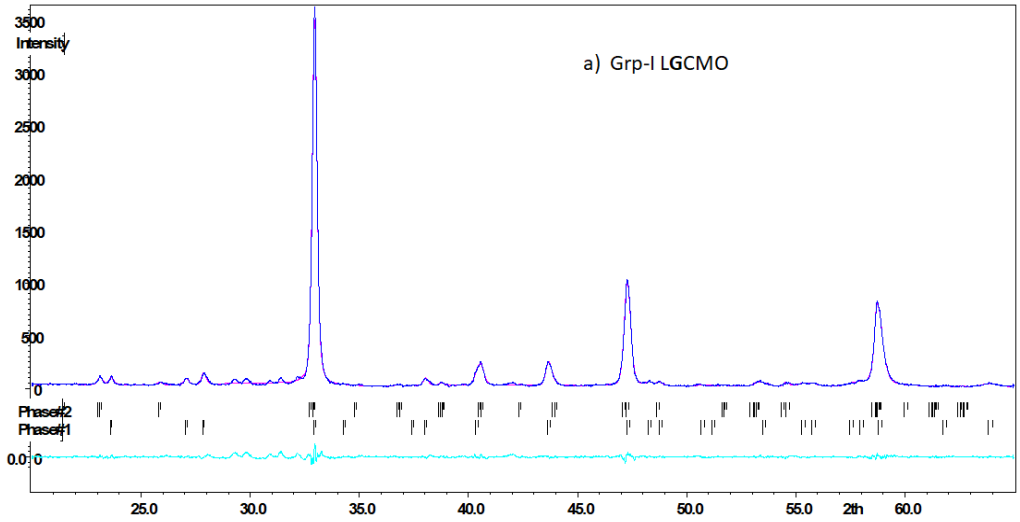

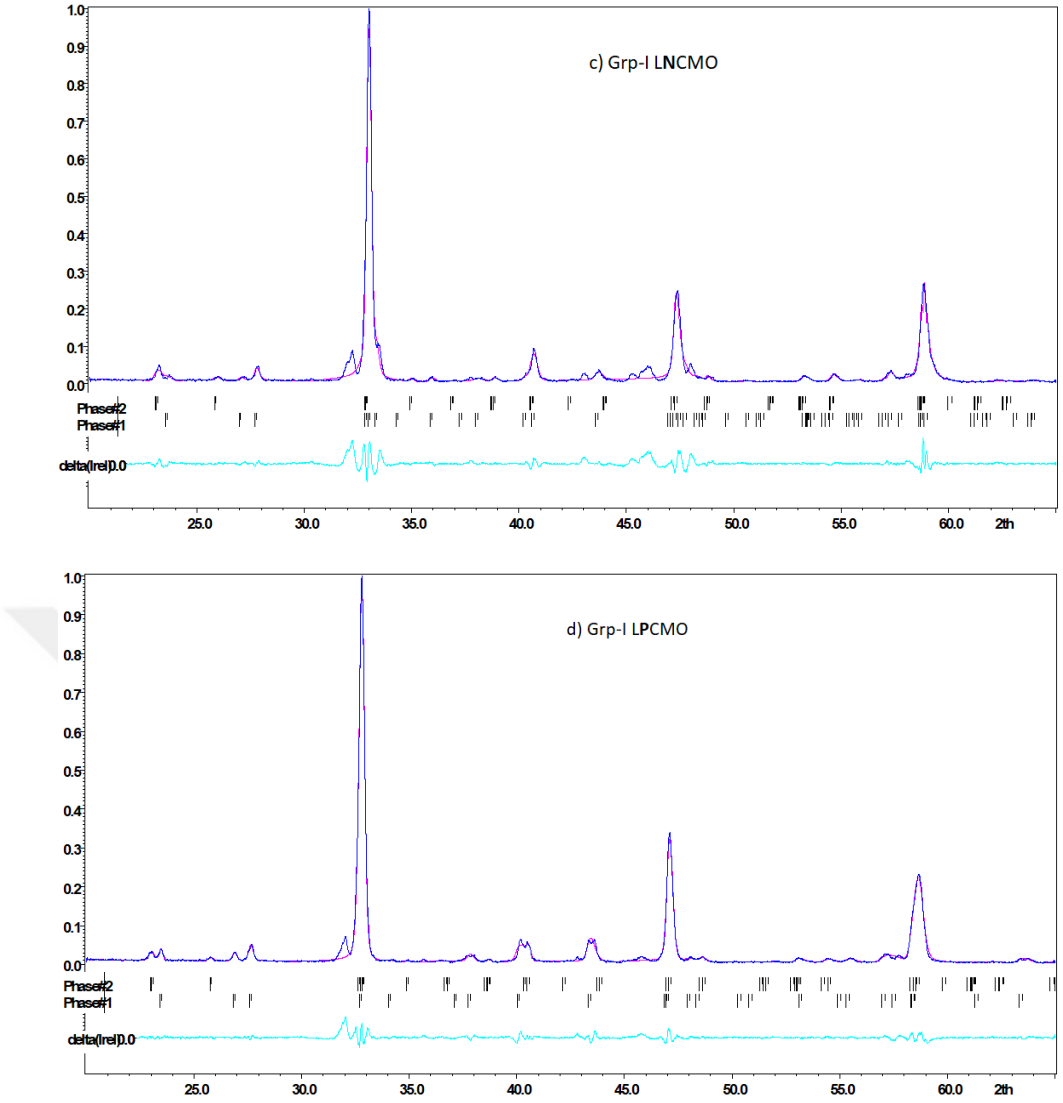

Figure 7. 2. Rietveld profiles considering *I4/mmm* space group for samples Group I a) LGCMO, b) LSCMO, c) LNCMO, d) LPCMO. The blue line indicates the observed data; the pink line (at the background) signs the calculated, modelled curl. At the bottom, vertical bars represent the Bragg positions (black); and the light blue line shows the difference between the calculated and the observed diagram.

Group-I LGCMO, LSCMO LNCMO and LPCMO sample have some prominent different phases unlike the main phase as at 2Θ= 23.02°(110) (002), 25.8° (111) and 54.6° (131). They were signed in purple colour. The peaks (105) and (110), which are characteristic and have the maximum intensity and so have been drawn also as enlarged. LGCMO and LNCMO samples are compatible with each other and the main phase, while LSCMO and LPCMO samples show a more compatible situation with the second phase. Likewise, the other two maximum

intensity brag positions (00$\underline{10}$)-(200) and (11$\underline{10}$)-(215) are in agreement with the main phase (phase1) for them LGCMO and LNCMO. There are impurity phases in the range of 29° to 32° in LGCMO. It can be said that there are no pollution phases in LSCMO. The LNCMO has some impurity peaks at between 31.8° and 32.4°; 45.2° and 46.4°. The *(040) and (221)* peaks should be a reflection of the MnO_2 layer .ref. The LPCMO has also the impurity phase at 2Θ=31.6° and 32.2 °. (The small impurity peaks of *(040) and * (221) observed in Gr-I LNCMO samples could be un-reaction $CaCO_3$ powder (131).

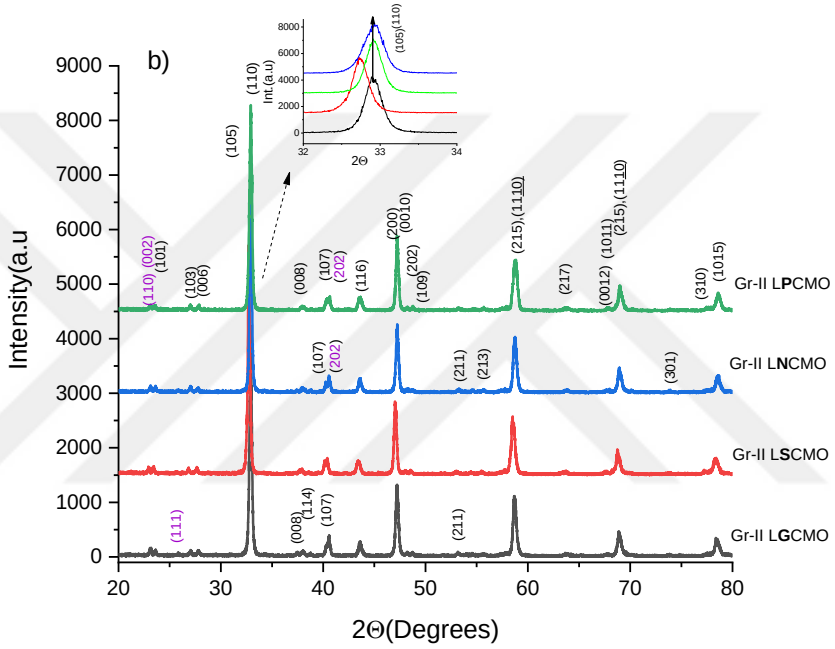

Figure 7. 3. X-ray diffraction pattern of the Group-II samples LGCMO, LSCMO, LNCMO, LPCMO. The enlarged view of the diffraction peaks of (105), (110) with maximum intensity located at 32°–34° degrees with maximum intensity is showed to observe the shift occurring at the top.

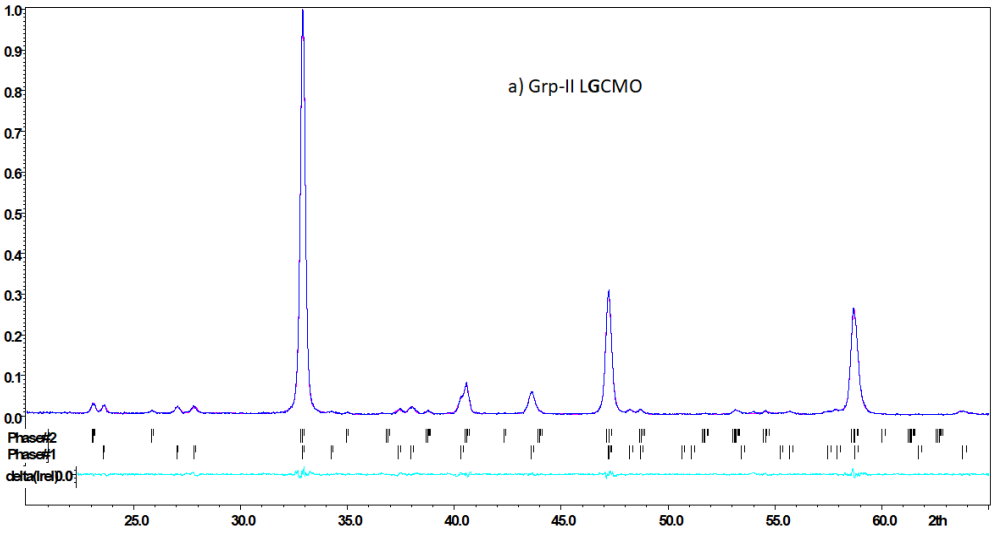
a) Grp-II LGCMO
Phase#2
Phase#1
delta(Irel)0.0
2th

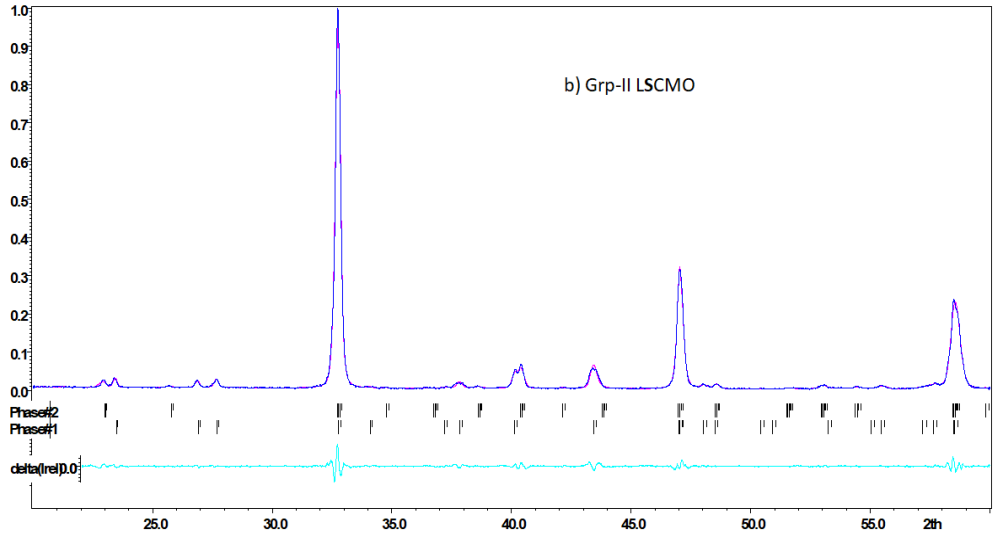
b) Grp-II LSCMO
Phase#2
Phase#1
delta(Irel)0.0
2th

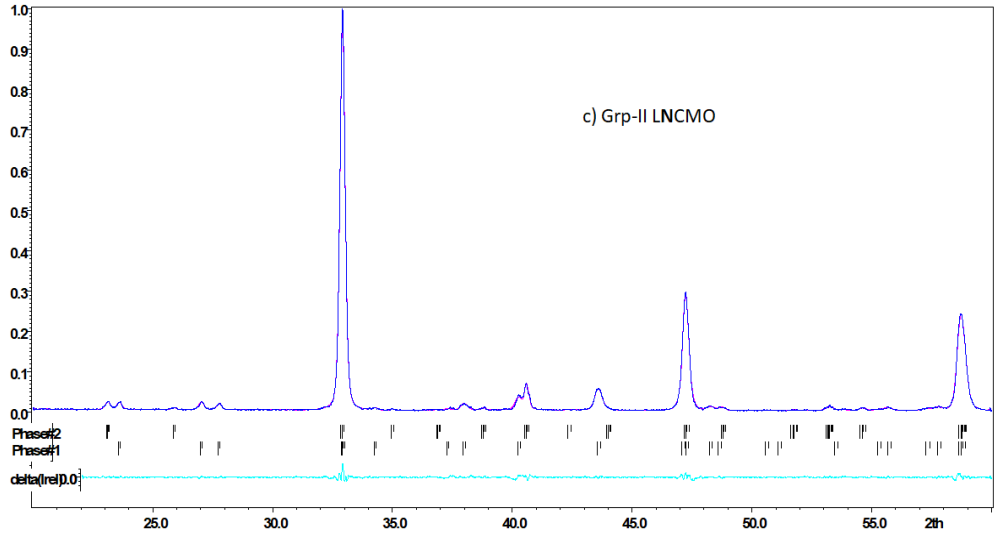
c) Grp-II LNCMO
Phase#2
Phase#1
delta(Irel)0.0
2th

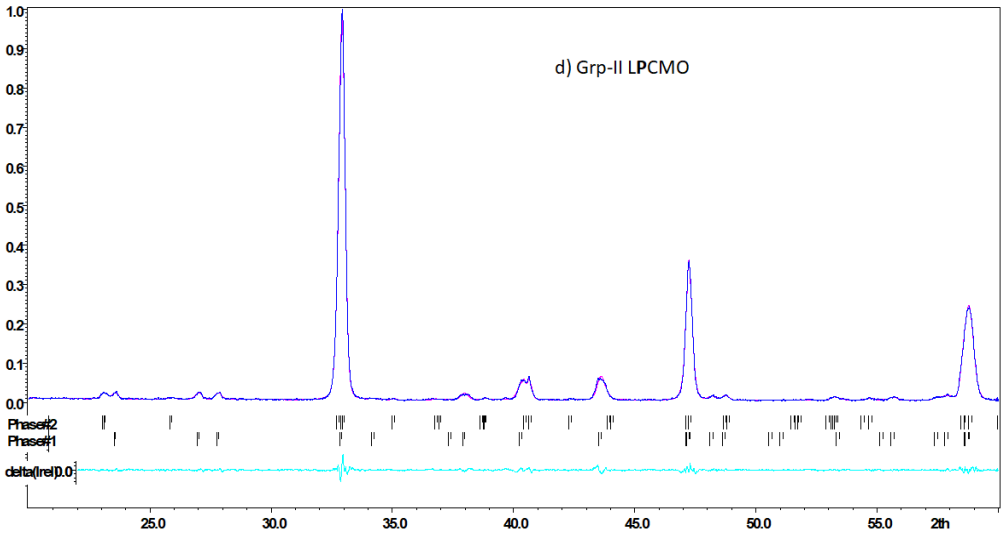

Figure 7. 4. Rietveld profiles considering *I4/mmm* space group for samples Group II a) LGCMO, b) LSCMO, c) LNCMO, d) LPCMO. The blue line indicates the observed data; the pink line (at the background) signs the calculated, modelled curl. At the bottom, vertical bars represent the Bragg positions (black); and the light blue line shows the difference between the calculated and the observed diagram.

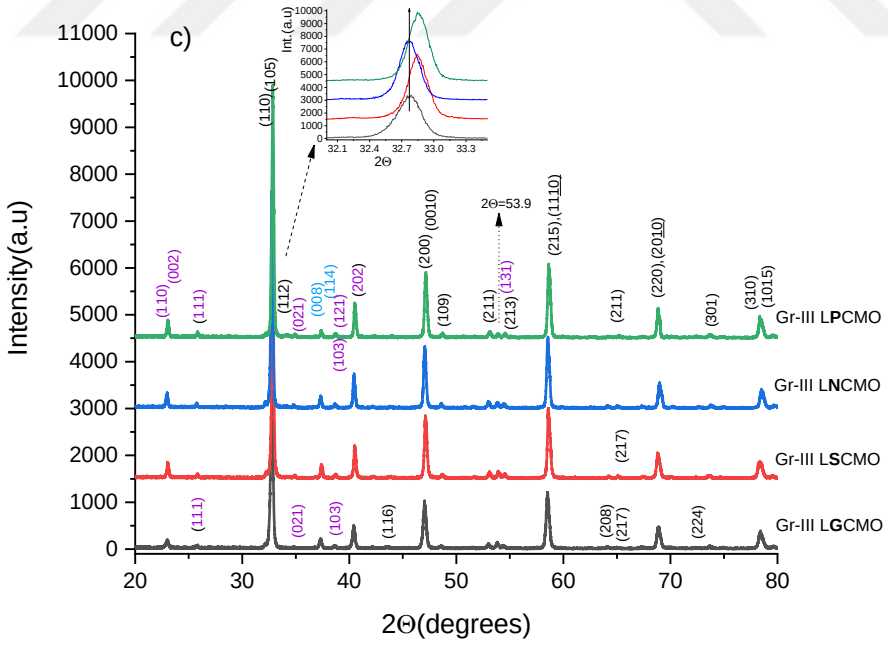

Figure 7. 5. X-ray diffraction pattern of the Group-III samples LGCMO, LSCMO, LNCMO, LPCMO. The enlarged view of the diffraction peaks of (105), (110) with maximum intensity located at 32°–34° degrees with maximum intensity is showed to observe the shift occurring at the top.

When the XRD diffraction graphs of the materials in Group-III are examined, we see that there are many secondary phase peaks thanks to the Rietveld analysis (The peaks was shown in purple colour on the graphics.) Also, we can see that the (006) peak does not occur on the XRD data for this group compositions. At the same time, we can say that all the materials show a peak at 2Θ= 53.9 °, unlike the other group. We can say that the major peak shifts to the left in LGCMO and LNCMO. The phase shift in detail will be examined in figure 7.7.

It was observed that peaks (008) and (114) did not form and a different peak was observed between the two LNCMO and LPCMO. This situation can be seen as significant in the Rietveld analysis. It may have occurred as a result of the phase shift with the peaks being transformed with each other. The XRD data of Group-III shows that the structural change could be seen very clearly.

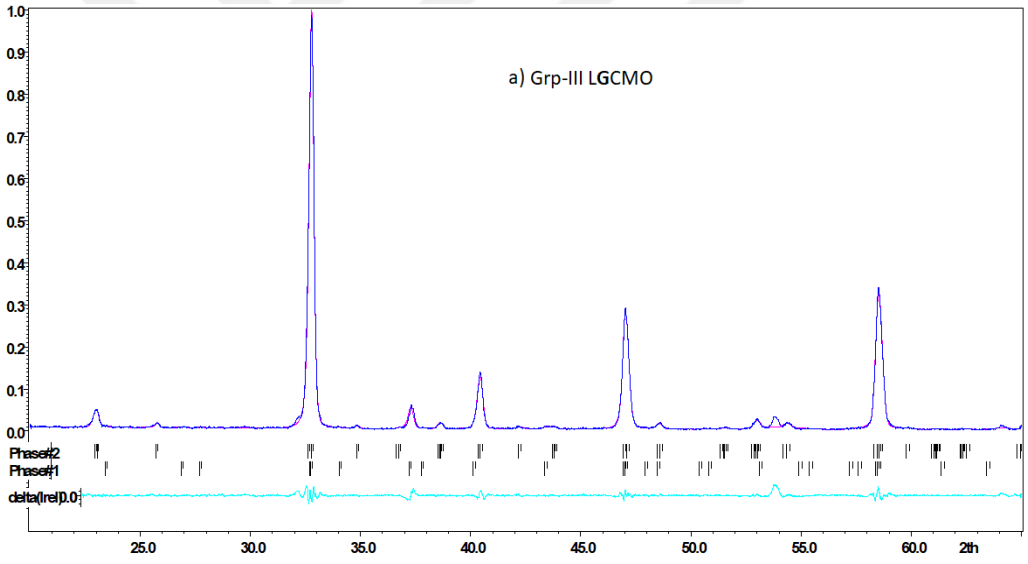

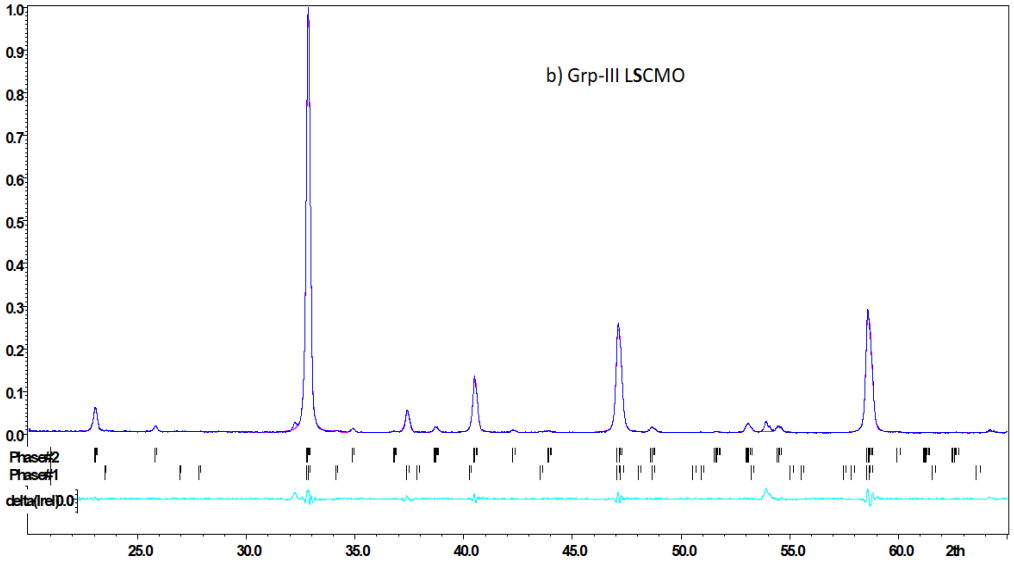
b) Grp-III LSCMO
1.0
0.9
0.8
0.7
0.6
0.5
0.4
0.3
0.2
0.1
0.0
Phase#2
Phase#1
delta(Irel)0.0
25.0
30.0
35.0
40.0
45.0
50.0
55.0
60.0
2th

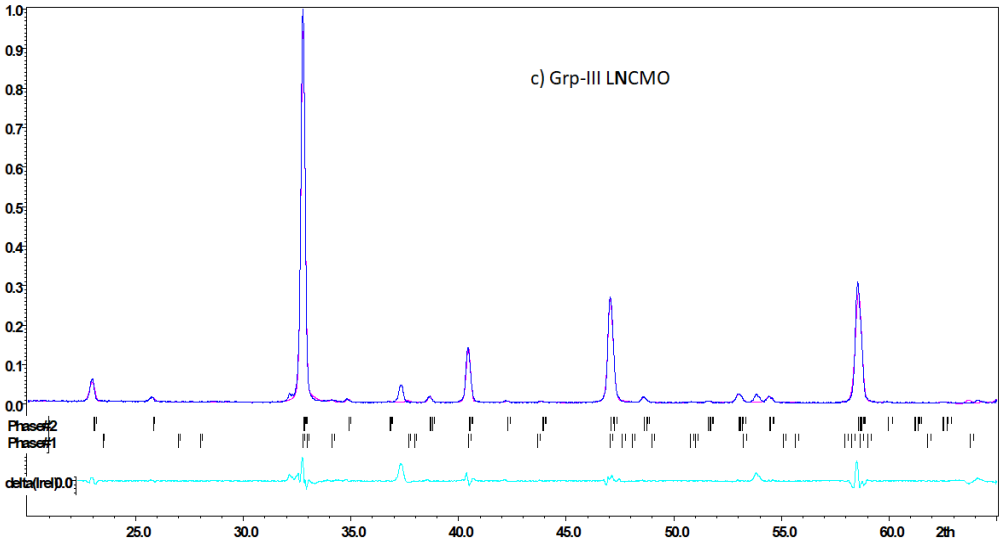
c) Grp-III LNCMO
1.0
0.9
0.8
0.7
0.6
0.5
0.4
0.3
0.2
0.1
0.0
Phase#2
Phase#1
delta(Irel)0.0
25.0
30.0
35.0
40.0
45.0
50.0
55.0
60.0
2th

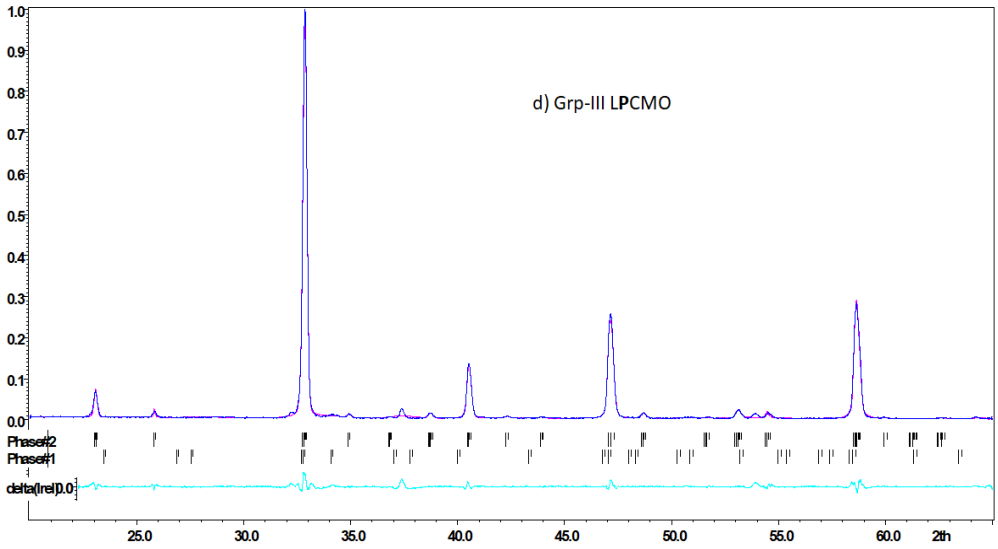

Figure 7. 6. Rietveld profiles considering *I4/mmm* space group for samples Group III a) LGCMO, b) LSCMO, c) LNCMO, d) LPCMO. The blue line indicates the observed data; the pink line (at the background) signs the calculated, modelled curl. At the bottom, vertical bars represent the Bragg positions (black); and the light blue line shows the difference between the calculated and the observed diagram.

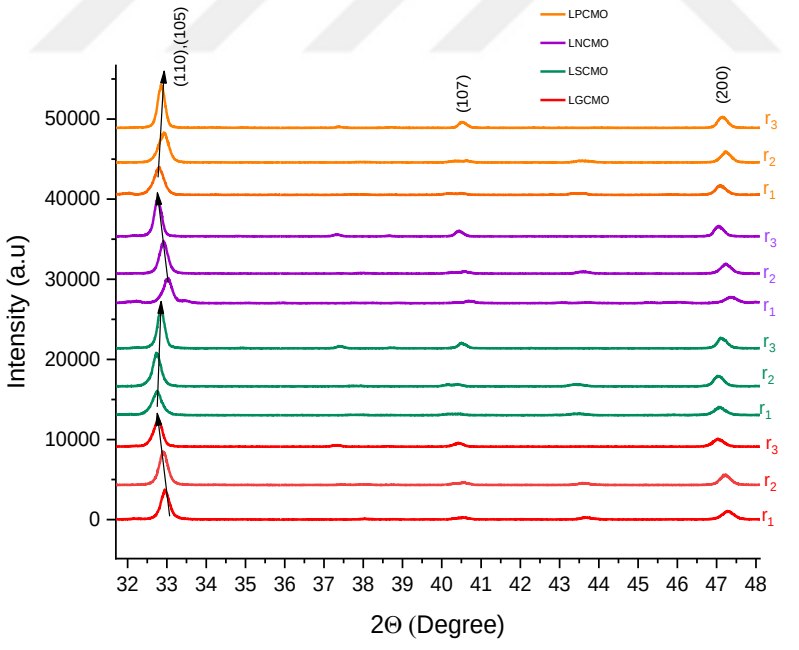

Figure 7. 7. Extended XRD diagram between 32 and 42 degrees to examine the variation of compounds obtained by substitution Gd, Sm, Nd, Pr as the form of $(La_yRE_{1-y})_{1.4}Ca_{1.6}Mn_2O_7$ according to three different radii (r_1, r_2, r_3).

Figure 7.7 is given together to examine the variation of LGCMO, LSCMO, LNCMO and LPCMO compounds concerning the radius. r_1, r_2, r_3 denotes 1.3213 Å, 1.3353 Å, 1.3423 Å, respectively. The enlarged diagram shows the selected two major Bragg peaks (110)-(105) and (215) -(11$\underline{10}$). As $\langle r_A \rangle$ increases, the amounts of RE in the compound (Gd, Sm, Nd and Pr) fall by half and the amount of La increases. (Table 5.2) (Gr-I LSCMO, Gr-II LSCMO, Gr-III LSCMO). The XRD peaks in the patterns shift continuously shifts to the left for Gd and Nd addition; LGCMO and LNCMO. Also, in other aspects the XRD patterns of compounds of LSCMO and LPCMO shift to the right.

Table 7. 1. Rietveld refinement parameters of XRD pattern and the obtained experimental data of samples

Parameters of refinement												
Structure **T e t r a g o n a l e**												
Space Group ***I4 / m m m***												
<r_A> (Å)	***<r_A>=1.3213 (r_1)***				***<r_A>=1.3353 (r_2)***				***<r_A>=1.3423 (r_3)***			
	LGCMO	**LSCMO**	**LNCMO**	**LPCMO**	**LGCMO**	**LSCMO**	**LNCMO**	**LPCMO**	**LGCMO**	**LSCMO**	**LNCMO**	**LPCMO**
a(Å)	**3.844025**	**3.857851**	**3.849543**	**3.869816**	**3.847302**	**3.861669**	**3.848149**	**3.854750**	**3.869985**	**3.859642**	**3.860291**	**3.863264**
Δa	0.000265	0.000347	0.000376	0.000509	0.000183	0.000184	0.000281	0.000235	0.000208	0.000207	0.000207	0.000864
c(Å)	**19.22056**	**19.29455**	**19.30577**	**19.38771**	**19.22711**	**19.30109**	**19.27587**	**19.26630**	**19.29206**	**19.25902**	**19.08335**	**19.41625**
Δc	0.00166	0.00166	0.00188	0.00287	0.00107	0.00132	0.00150	0.00137	0.00113	0.00116	0.00131	0.00675
c/a	**5.00011**	**5.00137**	**5.01508**	**5.00998**	**4.99756**	**4.99812**	**5.00913**	**4.99807**	**4.98505**	**4.98985**	**4.94350**	**5.02587**
V(Å^3)	**284.0132**	**287.1611**	**284.7388**	**290.3403**	**284.5945**	**287.8273**	**285.4420**	**286.2798**	**288.9330**	**286.8985**	**284.3772**	**289.7838**
ΔV	0.0331	0.0338	0.0380	0.0687	0.0215	0.0190	0.0367	0.0265	0.0206	0.0271	0.0273	0.1111
⟨D⟩(nm)	**29.95**	**26.79**	**33.04**	**26.96**	**32.66**	**35.03**	**34.48**	**28.19**	**32.28**	**40.63**	**39.15**	**38.81**
GOF	**1.05**	**1.14**	**1.96**	**1.44**	**0.70**	**0.91**	**0.73**	**0.76**	**1.05**	**1.08**	**1.77**	**1.36**
Rp	**6.97**	**9.21**	**15.20**	**9.53**	**4.61**	**6.89**	**4.97**	**5.11**	**7.07**	**6.57**	**11.16**	**8.31**
Rwp	**11.42**	**12.89**	**22.49**	**15.65**	**7.62**	**9.46**	**7.88**	**7.99**	**12.43**	**11.94**	**19.90**	**14.68**

These lattice constants (a,c, V) are obtained according to the Rietveld refinement and the Pseudo-Voigt profile functions are modelled for the XRD peak profiles. The result is close to that is found by several groups for lanthanum-based double perovskites (132–134). As we mentioned before; according to Shannon (129), the radii of rare-earth ions decrease from La^{+3}, Pr^{+3}, $Nd,^{+3}$ Sm^{+3} to Gd^{+3} respectively as 1.36 Å, 1.29 Å,1.27 Å, 1.23 Å, to 1.21 (Å). By then partial substituting on the La site of the undoped compound; the amount of La (1-y=y^) is higher in the LGCMO compounds compared to the LPCMO compounds to get the same radius on the one Group. (exp. Grp-II) $(La_{0.8}Gd_{0.2})_{1.4}Ca_{1.6}Mn_2O_7$-$(La_{0.57}Pr_{0.43})_{1.4}$ $Ca_{1.6}Mn_2O_7$)

Figure 7.8 is created to examine the variation of Lattice parameters according to the amount of La (y^).

The fitting results of cell parameters of all samples are listed in Table 6.1 The variations in the ratio c/a show us whether there is more shrinkage in the c or a direction. There is no specific change in lattice parameters, but any increase or decrease could be attributed to any change of the Mn-O bonds & Mn-O-Mn angles and JahnTeller distortion in the MnO_6 octahedron as reported by Luo et al. (135). This distortion of MnO_6 octahedra in the perovskite block effect of the electron-phonon coupling via the strengthening of the cooperative Jahn-Teller distortion which may have an obvious effect on the transport and magnetic properties of the DL manganites.

The average crystallite size ⟨D⟩ estimated from the maximum intensity peak of XRD data (Miller index of (106)), on Bragg angle 2Θ=32.79° and using Debye-Scherer's formula (136) and also listed in Table 6.1.

⟨D⟩ = kλ/ßcosΘ where ⟨D⟩ is average crystallite size in Å, k is the shape factor (generally taken as 0.89), λ is the wavelength of the X-ray ($\lambda_{Cu\text{-}Ka}$ = 1.5418 Å) and ß is the corrected full width at half maximum (FWHM) and Θ is the Bragg angle of diffraction. The size of average crystallite size seems to be mostly compatible with the average A site cation radius and we can say that the samples in Group-III have the largest ⟨D⟩. (32.28 nm, 40.63 nm, 39.15 nm, 38.81nm for Grp-III LGCMO, LSCMO, LNCMO, LPCMO, respectively.)

Further, the lattice contraction on replacing the larger lanthanide ion with the relatively smaller lanthanide ion can induce chemical pressure and increase the degradation of the MnO_6 octahedra in the perovskite block. This enhances the electron-phonon pairing through the enhancement of the common Jahn-Teller distortion, which can have a notable effect on the transport and magnetic properties of DL manganites.

7.2 Microstructural Analysis: Scanning Electron Microscopy (SEM)

The surface morphology of all samples is shown in Figure 6.9 with 5000x magnification at room temperature

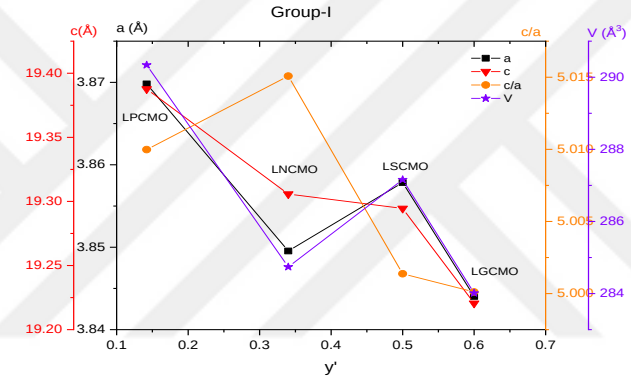

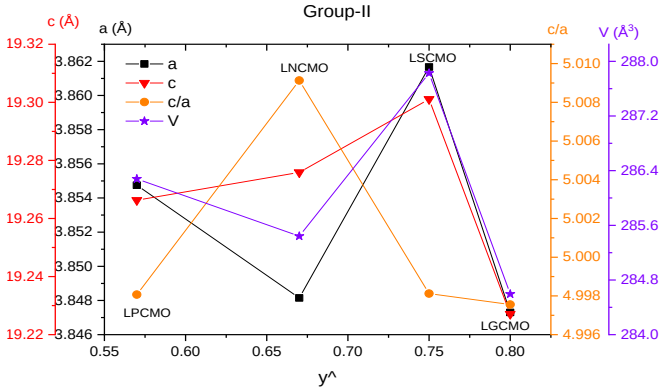

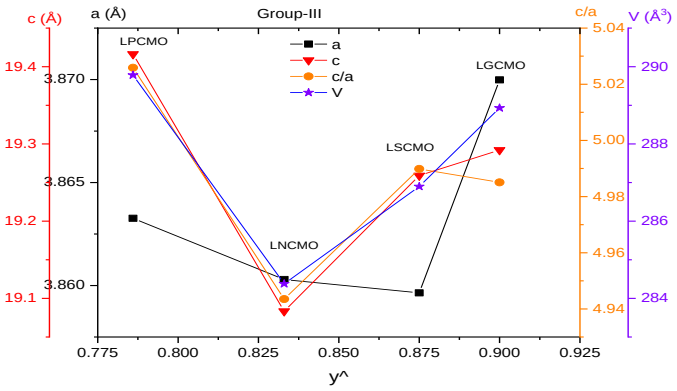

Figure 7. 8. Variation of lattice parameters a,c and unit cell volume (V) as a function of the La ratio (y^) on the compound for Group- I, Group-II and Group-III.

They are allowed us to discuss their morphological states and to estimate their microstructural parameters. Microstructural parameters also have a direct and significant effect on the magneto-resistance properties.

These SEM images show the granular and porous nature of all compounds. (Figure 7.9). Their porosity is obvious. Granulite is found everywhere in micrographs of single or double perovskite manganites prepared under similar conditions. They show the particle size distribution is almost homogenous and granular with spherical shape and the mean particle sizes ranging between $1\mu m$ and 5 μm values could be seen obviously for all the samples. From SEM micrographs of samples, the result of variation on the average A-site ionic radius $\langle r_A \rangle$ could be observed. As the images show, the average grain size values are close to each other in the same group, i.e. in the same A-site ionic radius $\langle r_A \rangle$ and get larger with an increase in the A-site ionic radius which is consistent with the X-ray diffraction results of an increase in crystallite sizes. And also porous structure decreases to a minimum in the Group-III samples' structure. The corresponding energy dispersive X-ray analysis (EDX) spectrum confirmed the characteristics of all elements present in all samples and showed in Table 7.2. and Figure 7.12. It is seen that each of the rare earth (Gd, Sm, Nd, Pr) weight fraction decreases gradually from Group-I to Group-III while La concentration increases as the chemical formulation.

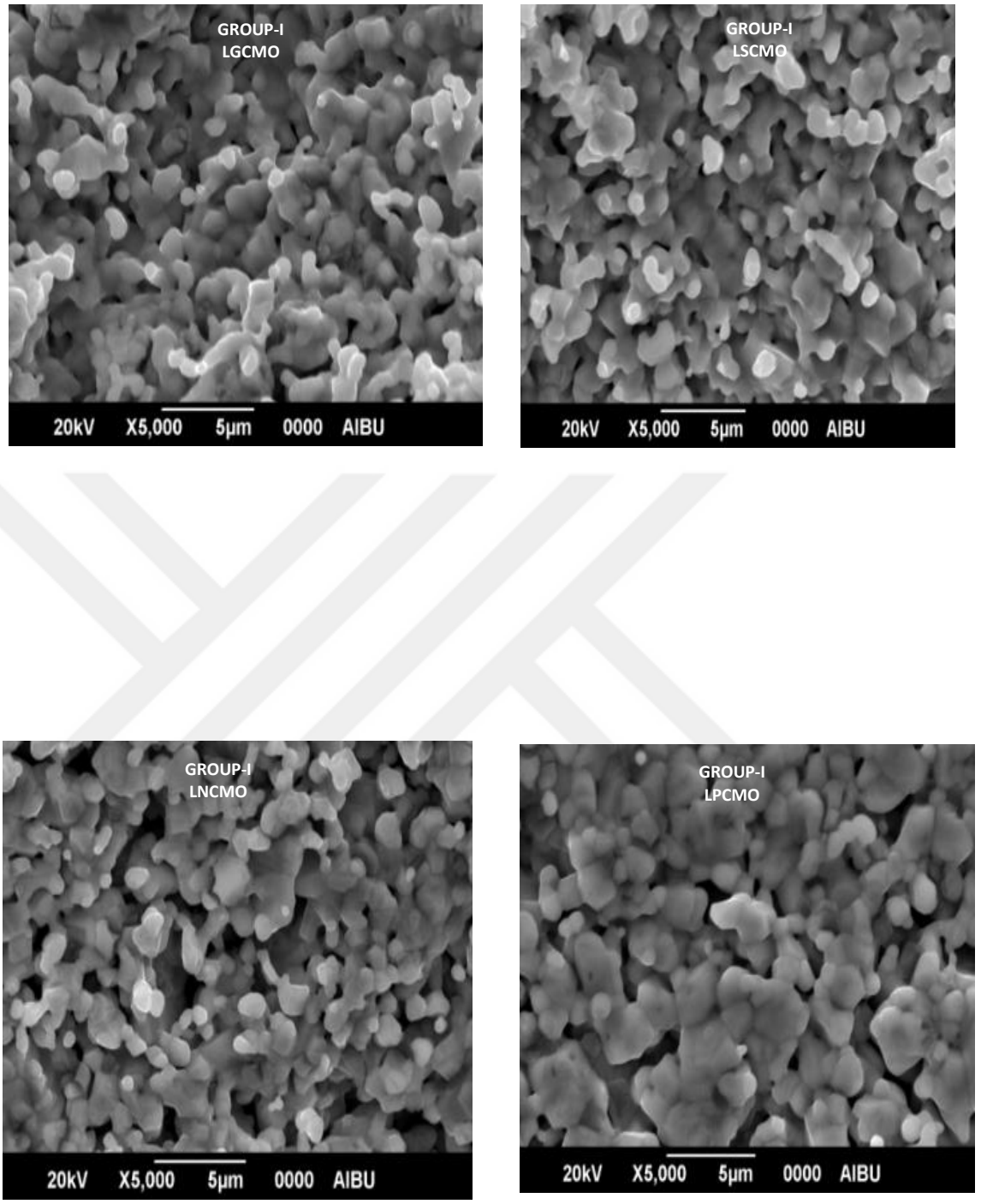

Figure 7. 9. Scanning electron microscopy (SEM) images of the Group-I samples LGCMO, LSCMO, LNCMO, LPCMO.

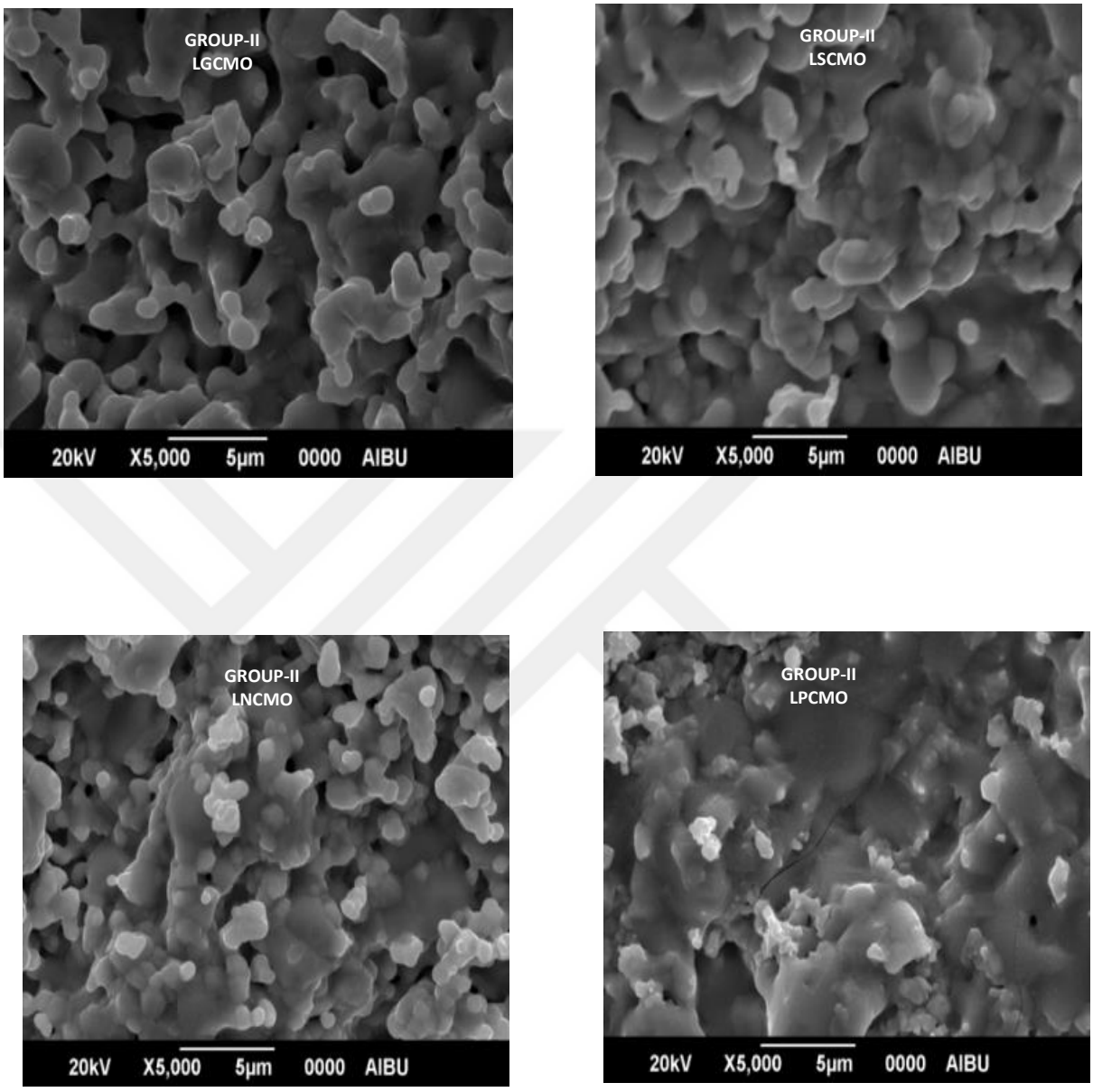

Figure 7. 10. Scanning electron microscopy (SEM) images of the Group-II samples LGCMO, LSCMO, LNCMO, LPCMO

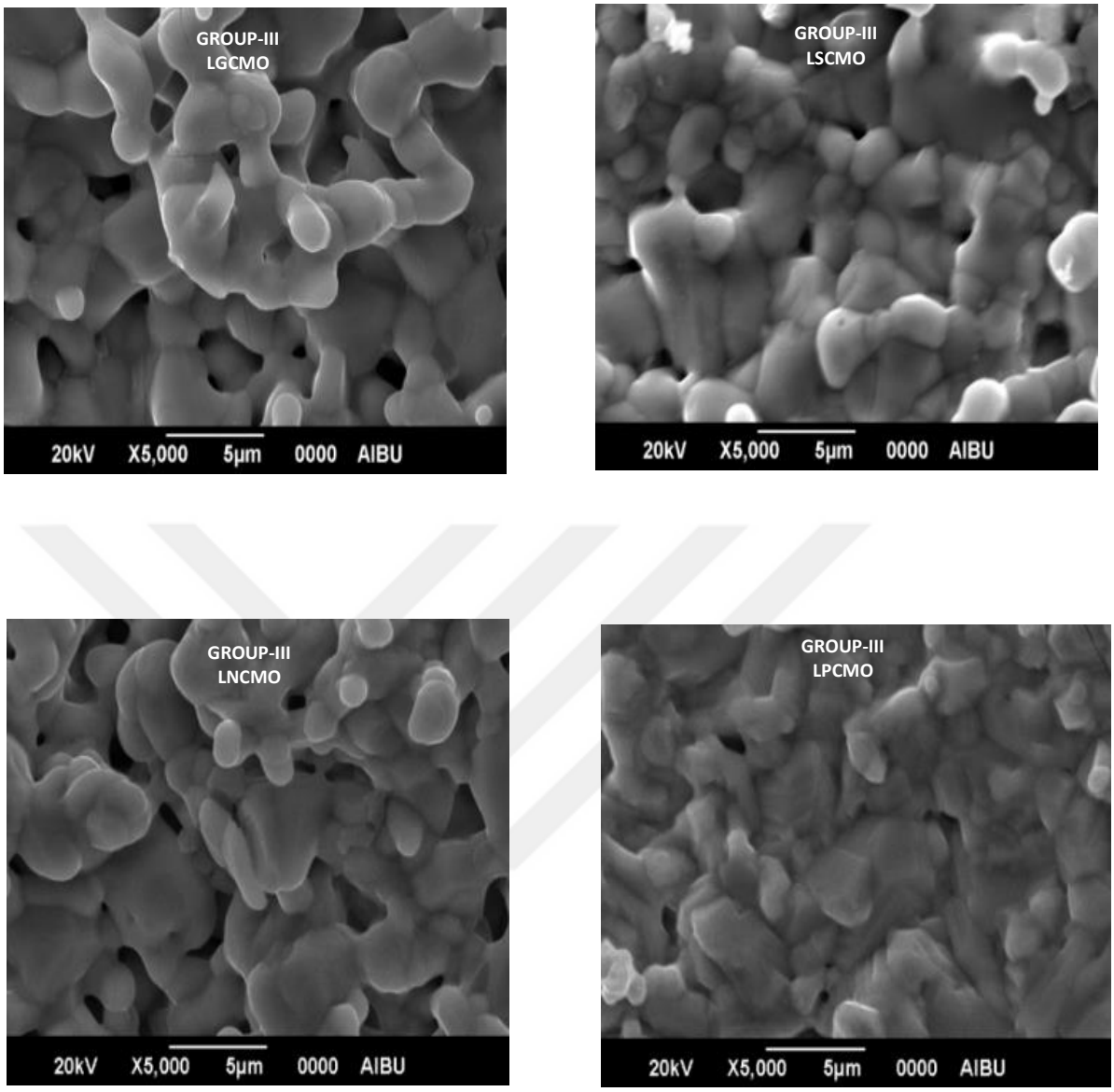

Figure 7. 11. Scanning electron microscopy (SEM) images of the Group-III samples LGCMO, LSCMO, LNCMO, LPCMO

We used the photon energy scatter microanalysis (EDX) technique to complete the microstructural study of our samples. The aim is to ensure the purity of the compounds, from the point of view of constituent elements and their relative rate of presence. The application of 20kV to the electron beam bombarding the sample is largely sufficient for their impact to cause the characteristic X-ray emission of all the elements constituting our samples, (Table 7.2). The obtained information concerns a depth of the order of one micrometre below the surface of

the compounds. The characteristic X-ray spectra of the samples are shown in Figures 7.12. These figures show, narrow, separated and very clear peaks. This reflects the good quality of these spectra. All elements La, Ca, Mn, O and Rare earth elements (Gd, Sm, Nd, Pr) are present. All peaks of considerable size are covered.

In three groups the smallest radius one (1.3213 Å) has the chemical formulation $(La_{1-y}RE_y)_{1.4}Ca_{1.6}Mn_20_7$ (RE: Gd^{+3}, Sm^{+3}, Nd^{+3}, Pr^{+3}) needs to maximum the doping ratios (y) (y=0.4, 05, 0.66, 0857) for rare earth elements, respectively, compared to the other groups. The bilayered perovskite compounds $(La_{1-y}RE_y)_{1.4}Ca_{1.6}Mn_2O_7$ were formed by partial replacing the greater radius La^{+3} ions (1.36Å) with the smaller radius rare earth (1.21, 1.24, 1.27, 1.29 Å). We can calculate that the adding ratio (y) of Rare Earth elements is getting smaller to adjust for the bigger A-site radius. For example, If we examine the LNCMO compositions; the Nd^{+3} content of 23.337% for Gr-I; 10.989 % for Gr-II and 4.73910 % for Gr-III; so, EDAX results also confirm the chemical composition. (Table 7.2)

Besides, the EDX results also confirm that RE^{3+}s have replaced La^{3+}; the Mn, Ca, O percentage weigh ratios which are almost constant versus increasing or decreasing La^{3+} and RE^{3+} amounts as a variation of A-site radius.

7.3 Cation Size Variance Effect

"Size variance effect" or "cation mismatch" (σ^2) indicates a disorder of the cations (RE^{+3} or AE^{+2}) with different sizes distributed according to their location, A-site or B- site. The variance (σ^2) in the distribution of $\langle r_A \rangle$ or $\langle r_B \rangle$ has been used to quantify the lattice mismatch by the following equation. It is a quantification of the size mismatch between the dopant and host cations (La^{3+}, Ca^{3+}) and the associated elastic energy minimization by pushing the larger or smaller dopant to free surfaces or interfaces (136)(137). The A site variance was examined because of the partial substituting to La Site. It can be shown as a formulation of that;

$$\sigma_A^2 = \langle r_A^2 \rangle - \langle r_A \rangle^2 \quad (7.1)$$

$$\sigma_A^2 = \sum y_i \, r_i^2 - \langle r_A \rangle^2 \quad (7.2)$$

where $\langle r_A \rangle$ defined as $\langle r_A \rangle = \sum y_i r_i$ and $\sum_i y = 1$ in which r_i is the corresponding ionic radii ; y_i is the fractional occupancy of the i^{th} atoms of A site (138). As can be seen in the equation 6.1 and 6.2, the variation is due to the difference in the ratio (y_i) and radius of the substituted cation for the same A-site radius. The calculated values are listed in Table 6.4.

We can see that if we analyse the for the same A-site radius $\langle r_A \rangle$; the variation is greater in doping with Gd^{3+} (LGCMO) with the smallest cation radii (1.21 Å), and that the variance is small (0.000691) in doping with Pr^{3+} (1.29), the closest radius to La^{3+} (1.36 Å) in groups.

When we examine the mismatch effect according to the $\langle r_A \rangle$; we observe the most incompatibility in Grp-I ($\langle r_A \rangle = 1.3213$ Å), which we created with the smallest radii. Because we can calculate the A-site radius as 1.3493 Å of $La_{1.4}Ca_{1.6}Mn_2O_7$ phase structure without substituting any cation. Therefore, the mismatch increases in the smallest radius of Grp-I. The maximum variation is observed for the Grp-I LGCMO sample (0.002919) and the minimum one is Grp-III LPCMO with the value of 0.000417.

In the perovskite structure, we mentioned that the transfer of an electron between neighbouring Mn^{3+} (t_{2g}^3, eg^1) and Mn^{4+} (t_{2g}^3, eg^0) via the Mn-O-Mn path is explained by the double exchange model (DE) and this is related to the spin structure and electronic properties. The mobility of *eg* electrons and crystal structural parameters are strongly dependent on, the mixed-valence state of manganese (hole carrier density), externally applied pressure (Moritomo et al. (139), change in oxygen stoichiometry (Guidara et al. (140)), B region cation size and the size mismatch between the A and Ln cations (141). The effect of mismatch becomes a mutual interaction effect with the other lattice parameters and Jahn Teller distortion also. (Dhahri et al. (142). There is a mutual interaction affecting the Mn-O-Mn bond angle and thus the overlap of manganese-oxygen orbitals has been mentioned, also.

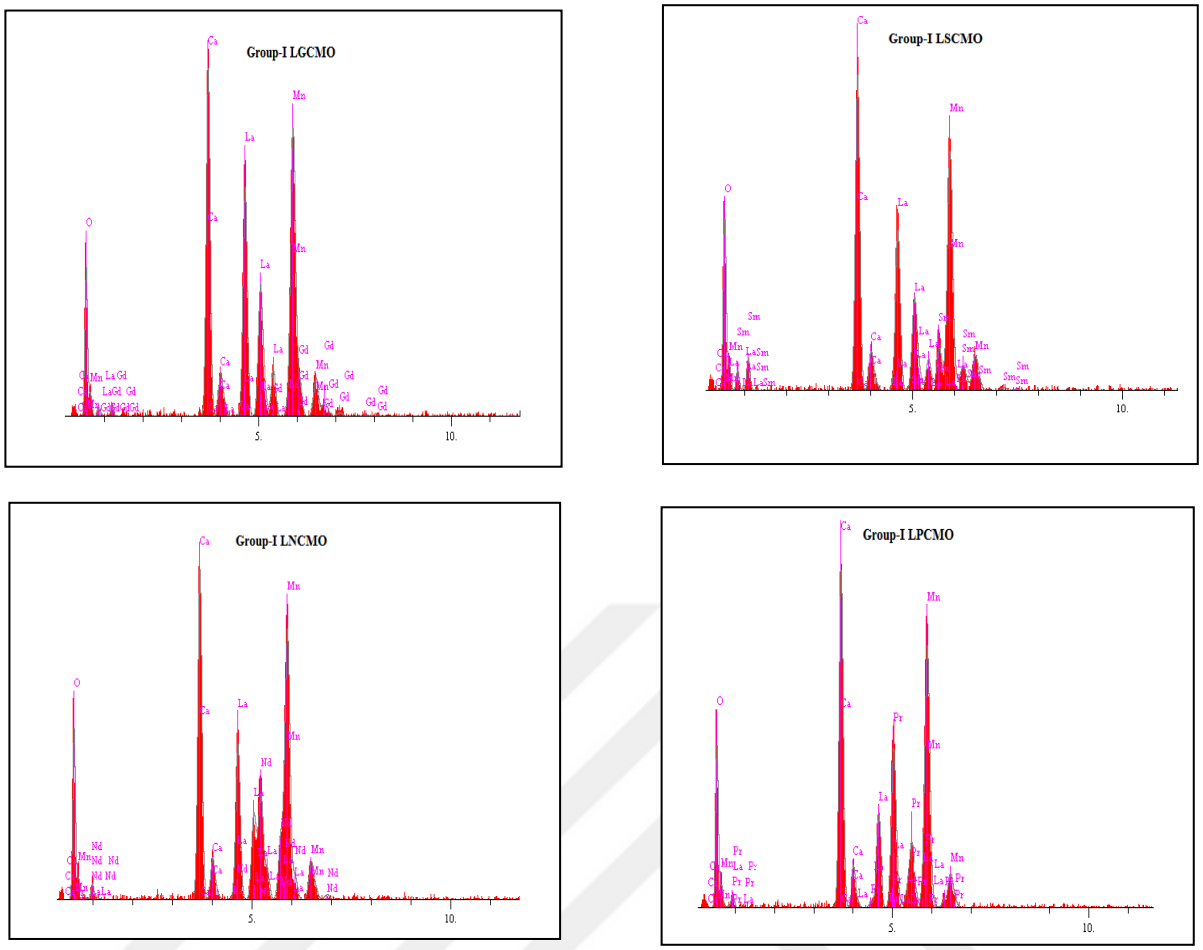

Figure 7. 12. EDX spectrum of the Group- I compounds a) LGCMO b) LSCMO c) LNCMO d) LPCMO

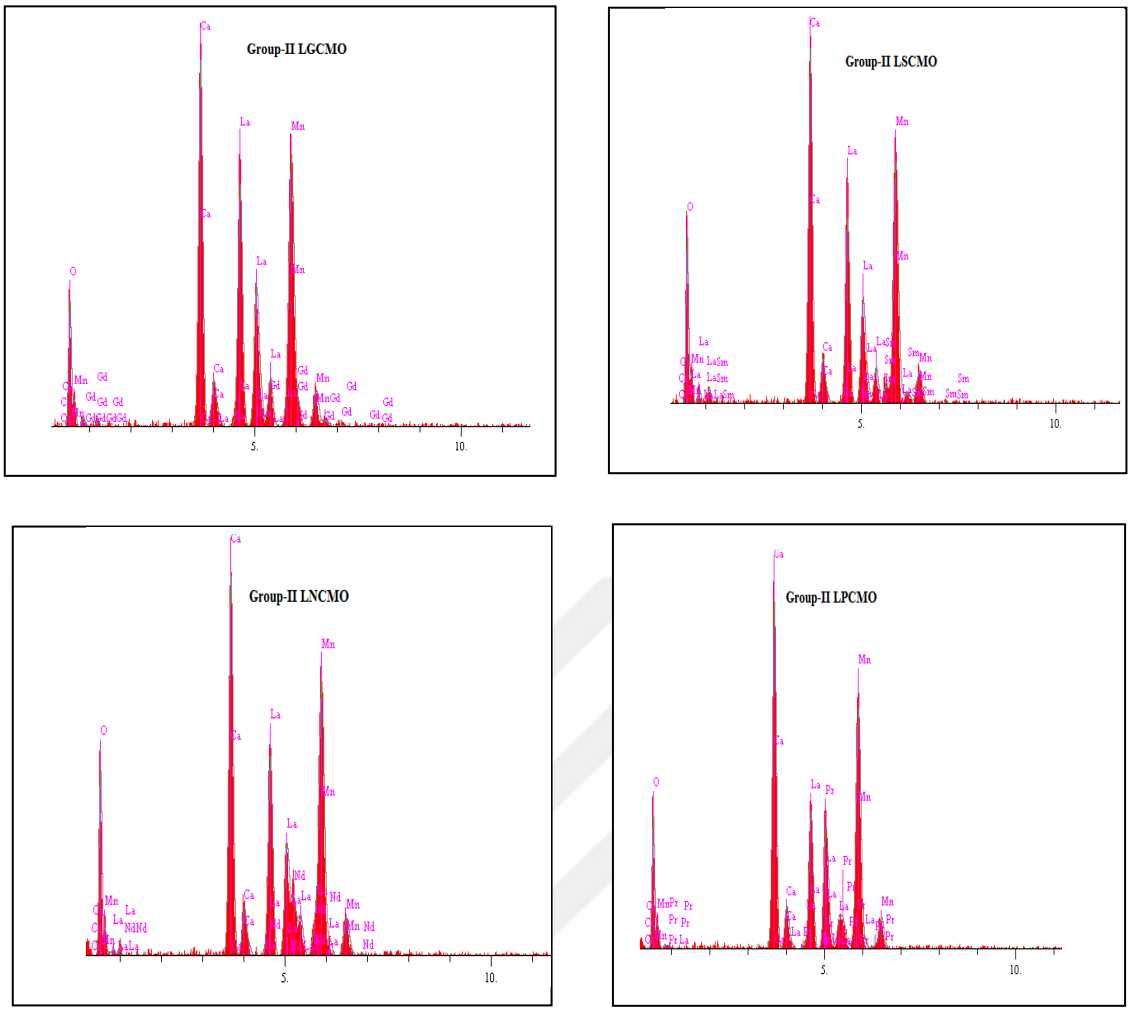

Figure 7. 13. EDX spectrum of the Group- II compounds a) LGCMO b) LSCMO c) LNCMO d) LPCMO

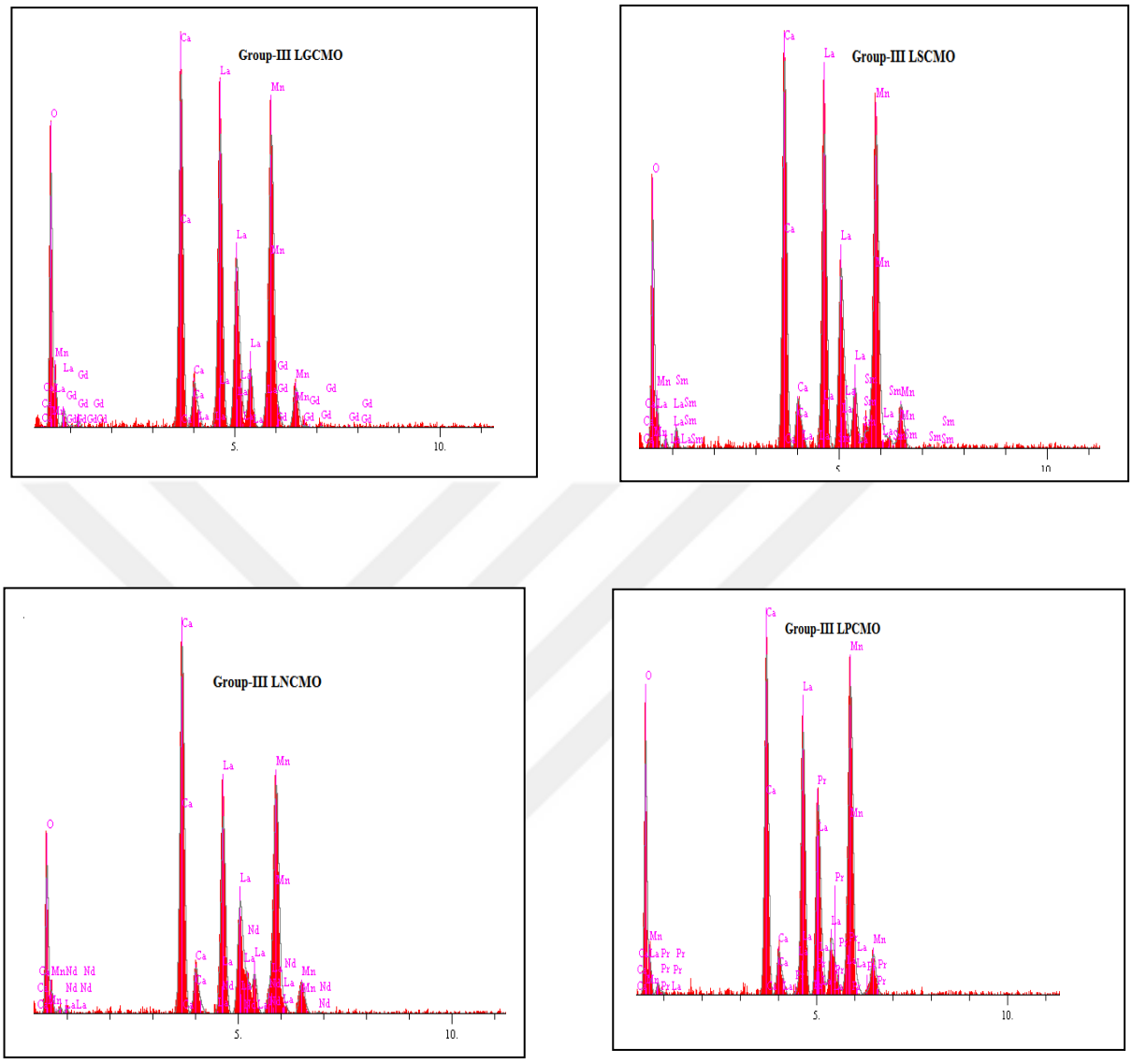

Figure 7. 14. EDX spectrum of the Group- III compounds a) LGCMO b) LSCMO c) LNCMO d) LPCMO

Table 7. 2. Energy-dispersive X-ray analysis (EDX) measurement for samples. (provides the elemental composition (weight %) of synthesized compounds).

a)

Concentration (%) -LGCMO			
Element	**Group-I**	**Group-II**	**Group-III**
O	18.498	17.731	19.609
Ca	13.154	13.314	12.566
Mn	19.253	20.296	17.987
La	40.656	44.655	48.087
Gd	8.438	4.004	1.751
	100.000	100.000	100.000

b)

Concentration (%) -LSCMO			
Element	**Group-I**	**Group-II**	**Group-III**
O	22.614	22.692	20.222
Ca	12.348	13.899	12.832
Mn	18.650	19.318	18.939
La	32.456	38.360	44.747
Sm	13.932	5.731	3.259
	100.000	100.000	100.000

c)

Concentration (%) -LNCMO			
Element	**Group-I**	**Group-II**	**Group-III**
O	18.675	21.545	23.009
Ca	11.515	12.999	11.769
Mn	18.743	18.658	18.710
La	27.731	35.809	41.773
Nd	23.337	10.989	4.739
	100.000	100.000	100.000

d)

Concentration (%) -LPCMO			
Element	**Group-I**	**Group-II**	**Group-III**
O	20.774	20.467	22.968
Ca	13.136	14.986	10.030
Mn	19.312	20.161	17.960
La	19.332	31.700	41.177
Pr	27.447	12.686	7.865
	100.000	100.000	100.000

7.4 Magneto-Transport Characterizations

7.4.1 Metallic –Insulator (MI) Transition

In this section firstly we present and analyze the experimental curves of the resistivity-temperature for all compounds. Fig. 7.15-7.16-7.17 shows the variation for electrical resistivity with a temperature change of double-layered $(La_{1-y}Re_y)_{1.4}Ca_{1.6}Mn_20_7$, between 20K-280K under zero magnetic field. The effect of partial replacements of the La ions with Rare Earths (Gd^{+3}, Sm^{+3}, Nd^{+3}, Pr^{+3}) with a systematic variation of A site radius $\langle r_A \rangle$ while the hole doping level remains constant on electrical transition can be seen from the resistivity data.

It is seen from the graphs all the curves have a metallic character ($d\rho / dT > 0$) at low temperature and a semiconductor character ($d\rho/dT < 0$) at high temperature, as well as a peak, separating these two characters and representing the Metallic – Insulator (MI) Transition at a temperature T_{MI}.

As it can be seen in theTable 7.3; T_{MI} values change in the range of 118-135 K for Group-I, 137-150K for Group-II, 152-179K for Group-III.

As a striking feature, with increasing $\langle r_A \rangle$, the metal-insulator transition temperature (T_{MI}) shift towards higher values and the magnitudes of the resistivity (ρ) at (T_{MI}) decreases. (Fig- 7.18) The maximum T_{MI} transition temperatures are observed in the Grp-III samples, which has the largest $\langle r_A \rangle$. (179.62 K,159.75 K, 158.98 K, 152.97K).

If we inspect the change in the value of T_{MI} according to a group within itself; for the same $\langle r_A \rangle$, we can see the smallest T_{MI} value is observed on LPCMO materials (118.14 K, 137.22 K, 152.97 K), besides, the largest values are observed in LGCMO samples. (135.60 K, 150.51K, 179.62 K). It does not match old studies with perovskites manganites.

Fig- was drawn specifically to examine how the resistivities of samples change depending on the radius. Clearly, we can say that as the A-site radii $\langle r_A \rangle$ increases, the resistivity values at T_{MI} decrease (except LSCMO series). As an example, we can give the maximum resistivity values are shown numerically at T_{MI} temperatures in Fig-7.19. The maximum T_{MI} resistivity values (ρ_{max}) changes as range from 1548.15 Ω.cm to 34,57 Ω.cm, for r_1 and r_3, respectively. This difference in resistivity may be due to the effects of grain boundaries. However, T.J. Zhou et al. (143) have ruled out this possibility because the resistivity due to the grain boundaries follows a function that changes little with temperature.

If we summarize the highest T_{MI} transition temperature in the sample Grp-III LGCMO as 179.62 K; the minimum one is for the Grp-I LPCMO sample as 118.14 K.

The metal-Insulator transition behaviour is explained as a first approximation in the framework of the double exchange theory (DE) (46). As a

first approach, the phonon-electron coupling and Coulomb interactions between electrons have been completely neglected within this theory. In addition, the Jahn-Teller distortion is considered within the same framework of the theory.

By doping on the La-site we vary the average A-site radius and this leads to the weakening of the double ferromagnetic exchange mechanism (FMDE). Reduction in the $\langle r_A \rangle$causes the increased distortion of the Mn_2O_6 octahedron and accordingly the optimal Mn^{3+}–O–Mn^{4+} bond angle. The rate of e_g electron hopping in Mn^{3+} and Mn^{4+} decreases as the weakening of electron's transition ability because of the narrowing of effective bandwidth and causing the growth of resistivity. Eventually, it results in a decrease of double exchange between Mn^{3+}–O–Mn^{4+}. This may be behind this difference in resistivity value observed, also. It is further explained that $\langle r_A \rangle$ the reduction is not conducive to the electrical transport behaviour, T_{MI} shifting to lower temperatures, at the same time, resistivity ρ increases constantly.

G. Venkataiah et al. (144) reported that there is a relationship between $\langle r_A \rangle$ and one electron bandwidth of e_g electrons (W) which depends on the Mn-O-Mn bond angle and it can be understood in the formula as $Wa\frac{cos^{\frac{1}{2}}[\pi-<\theta>]}{d_{Mn-O}}$ where $<\theta>$ is the average Mn-O-Mn bond angle and d is the average Mn-O bond length.

The cation size mismatch effect that is we mentioned above; is a crucial parameter for Metal-Insulator transition. As $\langle r_A \rangle$ increases, σ^2 decreases and deterioration improve, and T_{MI} temperatures, greatly affected by this effect, begin to form at higher temperatures as shown in table 7.4.

Contrary to this situation, when we examine the series with the same radius, we can see that the effect of the mismatch is adversely affected, which disagrees with earlier studies (145,146). A similar result was found in studies with rare earth Cobaltite's (147). A qualitative model has been proposed to explain the linear relationship between T_{MI} and σ^2 (145,146). This model says that there should be an optimal hole contribution and $\sigma^2_{critical}$ value that can be calculated with these values.

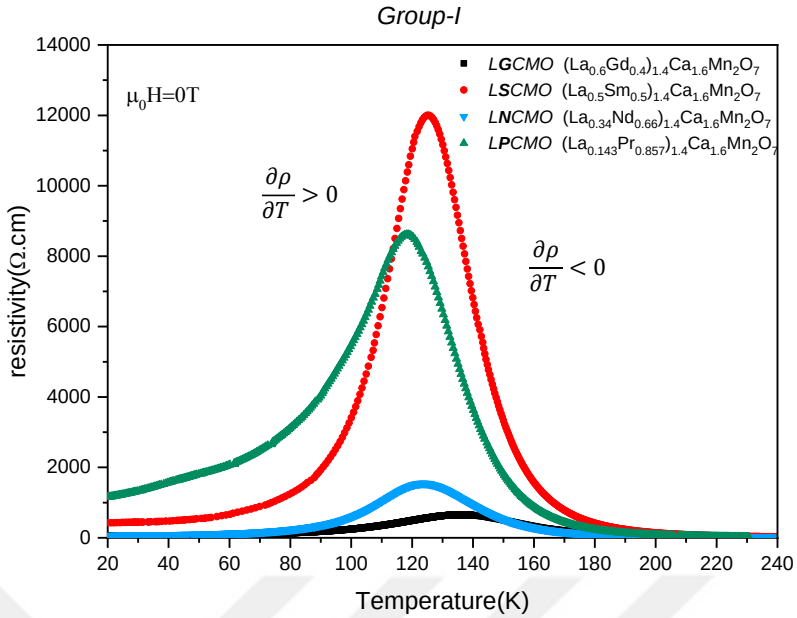

Figure 7. 15. Resistivity as a function of the Temperature of the Group-I compounds without application of the external magnetic field.

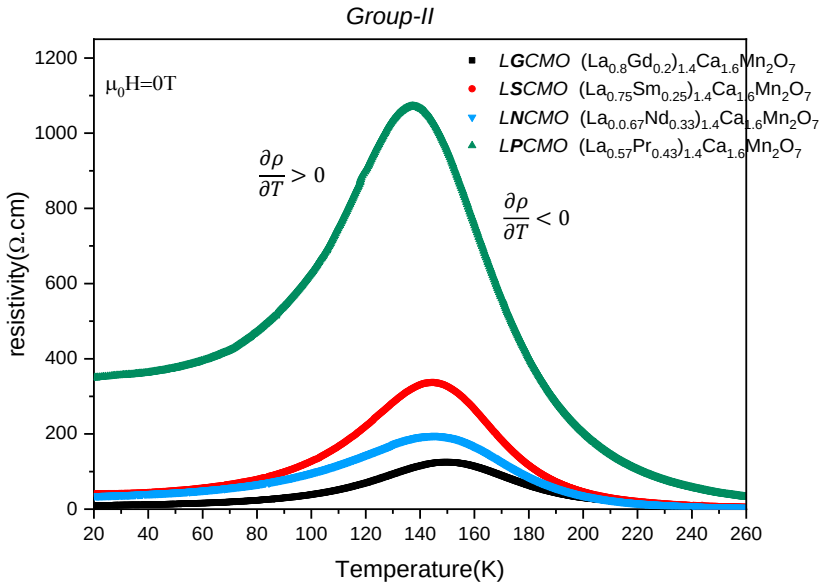

Figure 7. 16. Resistivity as a function of the Temperature of the Group-II compounds without application of the external magnetic field.

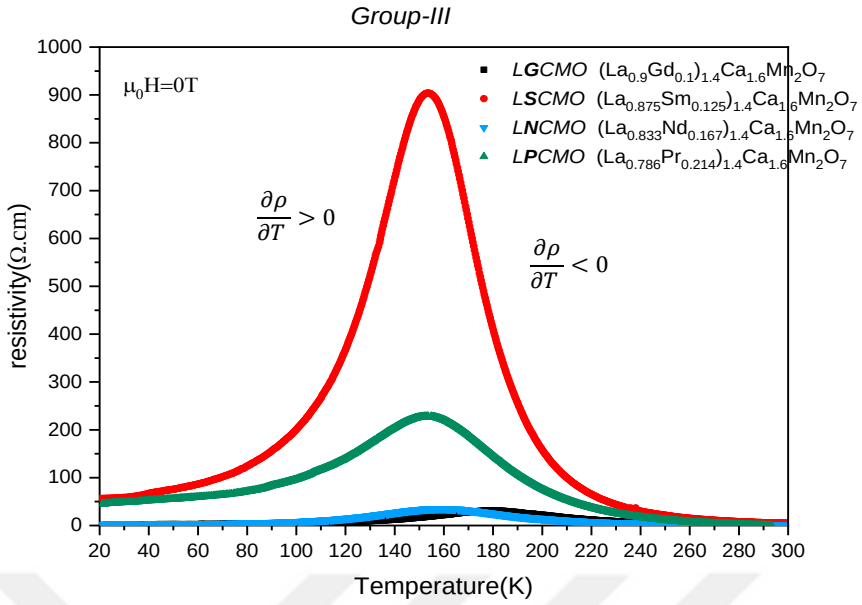

Figure 7. 17. Resistivity as a function of the Temperature of the Group-III compounds without application of the external magnetic field.

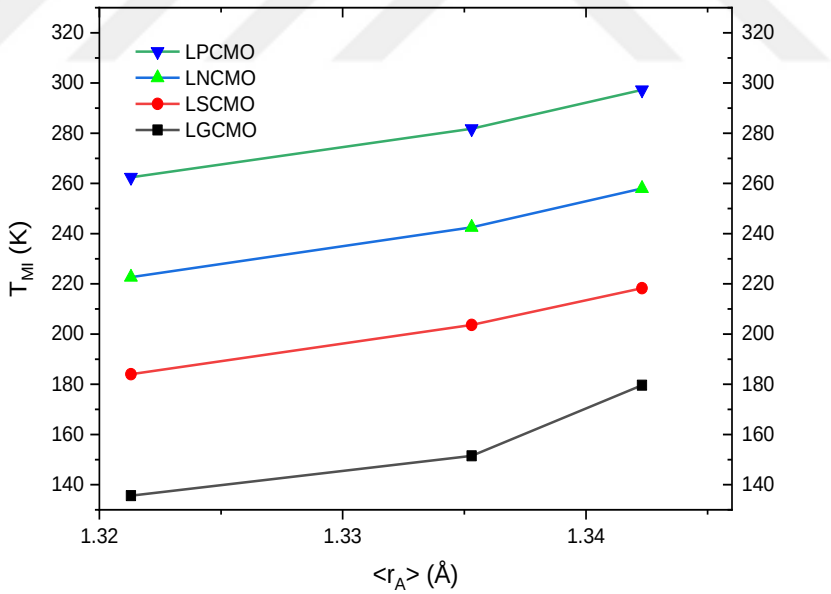

Figure 7. 18. Metal–insulator transition temperature (T_{MI}) dependence of A-site average cationic radius $\langle r_A \rangle$, for all Rare Earth substitution compounds (LGCMO, LSCMO, LNCMO, LPCMO).

7.4.2 Magnetoresistance Effect (MR%)

Figures 7.20-7.31 all show the effect of the external magnetic field on the resistivity of all compounds in the same temperature range: 20-300K. The samples were immersed in a medium where a magnetic field was applied at constant values at 0.4T for each compound. A common effect between all the compounds has been found: a considerable decrease in the resistivity as a function of the applied magnetic field. This decrease is accompanied by a slight increase in T_{MI}. The curves in the Figures show that all the samples have a large magnetoresistance spread over a wide range of low temperatures. They have a similar trend of variation; at a high temperature, they have a very low magnetoresistance, in contrast to the low temperatures. Between these two regions, we note the presence of a positive magnetoresistance peak for each curve.

This classic behaviour is likely to be observed because after applying the magnetic field, the spin of the ions in the environment became parallel and disciplined, thereby increasing the probability that electrons jump from Mn^{3+} to Mn^{4+}; therefore, the electrical resistance of the sample is reduced.

The Figures show the magnetoresistance curves of all the samples under 0.4T values of the magnetic field. It is calculated from the equation;

$$MR\ (\%) = \frac{\rho(0T)-\rho(0.4T)}{\rho(0T)}\ .100 \qquad (7.3)$$

The T_{MI} values and maximum MR values obtained for all samples under 0T and 0.4T field, are summarized in Table 7.3. and also are shown on between the figures 6.20-6.31.

The LPCMO-I shows maximum positive magnetoresistance over a wide temperature range (15-250K) with a maximum value of %55.09 % at 73.8 K under 0.4Tesla. Also, we can say for the samples in Group-I that they show high magnetoresistance values. (Except LGCMO-I). However, it is more pronounced at low temperatures. Also, most of the samples show high magnetoresistance values in a wide temperature range.

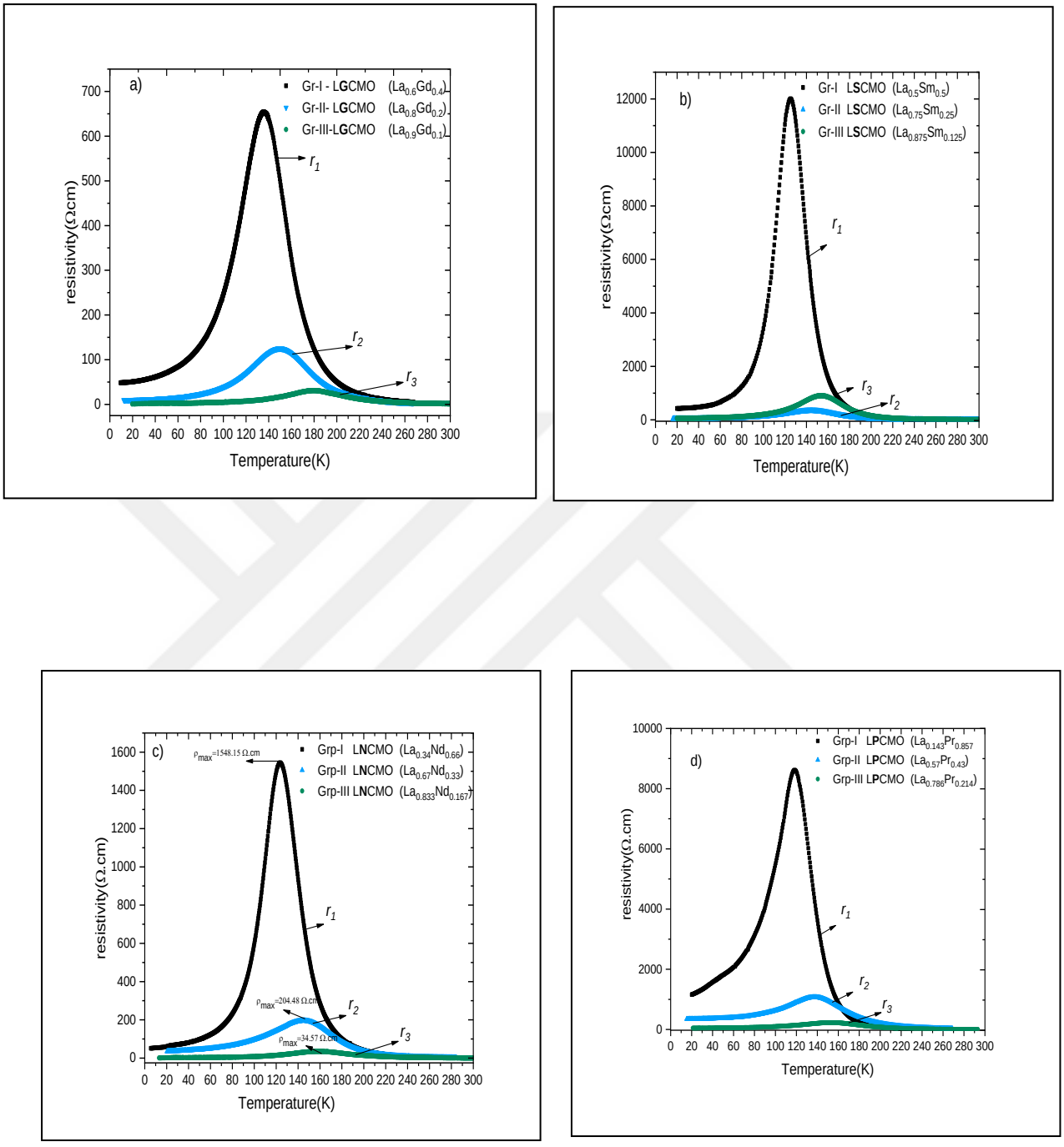

Figure 7. 19. Temperature versus resistivity is dependent on the $\langle r_A \rangle$ for a) LGCMO; b) LSCMO; c) LNCMO; d) LPCMO

Unlike the other compounds, Gr-II LPCMO shows also a negative magnetoresistance in addition to the first positive magnetoresistance (37.68 % at 82.7K). It shows negative magneto-resistance in a wide temperature range from 169 K to 223 K with a maximum value of -7%. This different behaviour can be caused by the strong growth of the fraction of the metallic ferromagnetic domain. This makes this compound more sensitive to the external magnetic field when compared with the other compounds. This phenomenon has already been observed, and it has been attributed to a transport dominated by magnetic polarons which have been formed by self-trapping of charge carriers accompanied by local deformation of the crystal lattice.

It is more pronounced for Group-I LPCMO compound. At the same time, the T_{MI} temperature shifted to high temperatures by a value of 3-4 K for each sample. This can be equivalent to a delocalization of the charge carriers under the action of the magnetic field by causing a local order of the spins. Thus, the conductive ferromagnetic regime reduces the insulating paramagnetic regime under the influence of the magnetic field.

By examining the twelve figures 7.20-7.31, all the peaks took place at temperatures slightly below $T_{MI.}$ This result led us to adopt the qualitative model of Asano et al. (96). This model was first proposed for the compound $La_{1.4}Ca_{1.6}Mn_2O_7$. We then believe that the peak of magnetoresistance is around T_{C1}, just below T_{MI} and that T_{C2} is at high temperature, much further from T_{MI}. In this temperature range, a two-dimensional spin fluctuation is established in the direction c while preserving the ferromagnetic character between the layers and in the a-b planes. Thus a weak external magnetic field can easily restore the order of the spins and consequently improves the transfer of the conduction electrons. This gives considerable magnetoresistance under a relatively weak magnetic field, which is explained by the significant decrease in the resistivity curves under 0.4 Tesla.

This behaviour, which corresponds to large MR at low temperature and weak MR at high temperature, has been widely found for manganites of double perovskites. A similar pattern of MR was found for the compound $La_{2-2x}Ca_{1+}$

$_{2x}Mn_2O_7$ (x = 0.25) (17) where the MR reached 64% at 77K under a magnetic field of 1.8 T . Moritomo et al. (148) have found with the studies of (La, Sr) $_3Mn_2O_7$ show a large MR range accompanying the PI-FM transition. In this layered manganite, the MnO_2 sheets are isolated by two (La, Sr)O planes, keeping the two-dimensional networks of the MnO_6 octahedra.

The origin of MR in manganites comes back to several factors: the tunnel effect of polarized spin across grain boundaries (100), the tunnel effect of charge carriers (at polarized spin) through insulating layers A_2O_2 between the MnO_2 double layers (115), the presence of cavities and grain boundaries (149). At low temperature, one of the main mechanisms is that based on magnetic domains (a magnetism-domain-based mechanism) (150) is coupled, either with the diffusion of spins at the grain boundaries (46) or with the effect inter-granular tunnel of polarized spins(100). The boundaries of the magnetic domains are sites that largely depend on the diffusion of spins. Kerr microscopy (which describes the change in the reflection of light on magnetic surfaces) revealed that the magnetic domains in polycrystalline compounds are defined by grains and generally change direction independently in a magnetic field. The magnetoresistance due to this change reaches 20% and takes place in relatively weak fields (<2000Oe) (101). Beyond a certain value of the magnetic field H> $H_{sa}t$ (H_{sat} is the saturation field), we believe that it is the tunnel effect through the insulating layers $(La,Ca)_2O_2$ which ensure the transfer of the carriers of charges between the double layers (MnO_2, as proposed by T. Kimora et al. (115).

At high temperatures, i.e. at T> T_{C2}, the spin order disappears completely and causes a sudden decrease in MR. This result is observed in all our compounds when T <200K and it is in perfect agreement with that found by K. Wang et al. (149).

Table 7. 3. Metal-Insulator Transition Temperature (T_{MI}) and differences (ΔT_{MI}) between them when 0T and 0.4T magnetic field is applied in Kelvin; and max. magnetoresistance (MR% max) obtained under 0.4T magnetic field and MR around T_{MI} (MR% at T_{MI}) as a percentage for all the compounds.

	Sample	T_{MI} (K)	T_{MI}(K)at 0.4T	ΔT_{MI} (K)	MR% max/ at T (K)	MR% at T_{MI}
Group-I	**LGCMO**	135.60	138.54	2.94	26.66/19.9	17.82
	LSCMO	125.51	128.64	3.13	49.91/29.1	30.38
	LNCMO	124.25	127.34	4.7	37.30/105.95	30.43
	LPCMO	118.68	123.33	4.65	55.09/73.8	45.19
Group-II	**LGCMO**	150.51	153.55	3.04	24.52/29.8	14.72
	LSCMO	145.13	147.53	2.4	27.19/25.5	15.92
	LNCMO	143.52	146.85	3.33	23.85/38.4	14.49
	LPCMO	137.22	145.83	8.61	37.68/82.7	26.88
Group-III	**LGCMO**	179.62	182.19	2.57	24.38/70.30	17.76
	LSCMO	159.75	161.70	1.95	29.25/34.10	18.12
	LNCMO	158.98	160.15	1.17	29.79/4.52	16.11
	LPCMO	152.97	155.15	2.18	28.51/67.7	21.88

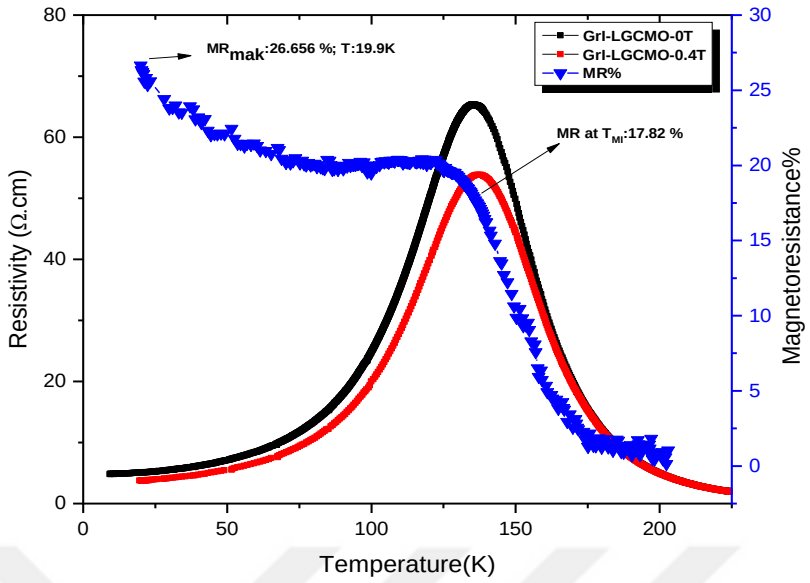

Figure 7. 20 . Resistivity curves and the calculated MR% of the Grp-I LGCMO $((La_{0.6}Gd_{0.4})_{1.4}Ca_{1.6}Mn_2O_7)$ compound under 0T and 0.4 T magnetic field.

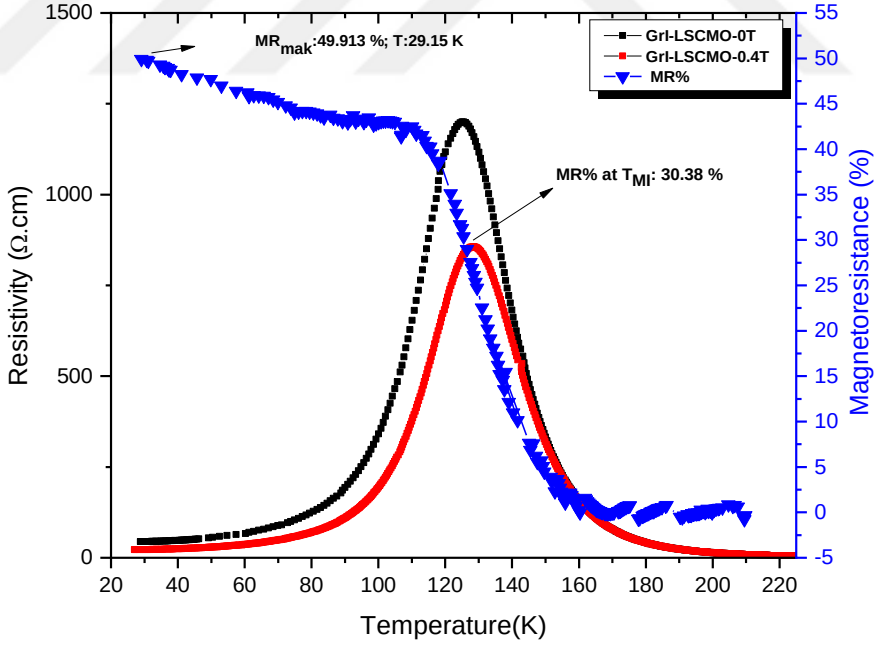

Figure 7. 21. Resistivity curves and the calculated MR% of the Grp-I LSCMO $((La_{0.5}Sm_{0.5})_{1.4}Ca_{1.6}Mn_2O_7)$ compound under 0 T and 0.4 T magnetic field.

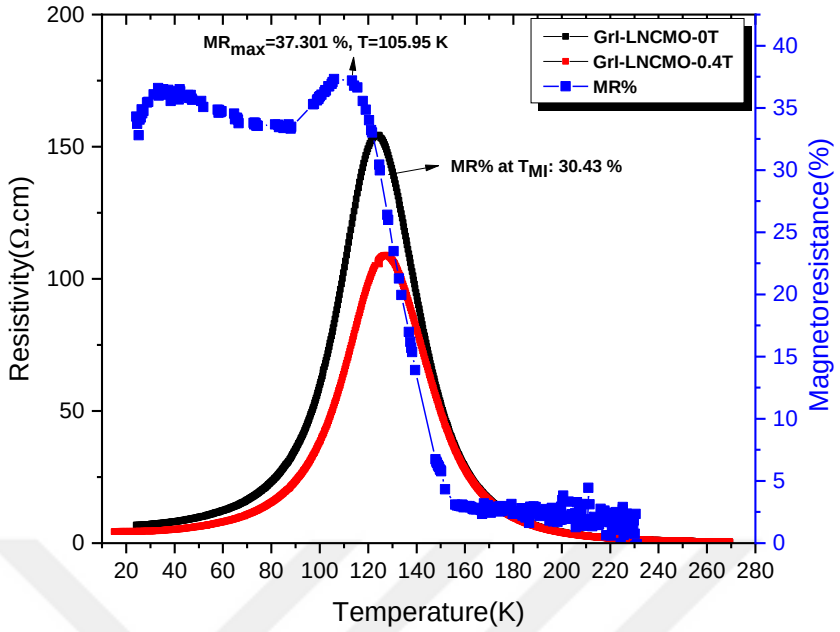

Figure 7. 22. Resistivity curves and the calculated MR% of the Grp-I LNCMO $((La_{0.34}Nd_{0.66})_{1.4}Ca_{1.6}Mn_2O_7)$ compound under 0 T and 0.4 T magnetic field.

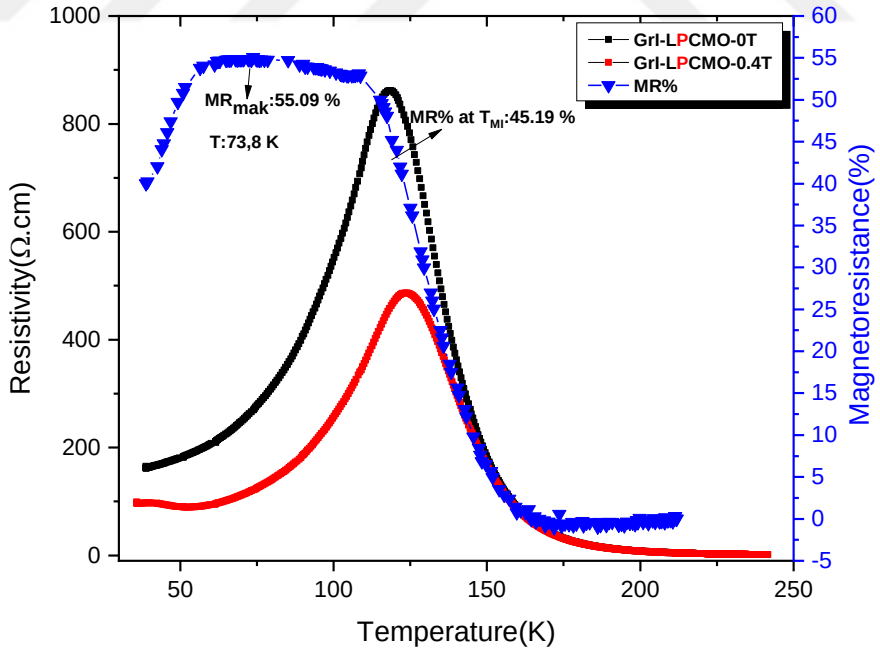

Figure 7. 23. Resistivity curves and the calculated MR% of the Grp-I LPCMO $((La_{0.143}Pr_{0.857})_{1.4}Ca_{1.6}Mn_2O_7)$ compound under 0 T and 0.4 T magnetic field.

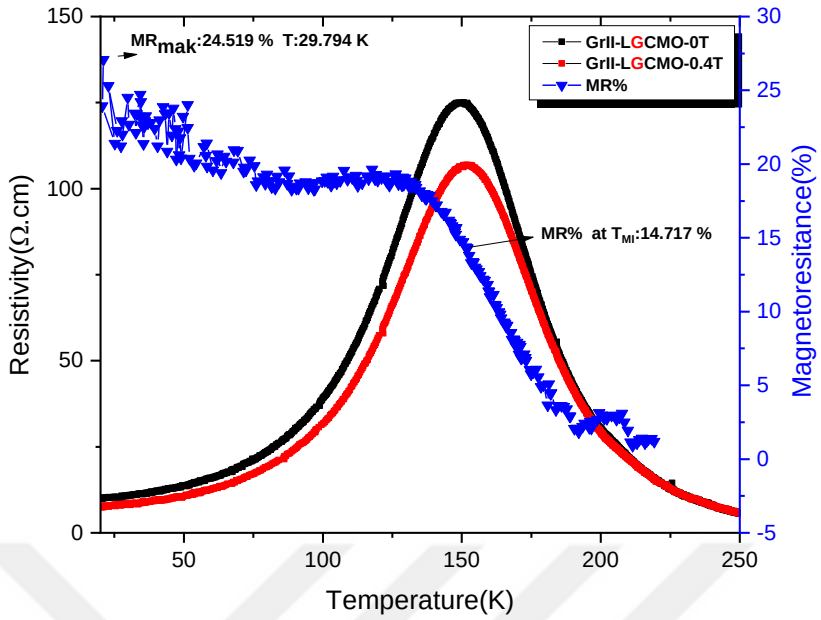

Figure 7. 24. Resistivity curves and the calculated MR % of the Grp-II LGCMO $((La_{0.8}Gd_{0.2})_{1.4}Ca_{1.6}Mn_2O_7)$ compound under 0 T and 0.4 T magnetic field.

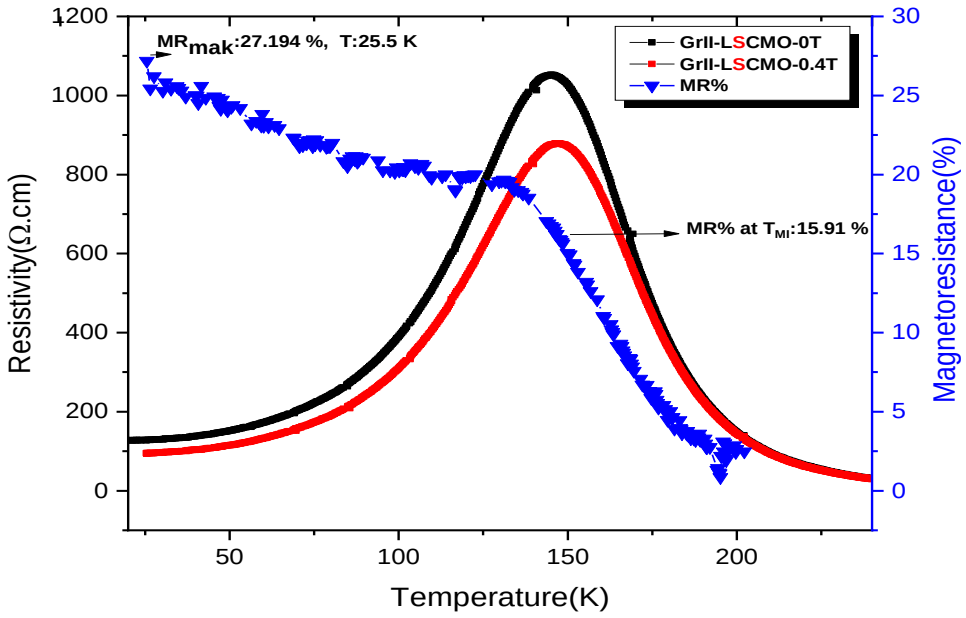

Figure 7. 25. Resistivity curves and the calculated MR% of the Grp-II LSCMO $((La_{0.75}Sm_{0.25})_{1.4}Ca_{1.6}Mn_2O_7)$ compound under 0 T and 0.4 T magnetic field.

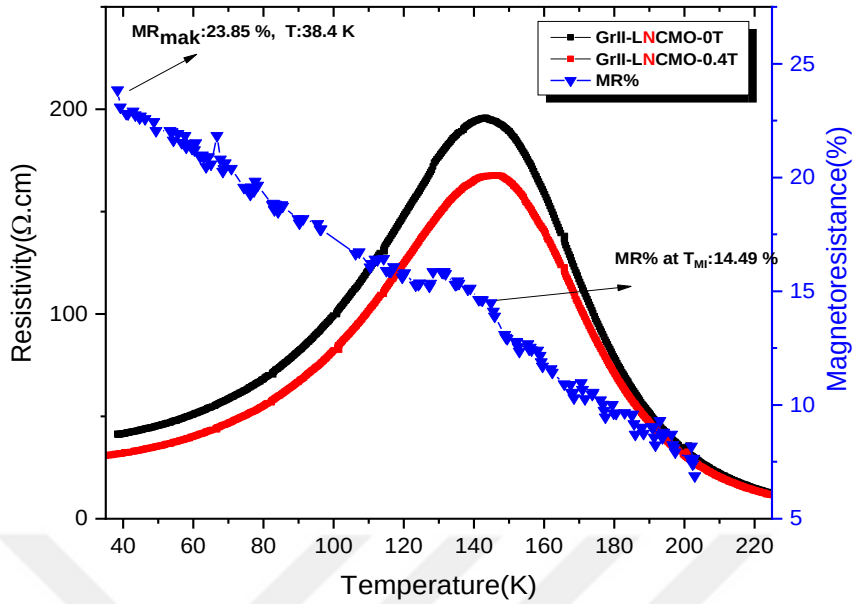

Figure 7. 26. Resistivity curves and the calculated MR% of the Grp-II LNCMO $((La_{0.67}Nd_{0.33})_{1.4}Ca_{1.6}Mn_2O_7)$ compound under 0 T and 0.4 T magnetic field.

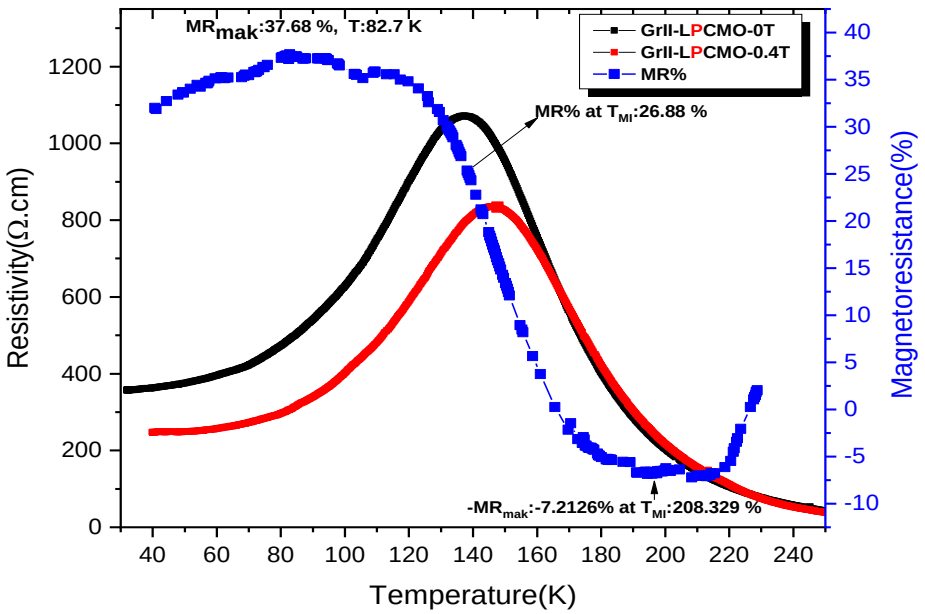

Figure 7. 27. Resistivity curves and the calculated MR% of the Grp-II LPCMO $((La_{0.57}Pr_{0.43})_{1.4}Ca_{1.6}Mn_2O_7)$ compound under 0 T and 0.4 T magnetic field.

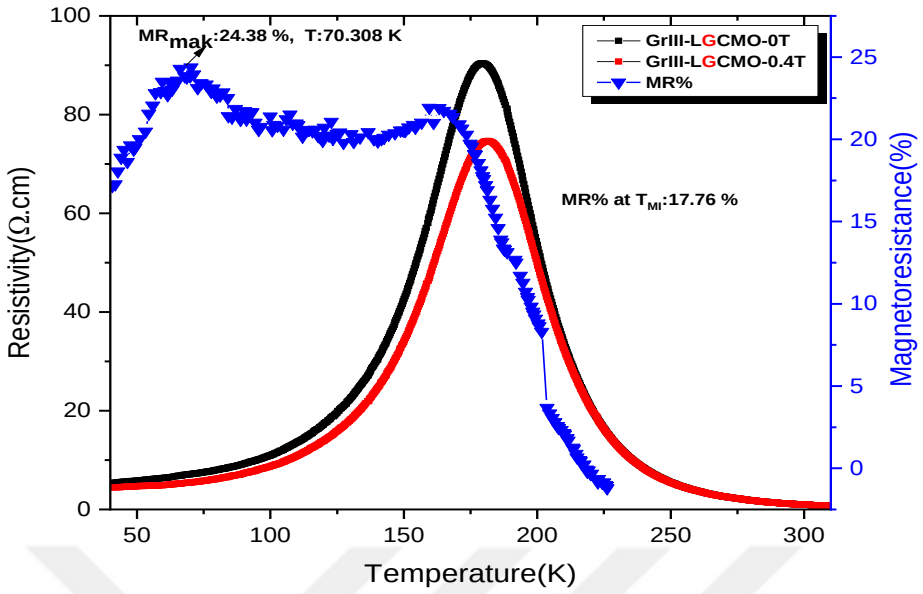

Figure 7. 28. Resistivity curves and the calculated MR % of the Grp-III LGCMO ($(La_{0.9}Gd_{0.1})_{1.4}Ca_{1.6}Mn_2O_7$) compound under 0 T and 0.4 T magnetic field.

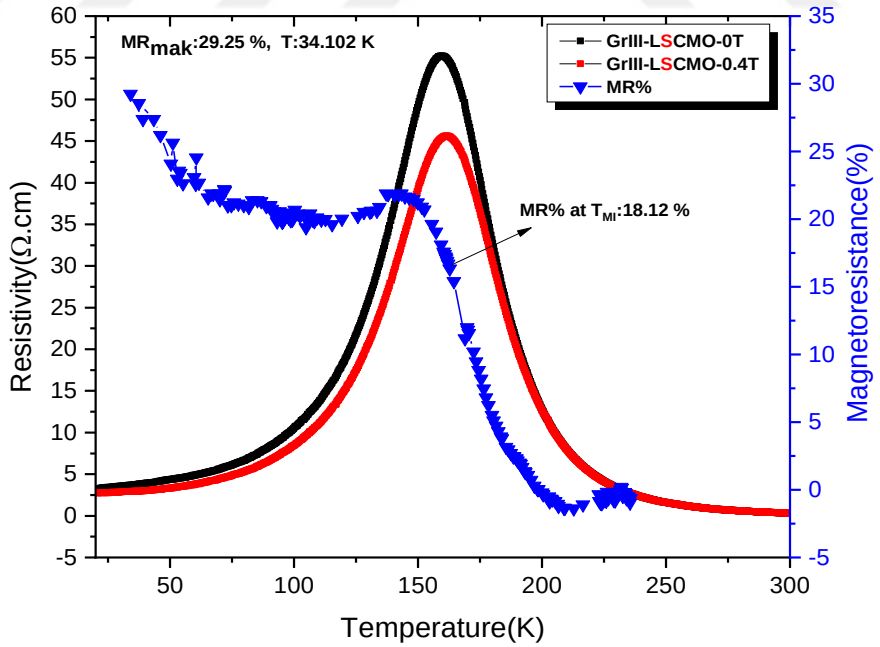

Figure 7. 29. Resistivity curves and the calculated MR % of the Grp-III LSCMO ($(La_{0.875}Sm_{0.125})_{1.4}Ca_{1.6}Mn_2O_7$) compound under 0 T and 0.4 T magnetic field.

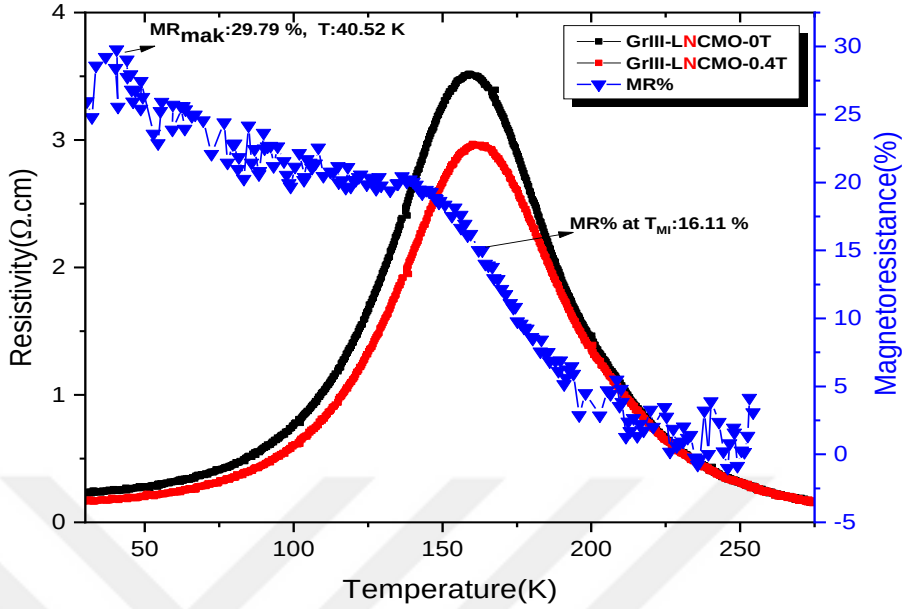

Figure 7. 30. Resistivity curves and the calculated MR % of the Grp-III LNCMO ($(La_{0.833}Nd_{0.167})_{1.4}Ca_{1.6}Mn_2O_7$) compound under 0 T and 0.4 T magnetic field.

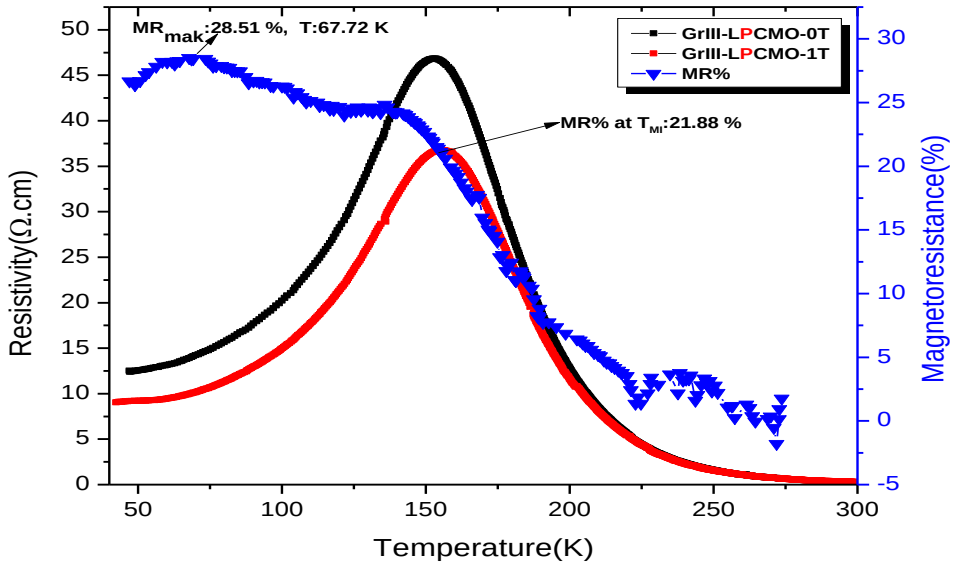

Figure 7. 31. Resistivity curves and the calculated MR % of the Grp-III LPCMO ($(La_{0.786}Pr_{0.214})_{1.4}Ca_{1.6}Mn_2O_7$) compound under 0 T and 0.4 T magnetic field.

7.4.3 Magnetic Transition

AC susceptibility (χ_{AC}) is complementary to measurements in the static (DC) magnetic field and is indispensable especially in phase transitions and magnetic relaxation studies. AC susceptibility is the differential dM/dH response of magnetization of the sample to the oscillating magnetic field (H). Operating frequencies f often varies from 1 Hz to 10 kHz (to compare with static sensitivity).

The A.C magnetic susceptibility, $\chi(T)=\chi'+i\chi''$, measurements were performed for the inquiry of the magnetic phase transition T_C, (paramagnetic - ferromagnetic transitions), measurements were performed under the weak magnetic field of $H_{a.c}$=2Oe at $f_{a.c}$=500 Hz signal frequency over a temperature range of 20–300 K. The only real part of ac-susceptibility (χ') is plotted on the figures. The transition point is defined as the change of orientation of the $d\chi/dT$ curves and is defined as the Critical Temperature, $T_{C.}$ The obtained T_C values are tabulated in Table 6.4. As shown in the graphs; the enlarged insert part is to show an example of the determination of T_C temperature by derivation of susceptibility versus temperature. ($d\chi/dT$ vs T).

As could be seen in the figures all the samples have a typical feature of double-layered ferromagnetic transition as temperature increases magnetization also starts to increase and after reaching a maximum value it shows a sharpness decrease. At low temperatures, the material is in the ferromagnetic phase and is highly ordered, suddenly points reach zero. Otherwise, as the temperature increases, the points of the curves that are dispersed because of the system reaches the paramagnetic phase that is characterized by a disorder of the spins, as is reflected in the susceptibility curves.

The paramagnetic -ferromagnetic phase transition temperatures, $T_{C,}$ is found to lie in the range 128–224 K on three series of samples. As a general observation, it can be said that the magnetic transition temperature (T_c) grows monotonously with increasing $\langle r_A \rangle$. The biggest Tc value of 224 K was measured on the compound Grp-III LPCMO ($\langle r_A \rangle$=1.3423 (Å)).

The relation between the Tc and $\langle r_A \rangle$ should be explained as, with decreasing the average ionic radius of the A-site elements, the distortion of the MnO_6 octahedral structure rises by bending the Mn-O-Mn bond. This causes the reduction of Mn-O-Mn bond angle, increase the Mn-O bond length. Depending on them, Mn^{3+}/Mn^{4+} spins alignment is exposed to distortion, the DE interaction becomes weakening because of the narrowing of the bandwidth by affecting the mobility of e_g electron hopping between Mn sites.

As we mentioned in this explanation, σ^2, which expresses the decay from normal, can be a good quantitative property to explain the changes in Tc. As our obtained Tc values compared to the mismatch effect; as σ^2 decreased, a visible increase in Tc value was also detected. Similar to the results obtained by Martinez et al. (65). The irregularity of the cations triggers the lattice tension, causing random displacement of oxygen ions, resulting in the degradation of the MnO_6 octahedra and thus the localization of the electrons. A major defect of A-site cations is a reason for the random design of Mn^{3+} and Mn^{4+} ions (144). The littlest defect means ($\sigma^2 = 0.00041685$) corresponds to the high magnetic transition temperature (137).

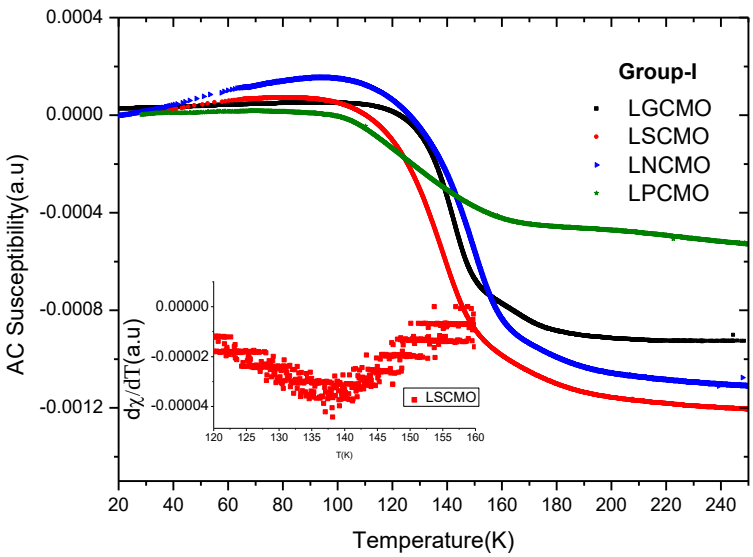

Figure 7. 32. Temperature dependence of real part of A.C susceptibility of Group-I series at $H_{a.c}$=2Oe, $f_{a.c}$=500 Hz. The enlarged derivation graph belongs to Grp-I LSCMO.

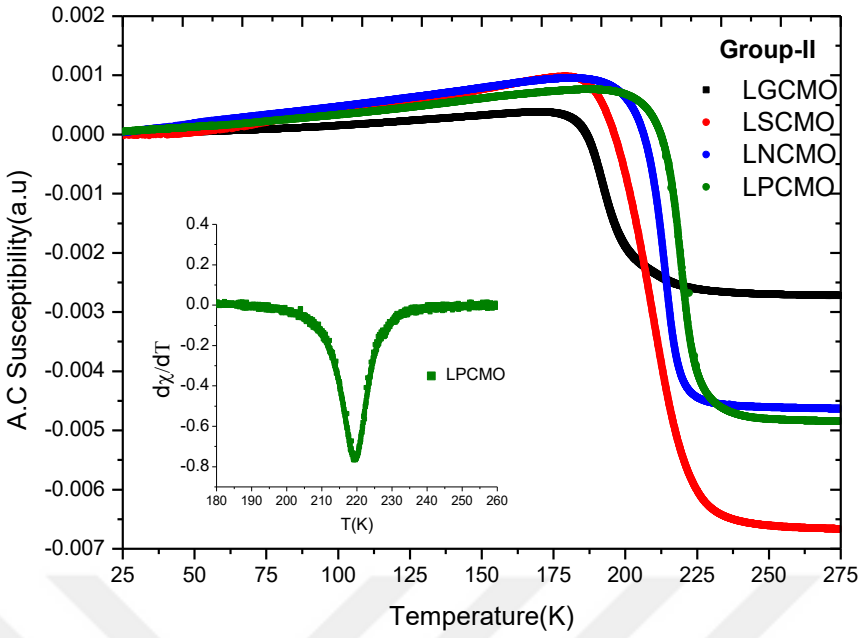

Figure 7. 33. Temperature dependence of real part of A.C susceptibility of Group-II series at Ha.c=2Oe, fa.c=500 Hz. The enlarged derivation graph belongs to Grp-II LPCMO.

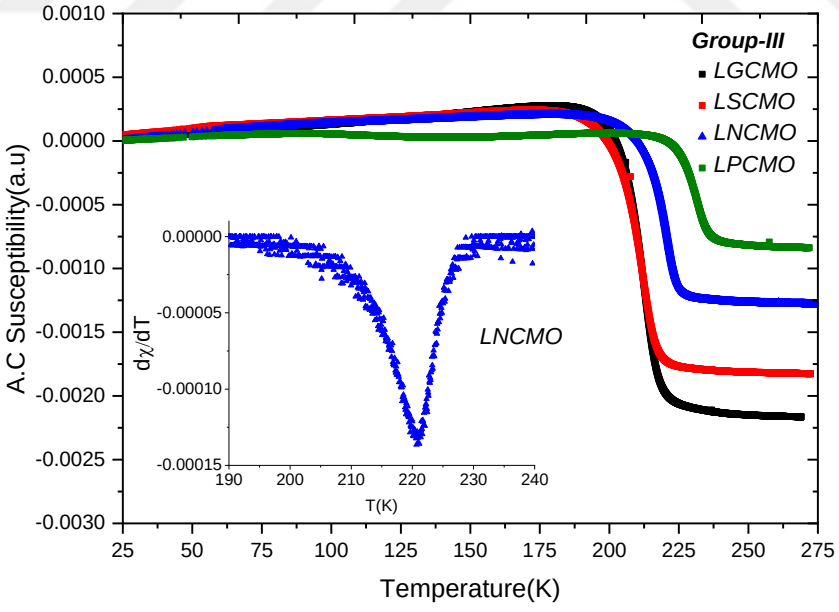

Figure 7. 34. Temperature dependence of real of A.C susceptibility of Group-III series at $H_{a.c}$=2Oe, $f_{a.c}$=500 Hz. The enlarged derivation graph belongs to Grp-III LNCMO.

Table 7. 4. Metal-insulator transition temperatures, T_{MI} (K); Antiferromagnetic to paramagnetic transition temperatures, T_C (K) and A-site variance, $\boldsymbol{\sigma^2}(\text{Å}^2)$.

	Sample	T_{MI} (K)	T_c(K)	$\sigma^2(\text{Å}^2)$
Group-I $\langle r_A \rangle = 1.3213$ (Å)	**LGCMO** $(La_{0.6}Gd_{0.4})_{1.4}Ca_{1.6}Mn_2O_7$	135.60	142	0.002919103
	LSCMO $(La_{0.5}Sm_{0.5})_{1.4}Ca_{1.6}Mn_2O_7$	125.51	138	0.002079103
	LNCMO $(La_{0.34}Nd_{0.66})_{1.4}Ca_{1.6}Mn_2O_7$	124.25	151	0.001975503
	LPCMO $(La_{0.143}Pr_{0.857})_{1.4}Ca_{1.6}Mn_2O_7$	118.68	128	0.000691470
Group-II $\langle r_A \rangle = 1.3353$ (Å)	**LGCMO** $(La_{0.8}\ Gd_{0.2})_{1.4}Ca_{1.6}Mn_2O_7$	150.51	192	0.001704889
	LSCMO $(La_{0.75}Sm_{0.25})_{1.4}Ca_{1.6}Mn_2O_7$	145.13	209	0.001284889
	LNCMO $(La_{0.67}Nd_{0.33})_{1.4}Ca_{1.6}Mn_2O_7$	143.52	214	0.000864889
	LPCMO $(La_{0.57}Pr_{0.43})_{1.4}Ca_{1.6}Mn_2O_7$	137.22	219	0.000584889
Group-III $\langle r_A \rangle = 1.3423$ (Å)	**LGCMO** $(La_{0.9}Gd_{0.1})_{1.4}Ca_{1.6}Mn_2O_7$	179.62	212	0.000952117
	LSCMO $(La_{0.875}Sm_{0.125})_{1.4}Ca_{1.6}Mn_2O_7$	159.75	212	0.000742117
	LNCMO $(La_{0.833}Nd_{0.167})_{1.4}Ca_{1.6}Mn_2O_7$	158.98	220.92	0.000495297
	LPCMO $(La_{0.786}Pr_{0.214})_{1.4}Ca_{1.6}Mn_2O_7$	152.97	224	0.00041685

8. CONCLUSIONS AND RECOMMENDATIONS

In this study, we have explored the chemical pressure on layered manganites by partially substituting the smaller RE elements (RE: Gd^{+3}, Sm^{+3}, Nd^{+3} Pr^{+3}) for the larger La^{3+} ions on the composite of layered $(La_{1-y}RE_y)_{1.4}Ca_{1.6}Mn_20_7$ and we get three different A-site radius ($\langle r_A \rangle$), which is $\langle r_A \rangle \approx$1.3213, 1.3353, 1.3423 (Å). , Three different groups with three different mean radii were formed and each group was formed from 4 different compounds, a total of 12 compounds were formed.

The structural, magneto-electrical properties and their changes under the influence of chemical pressure were investigated in the layered $(La_{1-y}RE_y)_{1.4}Ca_{1.6}Mn_20_7$ manganites.

The smaller RE elements (Gd^{+3}, Sm^{+3} , Nd^{+3} ,Pr^{+3}) (1.21 , 1.23, 1.27 1.29 Å ,respectively) were substituted for the larger La^{+3} (1.36 Å). The considered compound was synthesized by using solid-state reaction methode. The microstructural characterization was analysed by the XRD measurement, Rietveld structural refinements, scanning electron microscopy photograph and the X-ray spectrum elemental analysis (EDX). The electrical transport properties were determined in the temperature range of 5-300 K under a 0.4 T magnetic field. The metal-insulator (M-I) transition temperature (TM-I) and magnetoresistance (MR) values were determined. The A.C susceptibility measurements were performed to obtain the FM- AFM phase transition temperature (Tc). According to these analyses.

1. It is found that the system has a tetragonal perovskite structure with a quadratic space group *I4/mmm.*
2. The metal-insulator transition temperature (T_{MI}) shift towards higher values and the magnitudes of the resistivity (ρ) at (T_{MI}) decreases with increasing $\langle r_A \rangle$. The maximum T_{MI} transition temperatures are observed in the Grp-III samples, which has the largest $\langle r_A \rangle$.(179.62 K,159.75 K, 158.98 K, 152.97K).
3. It can be seen for the same $\langle r_A \rangle$; the smallest T_{MI} value is observed on Pr substituted LPCMO samples (118.14 K, 137.22 K, 152.97 K), besides, the largest values are observed in Gd substituted LGCMO samples. (135.60 K,

150.51K, 179.62 K). It does not match old studies with perovskites manganites.

4. As $\langle r_A \rangle$ increases, σ^2 decreases and deterioration weakens, and T_{MI} temperatures, greatly affected by this effect, begin to form at higher temperatures.
5. The LPCMO-I shows maximum positive magnetoresistance over a wide temperature range (15-250K) with a maximum value of %55.09 % at 73.8 K under 0.4Tesla. Also, we can say for the samples in Group-I that they show high magnetoresistance values. (Except LGCMO-I).
6. The magnetic transition temperature (T_c) grows monotonously with increasing $\langle r_A \rangle$. The biggest T*c* value of 224 K was measured on the compound Grp-III LPCMO ($\langle r_A \rangle$ =1.3423 (Å)).
7. As σ^2 decreased, a visible increase in Tc value was detected. The irregularity of the cations triggers the lattice tension, causing random displacement of oxygen ions, resulting in the degradation of the MnO_6 octahedra and thus the localization of the electrons. A major defect of A-site cations is a reason for the random design of Mn^{3+} and Mn^{4+} ions. The littlest defect means (σ^2= 0.00041685) corresponds to the high magnetic transition temperature.

It can be said that small changes in the size and concentration of ions in the region (R, A) can have a significant impact on transport and magnetic properties. An important factor in promoting electronic transmission, which is very sensitive to the bond lengths and bond angles of Mn-O–Mn caused by the change in the size of lanthanide ions, is the overlap between Mn 3d orbital and O 2p. This chemical pressure has two important consequences; first, it affects magnetic ground states by changing the effective transfer integral of DE and the other one affects the magnetotransport properties by altering the strength of the carrier localization effect (133). Also, the Mn -O- Mn bond angle is about 180 ° in the (La, A) $_3Mn_2O_7$ system and about 155 ° to 170 ° in the (La, A)MnO_3 system(151,152). The bond length can be changed by internal pressure, that is, by changing the size and/or concentration of ground ions (R, A), but it should be noted the variation of the bond length of the Mn-O-Mn bond in the Mn_2O_7 system differs from the bond length in the MnO_3 system. Therefore, investigation of lattice effects on magnetotransport properties in

the (R, A)$_3$Mn$_2$O$_7$ system can be useful in understanding the basics of CMR and related properties(133).

9. REFERENCES

"Vancouver citation system was used in this thesis."

1. Hans-Rudolf Wenk AB. Minerals: their constitution and origin. Vol. 42, Choice Reviews Online. 2004. 42-2243-42–2243 p.
2. Jonker GH, Van Santen JH. Ferromagnetic compounds of manganese with perovskite structure. Physica. 1950;16(3):337–49.
3. Apalkov D, Dieny B, Slaughter JM. Magnetoresistive Random Access Memory. Proc IEEE. 2016;104(10):1796–830.
4. Richards PL. Bolometers for infrared and millimeter waves. J Appl Phys [Internet]. 1994;76(1):1–24. Available from: https://doi.org/10.1063/1.357128
5. Li Y, Walko DA, Li Q, Liu Y, Rosenkranz S, Zheng H, et al. Evidence of photo-induced dynamic competition of metallic and insulating phase in a layered manganite. J Phys Condens Matter. 2015 Dec;27(49):495602.
6. Ramesh R. A new spin on spintronics. Nat Mater [Internet]. 2010;9(5):380–1. Available from: https://doi.org/10.1038/nmat2762
7. El Yadari M, Bahmad L, El Kenz A, Benyoussef A. Monte Carlo study of the double perovskite nano Sr2VMoO6. J Alloys Compd [Internet]. 2013;579:86–91. Available from: https://www.sciencedirect.com/science/article/pii/S0925838813002211
8. Abdelmoula N, Dhahri E, Guidara K, Joubert JC. Structural magnetic and electrical properties of La0.6Ba4−xSrxMnO3 perovskite. Phase Transitions [Internet]. 1999 Jul 1;69(2):215–26. Available from: https://doi.org/10.1080/01411599908208020
9. Raju K, Song MS, Lee JY. Crystal structure and magnetic properties of La2−x(Sr0.5Ca0.5)1+xMn2O7 (x=0.6, 0.8 and 1.0) Ruddlesden–Popper manganites. J Magn Magn Mater [Internet]. 2014;358–359:119–22. Available from: https://www.sciencedirect.com/science/article/pii/S0304885314000511
10. Sharma N, Das A, Prajapat CL, Kumar A, Singh MR. Phase separated behavior in yttrium doped CaMnO3. Mater Res Bull [Internet]. 2016;77:284–90. Available from: https://www.sciencedirect.com/science/article/pii/S0025540816300617
11. Adkin JJ, Hayward MA. BaMnO3-x Revisited: A Structural and Magnetic Study. Chem Mater [Internet]. 2007 Feb 1;19(4):755–62. Available from: https://doi.org/10.1021/cm062055r
12. Gupta AK, Bhalla GL, Khare N. Magnetic phase diagram of double-layered La2−2xCa1+2xMn2O7 manganite. J Phys Chem Solids. 2006;67(11):2358–64.
13. Marthinsen A, Grande T, Selbach SM. Microscopic Link between Electron Localization and Chemical Expansion in AMnO3 and ATiO3 Perovskites (A = Ca, Sr, Ba). J Phys Chem C [Internet]. 2020 Jun 18;124(24):12922–32. Available from: https://doi.org/10.1021/acs.jpcc.0c02060
14. Malavasi L, Mozzati MC, Azzoni CB, Chiodelli G, Flor G. Role of oxygen content on the transport and magnetic properties of La1−xCaxMnO3+δ manganites. Solid State Commun [Internet]. 2002;123(8):321–6. Available from: https://www.sciencedirect.com/science/article/pii/S0038109802003769
15. Chatterji T, editor. Colossal Magnetoresistive Manganites [Internet]. Dordrecht: Springer Netherlands; 2004. Available from: http://link.springer.com/10.1007/978-94-015-1244-2
16. MEHMET HAZAR ŞEREN. Chemical Expansion in Manganites. MIDDLE EAST TECHNICAL UNIVERSITY; 2015.
17. Asano H, Hayakawa J, Matsui M. Giant magnetoresistance of a two-dimensional ferromagnet La 2−2 x Ca 1+2 x Mn 2 O 7. Appl Phys Lett [Internet]. 1996 Jun 17;68(25):3638–40. Available from: http://aip.scitation.org/doi/10.1063/1.115755
18. Kimura T, Tokura Y. Layered Magnetic Manganites. Annu Rev Mater Sci [Internet]. 2000 Aug;30(1):451–74. Available from:

http://www.annualreviews.org/doi/10.1146/annurev.matsci.30.1.451

19. Leonowicz ME, Poeppelmeier KR, Longo JM. Structure determination of Ca2MnO4 and Ca2MnO3.5 by X-ray and neutron methods. J Solid State Chem [Internet]. 1985;59(1):71–80. Available from: https://www.sciencedirect.com/science/article/pii/0022459685903524

20. Battle PD, Green MA, Lago J, Millburn JE, Rosseinsky MJ, Vente JF. Crystal and Magnetic Structures of Ca4Mn3O10, an n = 3 Ruddlesden−Popper Compound. Chem Mater [Internet]. 1998 Feb 1;10(2):658–64. Available from: https://doi.org/10.1021/cm970647r

21. Tokura Y, editor. Colossal Magnetoresistive Oxides [Internet]. CRC Press; 2000. Available from: https://www.taylorfrancis.com/books/9781482287493

22. Sagar S. Investigations on the Multiferroic and Thermoelectric properties of Low and Intermediate band width Manganites. Department of Physics, Cochin University of Science & Technolog; 2010.

23. Vasala S, Karppinen M. A2B′B″O6 perovskites: A review. Prog Solid State Chem [Internet]. 2015 May;43(1–2):1–36. Available from: https://linkinghub.elsevier.com/retrieve/pii/S0079678614000338

24. Hossain A, Bandyopadhyay P, Roy S. An overview of double perovskites A2B′B″O6 with small ions at A site: Synthesis, structure and magnetic properties. J Alloys Compd [Internet]. 2018 Apr;740:414–27. Available from: https://linkinghub.elsevier.com/retrieve/pii/S092583881734478X

25. Jonker GH, Van Santen JH. Ferromagnetic compounds of manganese with perovskite structure. Physica [Internet]. 1950 Mar;16(3):337–49. Available from: https://linkinghub.elsevier.com/retrieve/pii/0031891450900334

26. Jonker GH. Semiconducting properties of mixed crystals with perovskite structure. Physica [Internet]. 1954;20(7):1118–22. Available from: https://www.sciencedirect.com/science/article/pii/S0031891454802503

27. Assirey EAR. Perovskite synthesis, properties and their related biochemical and industrial application. Saudi Pharm J [Internet]. 2019 Sep;27(6):817–29. Available from: https://linkinghub.elsevier.com/retrieve/pii/S1319016419300726

28. Ulyanov AN, Yang D-S, Yu S-C. Anomaly of local structure of La0.7Ca0.3−xBaxMnO3 manganites at Curie temperature. J Appl Phys [Internet]. 2003 May 15;93(10):7376–8. Available from: http://aip.scitation.org/doi/10.1063/1.1558654

29. Parida P, Kashikar R, Jena A, Nanda BRK. Universality in the electronic structure of 3d transition metal oxides. J Phys Chem Solids [Internet]. 2018 Dec;123:133–49. Available from: https://linkinghub.elsevier.com/retrieve/pii/S002236971830204X

30. Coey JMD, Viret M, von Molnár S. Mixed-valence manganites. Adv Phys [Internet]. 1999 Mar;48(2):167–293. Available from: http://www.tandfonline.com/doi/abs/10.1080/000187399243455

31. Zhang J, Wang F, Zhang P, Yan Q. Magnetoresistance in layered perovskites La 1.2 − x Nd x Sr 1.8 Mn 2 O 7. Solid State Commun [Internet]. 1999 Jan;109(6):401–5. Available from: https://linkinghub.elsevier.com/retrieve/pii/S0038109898005754

32. Li Z, Guo W, Zhang TT, Song JH, Gao TY, Gu ZB, et al. Epitaxial growth and electronic structure of Ruddlesden–Popper nickelates (Lan+1NinO3n+1, n = 1–5). APL Mater [Internet]. 2020 Sep 1;8(9):91112. Available from: https://doi.org/10.1063/5.0018934

33. Lee D, Lee H. Controlling Oxygen Mobility in Ruddlesden–Popper Oxides. Materials (Basel) [Internet]. 2017 Mar 31;10(4):368. Available from: http://www.mdpi.com/1996-1944/10/4/368

34. Goldschmidt VM. Die Gesetze der Krystallochemie. Naturwissenschaften [Internet]. 1926;14(21):477–85. Available from: https://doi.org/10.1007/BF01507527

35. GOLDSCHMIDT VM. Geochemistry. Soil Sci [Internet]. 1954;78(2). Available from: https://journals.lww.com/soilsci/Fulltext/1954/08000/Geochemistry.19.aspx

36. Mark Levy. Crystal Structure and Defect Properties in Ceramic Materials. Department of Materials Imperial College of Science, Technology and Medicine; 2005.

37. Johnsson M, Lemmens P. Crystallography and Chemistry of Perovskites. In 2005.

38. Johnson DE. Structural, transport, and magnetic properties of A-site substituted perovskite manganites [Internet]. ProQuest Dissertations and Theses. [Ann Arbor]: Northern Illinois University; 2011. Available from: https://www.proquest.com/dissertations-theses/structural-transport-magnetic-properties-site/docview/894737133/se-2?accountid=15310

39. Mitra SBT-D in G, editor. Chapter 10 ABX3, Perovskite-ilmenite structure. In: High-Pressure Geochemistry and Mineral Physics [Internet]. Elsevier; 2004. p. 711–92. Available from: https://www.sciencedirect.com/science/article/pii/S0921319804800127

40. Benedek N, Fennie C. Hybrid improper ferroelectricity: a mechanism for controllable polarization-magnetization coupling. Phys Rev Lett. 2011;106 10:107204.

41. H. A. Jahn and E. Teller. Stability of polyatomic molecules in degenerate electronic states - I—Orbital degeneracy. R Soc. 1937;161(905).

42. Moritomo Y, Ishikawa H, Nakamura A. Interrelation between cluster orbital and spin ordering in bilayer manganites. Phys Rev B [Internet]. 2003 Aug 21;68(6):64417. Available from: https://link.aps.org/doi/10.1103/PhysRevB.68.064417

43. Dho J, Kim WS, Hur NH. Anomalous thermal hysteresis in magnetization and resistivity of La1-xSrxMnO3. Phys Rev Lett [Internet]. 2001 Oct 10;87(18):187201-1-187201–4. Available from: https://link.aps.org/doi/10.1103/PhysRevLett.87.187201

44. Kawano H, Kajimoto R, Kubota M, Yoshizawa H. Canted antiferromagnetism in an insulating lightly dop with x⩽0.17. Phys Rev B - Condens Matter Mater Phys [Internet]. 1996 Feb 1;53(5):2202–5. Available from: https://link.aps.org/doi/10.1103/PhysRevB.53.2202

45. Kawano H, Kajimoto R, Kubota M, Yoshizawa H. Ferromagnetism-induced reentrant structural transition and phase diagram of the lightly doped insulator). Phys Rev B - Condens Matter Mater Phys [Internet]. 1996 Jun 1;53(22):R14709–12. Available from: https://link.aps.org/doi/10.1103/PhysRevB.53.R14709

46. Schiffer P, Ramirez AP, Bao W, Cheong SW. Low temperature magnetoresistance and the magnetic phase diagram of La1-xCaxMnO3. Phys Rev Lett [Internet]. 1995 Oct 30;75(18):3336–9. Available from: https://link.aps.org/doi/10.1103/PhysRevLett.75.3336

47. Siwach PK, Singh HK, Srivastava ON. Low field magnetotransport in manganites. J Phys Condens Matter [Internet]. 2008 Jul 9;20(27):273201. Available from: https://iopscience.iop.org/article/10.1088/0953-8984/20/27/273201

48. Bousquet E, Cano A. Non-collinear magnetism in multiferroic perovskites. J Phys Condens Matter [Internet]. 2016;28(12):123001. Available from: http://dx.doi.org/10.1088/0953-8984/28/12/123001

49. Long MW, Khomskii D, Millis AJ, Venkatesan T, Paul DM. Orbital Ordering and Strong Correlations in Manganites [and Discussion]. Philos Trans Math Phys Eng Sci [Internet]. 1998 Jul 25;356(1742):1493–517. Available from: http://www.jstor.org/stable/54874

50. Goodenough JB. Theory of the role of covalence in the perovskite-type manganites [La,M(II)]MnO3. Phys Rev [Internet]. 1955 Oct 15;100(2):564–73. Available from: https://link.aps.org/doi/10.1103/PhysRev.100.564

51. Kanamori J. Crystal Distortion in Magnetic Compounds. J Appl Phys. 1960;31.

52. Mizokawa T, Khomskii DI, Sawatzky GA. Interplay between orbital ordering and lattice distortions in LaMnO3, YVO3, and YTiO3. Phys Rev B - Condens Matter Mater Phys [Internet]. 1999 Sep 1;60(10):7309–13. Available from: https://link.aps.org/doi/10.1103/PhysRevB.60.7309

53. Dagotto E, Hotta T, Moreo A. Colossal magnetoresistant materials: the key role of phase separation. Phys Rep [Internet]. 2001;344(1):1–153. Available from: https://www.sciencedirect.com/science/article/pii/S0370157300001216

54. X. Xiong, B. Dabrowski, O. Chmaissem, Z. Bukowski, S. Kolesnik, R. Dybzinski, C. W. Kimball and JDJ. No Title. Phys Rev B. 1999;60(10):186.

55. Anderson PW, Hasegawa H. Considerations on Double Exchange. Phys Rev [Internet].

1955 Oct 15;100(2):675–81. Available from: https://link.aps.org/doi/10.1103/PhysRev.100.675

56. Wollan EO, Koehler WC. Neutron diffraction study of the magnetic properties of the series of perovskite-type compounds [(1-x)La,xCa]MnO3. Phys Rev [Internet]. 1955 Oct 15;100(2):545–63. Available from: https://link.aps.org/doi/10.1103/PhysRev.100.545

57. Mathieu R, Uchida M, Kaneko Y, He JP, Yu XZ, Kumai R, et al. Bandwidth-disorder phase diagram of half-doped layered manganites. Phys Rev B [Internet]. 2006 Jul 27;74(2):020404. Available from: https://link.aps.org/doi/10.1103/PhysRevB.74.020404

58. Freeman PG, Boothroyd AT, Prabhakaran D, Frost CD, Enderle M, Hiess A. Spin dynamics of half-doped La3/2 Sr1/2 Ni O4. Phys Rev B - Condens Matter Mater Phys [Internet]. 2005 May 18;71(17):174412. Available from: https://link.aps.org/doi/10.1103/PhysRevB.71.174412

59. van den Brink J, Khomskii D. Double Exchange via Degenerate Orbitals. Phys Rev Lett [Internet]. 1999 Feb 1;82(5):1016–9. Available from: https://link.aps.org/doi/10.1103/PhysRevLett.82.1016

60. Yun SH. EFFECT OF DISORDER IN CUPRATES AND MANGANITES. Florida Uni; 2008.

61. MOTT NF. Metal-Insulator Transition. Rev Mod Phys [Internet]. 1968 Oct 1;40(4):677–83. Available from: https://link.aps.org/doi/10.1103/RevModPhys.40.677

62. Rodriguez-Martinez LM, Attfield JP. Cation disorder and the metal-insulator transition temperature in manganese oxide perovskites. Phys Rev B [Internet]. 1998 Aug 1;58(5):2426–9. Available from: https://link.aps.org/doi/10.1103/PhysRevB.58.2426

63. Rodríguez-Martínez LM, Attfield JP. Disorder-induced orbital ordering in L 0.7 M 0.3 MnO 3 perovskites . Phys Rev B [Internet]. 2000 Dec 20;63(2):024424. Available from: https://link.aps.org/doi/10.1103/PhysRevB.63.024424

64. Huang Y, Liao C-S, Yan C-H. Structural Dependence of Magnetic and Transport Properties in Doped Manganite Perovskites①. Jiegou Huaxue. 2002 Jan 1;21.

65. Rodriguez-Martinez LM, Attfield JP. Cation disorder and size effects in magnetoresistive manganese oxide perovskites. Phys Rev B - Condens Matter Mater Phys [Internet]. 1996 Dec 1;54(22):R15622–5. Available from: https://link.aps.org/doi/10.1103/PhysRevB.54.R15622

66. Zhu L, Zhang M, Zhong W, Leng S, Zhou G, Zou Y, et al. Progress and prospects of the morphology of non-fullerene acceptor based high-efficiency organic solar cells. Energy Environ Sci [Internet]. 2021; Available from: http://xlink.rsc.org/?DOI=D1EE01220G

67. Coronado E, Tsukerblat BS, Georges R. Exchange Interactions I: Mechanisms. In: Molecular Magnetism: From Molecular Assemblies to the Devices [Internet]. Dordrecht: Springer Netherlands; 1996. p. 65–84. Available from: http://link.springer.com/10.1007/978-94-017-2319-0_3

68. Liu J. Lattice, magnetic excitations and their coupling in multiferroic materials. Université Paris 7 – Denis Diderot; 2013.

69. Goodenough J. Goodenough-Kanamori rule. Scholarpedia [Internet]. 2008;3(10):7382. Available from: http://www.scholarpedia.org/article/Goodenough-Kanamori_rule

70. de Gennes P-G. Effects of Double Exchange in Magnetic Crystals. Phys Rev [Internet]. 1960 Apr 1;118(1):141–54. Available from: https://link.aps.org/doi/10.1103/PhysRev.118.141

71. Zener C. Interaction Between the d Shells in the Transition Metals. Phys Rev [Internet]. 1951 Feb 1;81(3):440–4. Available from: https://link.aps.org/doi/10.1103/PhysRev.81.440

72. Uehara M, Mori S, Chen CH, Cheong S-W. Percolative phase separation underlies colossal magnetoresistance in mixed-valent manganites. Nature [Internet]. 1999;399(6736):560–3. Available from: https://doi.org/10.1038/21142

73. Li H. Synthesis of CMR manganites and ordering phenomena in complex transition metal oxides. Schriften des Forschungszentrums Jülich Reihe Schlüsseltechnologien / Key Technologies; 2008.

74. Zener C. Interaction between the d-Shells in the Transition Metals. II. Ferromagnetic Compounds of Manganese with Perovskite Structure. Phys Rev [Internet]. 1951 May 1;82(3):403–5. Available from: https://link.aps.org/doi/10.1103/PhysRev.82.403

75. Prieto MJC. Magnetic and electric properties of systems with colossal magnetoresistance. Université Autonoma de Madrid, Espagne; 2001.

76. Millis AJ, Littlewood PB, Shraiman BI. Double exchange alone does not explain the resistivity of La1-xSrxMnO3. Phys Rev Lett [Internet]. 1995 Jun 19;74(25):5144–7. Available from: https://link.aps.org/doi/10.1103/PhysRevLett.74.5144

77. Millis AJ. Colossal magnetoresistance manganites: a laboratory for electron–phonon physics. Blamire M, Cohen LF, Edwards DM, Macmanus-Driscoll JL, editors. Philos Trans R Soc London Ser A Math Phys Eng Sci [Internet]. 1998 Jul 15;356(1742):1473–80. Available from: https://royalsocietypublishing.org/doi/10.1098/rsta.1998.0230

78. Johnsson M, Lemmens P. Crystallography and Chemistry of Perovskites. In: Handbook of Magnetism and Advanced Magnetic Materials [Internet]. Chichester, UK: John Wiley & Sons, Ltd; 2007. Available from: https://onlinelibrary.wiley.com/doi/10.1002/9780470022184.hmm411

79. Ramakrishnan T V. Modelling colossal magnetoresistance manganites. J Phys Condens Matter [Internet]. 2007 Mar 28;19(12):125211. Available from: https://iopscience.iop.org/article/10.1088/0953-8984/19/12/125211

80. Zhao G, Conder K, Keller H, Müller KA. Isotope and pressure effects in manganites: Important experimental constraints on the physics of manganites. Phys Rev B [Internet]. 1999 Nov 1;60(17):11914–7. Available from: https://link.aps.org/doi/10.1103/PhysRevB.60.11914

81. Fontcuberta J, Martinez B, Laukhin V, Balcells L, Obradors X, Cohenca CH, et al. Bandwidth Control of the Spin Diffusion through Interfaces and the Electron-Phonon Coupling in Magnetoresistive Manganites [and Discussion]. Philos Trans Math Phys Eng Sci [Internet]. 1998 Jul 26;356(1742):1577–91. Available from: http://www.jstor.org/stable/54878

82. Zhao D, Liu F, Huber DL, Lagally MG. Magnetization on rough ferromagnetic surfaces. Phys Rev B [Internet]. 2000 Nov 1;62(17):11316–9. Available from: https://link.aps.org/doi/10.1103/PhysRevB.62.11316

83. Rozenberg E, Shames AI, Auslender M, Jung G, Felner I, Sinha J, et al. Disorder-induced phase coexistence in bulk doped manganites and its suppression in nanometer-sized crystals: The case of La0.9 Ca0.1 Mn O3. Phys Rev B - Condens Matter Mater Phys [Internet]. 2007 Dec 26;76(21):214429. Available from: https://link.aps.org/doi/10.1103/PhysRevB.76.214429

84. Yun S. Effect of Disorder in Cuprates and Manganites. University of Florida; 2008.

85. Cherif K, Dhahri J, Dhahri E, Oumezzine M, Vincent H. Effect of the A Cation Size on the Structural, Magnetic, and Electrical Properties of Perovskites (La1−xNdx)0.7Sr0.3r003nMnO3. J Solid State Chem [Internet]. 2002;163(2):466–71. Available from: https://www.sciencedirect.com/science/article/pii/S0022459601994290

86. S. Zhou, J. Xu, S. Li, W. Yang, J. Zou, G. Zhao, H. Li, Y. Hang, J. R. Cheng and Y. Zhang. No Title. Phys Stat Sol (a), 201, No 5, 990. 2004;201(5):990.

87. López J, de Lima OF, Lisboa-Filho PN, Araujo-Moreira FM. Specific heat at low temperatures and magnetic measurements in (formula presented) and (formula presented) (formula presented) Sm, Dy, and Ho) samples. Phys Rev B - Condens Matter Mater Phys [Internet]. 2002 Dec 4;66(21):1–7. Available from: https://link.aps.org/doi/10.1103/PhysRevB.66.214402

88. Radaelli P, Cox D, Marezio M. Charge, orbital, and magnetic ordering ins. Phys Rev B - Condens Matter Mater Phys [Internet]. 1997 Feb 1;55(5):3015–23. Available from: https://link.aps.org/doi/10.1103/PhysRevB.55.3015

89. Asano H, Hayakawa J, Matsui M. Preparation and properties of triple perovskite La3−3xCa1+3xMn3O10 ferromagnetic thin films. Appl Phys Lett [Internet]. 1997 Aug 11;71(6):844–6. Available from: http://aip.scitation.org/doi/10.1063/1.119664

90. Y Tokura. Colossal magnetoresistive oxides.

91. Raychaudhuri P, Mitra C, Paramekanti A, Pinto R, Nigam AK, Dhar SK. The metal - insulator transition and ferromagnetism in the electron-doped layered manganites (x = 0, 0.3, 0.5). J Phys Condens Matter [Internet]. 1998 Mar 30;10(12):L191–8. Available from: https://iopscience.iop.org/article/10.1088/0953-8984/10/12/002

92. Yuan SL, Li ZY, Zhao WY, Li G, Jiang Y, Zeng XY, et al. Phenomenological model for colossal magnetoresistance in optimally doped manganese perovskites. Phys Rev B [Internet]. 2001 Apr 9;63(17):172415. Available from: https://link.aps.org/doi/10.1103/PhysRevB.63.172415

93. Fontcuberta J, Martínez B, Seffar A, Piñol S, García-Muñoz JL, Obradors X. Colossal Magnetoresistance of Ferromagnetic Manganites: Structural Tuning and Mechanisms. Phys Rev Lett [Internet]. 1996 Feb 12;76(7):1122–5. Available from: https://link.aps.org/doi/10.1103/PhysRevLett.76.1122

94. Thomson W. XIX. On the electro-dynamic qualities of metals:—Effects of magnetization on the electric conductivity of nickel and of iron. Proc R Soc London [Internet]. 1857 Dec 31;8:546–50. Available from: https://royalsocietypublishing.org/doi/10.1098/rspl.1856.0144

95. Venkataiah G, Lakshmi YK, Reddy PV. Thermopower studies of Pr0.67D0.33MnO3manganite system. J Phys D Appl Phys [Internet]. 2007;40(3):721–9. Available from: http://dx.doi.org/10.1088/0022-3727/40/3/005

96. Asano H, Hayakawa J, Matsui M. Magnetotransport in perovskite series ferromagnets. Phys Rev B - Condens Matter Mater Phys [Internet]. 1998 Jan 1;57(2):1052–6. Available from: https://link.aps.org/doi/10.1103/PhysRevB.57.1052

97. Zhang J, Wang F, Zhang P, Yan Q. Effect of Fe doping on magnetic properties and magnetoresistance in La1.2Sr1.8Mn2O7. J Appl Phys [Internet]. 1999 Aug;86(3):1604–6. Available from: http://aip.scitation.org/doi/10.1063/1.370933

98. Damay F, Martin C, Maignan A, Raveau B. Cation disorder and size effects upon magnetic transitions in Ln0.5A0.5MnO3 manganites. J Appl Phys [Internet]. 1997 Dec 15;82(12):6181–5. Available from: http://aip.scitation.org/doi/10.1063/1.366543

99. Attfield JP. A Simple Approach to Lattice Effects in Conducting Perovskite-Type Oxides. Chem Mater [Internet]. 1998 Nov 1;10(11):3239–48. Available from: https://doi.org/10.1021/cm980221s

100. Hwang HY, Cheong SW, Ong NP, Batlogg B. Spin-polarized intergrain tunneling in La2/3Sr1/3MnO3. Phys Rev Lett [Internet]. 1996 Sep 2;77(10):2041–4. Available from: https://link.aps.org/doi/10.1103/PhysRevLett.77.2041

101. Gupta A, Gong GQ, Xiao G, Duncombe PR, Lecoeur P, Trouilloud P, et al. Grain-boundary effects on the magnetoresistance properties of perovskite manganite films. Phys Rev B [Internet]. 1996 Dec 1;54(22):R15629–32. Available from: https://link.aps.org/doi/10.1103/PhysRevB.54.R15629

102. Sheng P, Abeles B, Arie Y. Hopping Conductivity in Granular Metals. Phys Rev Lett [Internet]. 1973 Jul 2;31(1):44–7. Available from: https://link.aps.org/doi/10.1103/PhysRevLett.31.44

103. Helman JS, Abeles B. Tunneling of Spin-Polarized Electrons and Magnetoresistance in Granular Ni Films. Phys Rev Lett [Internet]. 1976 Nov 22;37(21):1429–32. Available from: https://link.aps.org/doi/10.1103/PhysRevLett.37.1429

104. Narjis A, kaaouachi A El, Limouny L, Dlimi S, Errai M, Sybous A, et al. Coulomb blockade and magnetoresistance in granular La1.32Sr1.68Mn2O7 under hydrostatic pressure. J Magn Magn Mater [Internet]. 2013;332:6–9. Available from: https://www.sciencedirect.com/science/article/pii/S0304885312009766

105. Grünberg P, Schreiber R, Pang Y, Brodsky MB, Sowers H. Layered Magnetic Structures: Evidence for Antiferromagnetic Coupling of Fe Layers across Cr Interlayers. Phys Rev Lett [Internet]. 1986 Nov 10;57(19):2442–5. Available from: https://link.aps.org/doi/10.1103/PhysRevLett.57.2442

106. Fert A, Grünberg P, Barthélémy A, Petroff F, Zinn W. Layered magnetic structures: interlayer exchange coupling and giant magnetoresistance. J Magn Magn Mater [Internet]. 1995 Feb;140–144:1–8. Available from: https://linkinghub.elsevier.com/retrieve/pii/0304885394008809

107. Hirota E, Sakakima H, Inomata K. Giant Magneto-Resistance Devices [Internet]. Berlin, Heidelberg: Springer Berlin Heidelberg; 2002. (Springer Series in Surface Sciences; vol. 40). Available from: http://link.springer.com/10.1007/978-3-662-04777-4

108. Weiss R, Mattheis R, Reiss G. Advanced giant magnetoresistance technology for measurement applications. Meas Sci Technol [Internet]. 2013 Aug 1;24(8):082001. Available from: https://iopscience.iop.org/article/10.1088/0957-0233/24/8/082001

109. Reig C, Cubells-Beltrán M-D, Ramírez Muñoz D. Magnetic Field Sensors Based on Giant Magnetoresistance (GMR) Technology: Applications in Electrical Current Sensing. Sensors [Internet]. 2009 Oct 12;9(10):7919–42. Available from: http://www.mdpi.com/1424-8220/9/10/7919

110. Von Helmolt R, Wecker J, Holzapfel B, Schultz L, Samwer K. Giant negative magnetoresistance in perovskitelike La2/3Ba1/3MnOx ferromagnetic films. Phys Rev Lett [Internet]. 1993 Oct 4;71(14):2331–3. Available from: https://link.aps.org/doi/10.1103/PhysRevLett.71.2331

111. Baldini M, Muramatsu T, Sherafati M, Mao H, Malavasi L, Postorino P, et al. Origin of colossal magnetoresistance in LaMnO 3 manganite. Proc Natl Acad Sci [Internet]. 2015 Sep 1;112(35):10869–72. Available from: http://www.pnas.org/lookup/doi/10.1073/pnas.1424866112

112. Julliere M. Tunneling between ferromagnetic films. Phys Lett A [Internet]. 1975;54(3):225–6. Available from: https://www.sciencedirect.com/science/article/pii/0375960175901747

113. Miyazaki T, Tezuka N. Giant magnetic tunneling effect in Fe/Al2O3/Fe junction. J Magn Magn Mater [Internet]. 1995;139(3):L231–4. Available from: https://www.sciencedirect.com/science/article/pii/0304885395900012

114. Chappert C, Fert A, Van Dau FN. The emergence of spin electronics in data storage. Nat Mater [Internet]. 2007 Nov;6(11):813–23. Available from: http://www.nature.com/articles/nmat2024

115. Kimura T, Tomioka Y, Kuwahara H, Asamitsu A, Tamura M, Tokura Y. Interplane Tunneling Magnetoresistance in a Layered Manganite Crystal. Science (80-) [Internet]. 1996 Dec 6;274(5293):1698–701. Available from: https://www.sciencemag.org/lookup/doi/10.1126/science.274.5293.1698

116. Kimura T, Asamitsu A, Tomioka Y, Tokura Y. Pressure-Enhanced Interplane Tunneling Magnetoresistance in a Layered Manganite Crystal. Phys Rev Lett [Internet]. 1997 Nov 10;79(19):3720–3. Available from: https://link.aps.org/doi/10.1103/PhysRevLett.79.3720

117. J. Zhang, Q. Yan, F. Wang PY and PZ. No Title. J Phys Condens Matter. 2001;13:917–927.

118. Zheng L, Lu Y, Zhao J-J, Zhang X-Q, Xing R, Wu H-Y, et al. Magnetic and transport properties of Dy substituted layered perovskite La 1.3 Sr 1.7 Mn 2 O 7. Chinese Phys B [Internet]. 2010 Dec;19(12):127501. Available from: https://iopscience.iop.org/article/10.1088/1674-1056/19/12/127501

119. Oseroff S, Torikachvili M, Singley J, Ali S, Cheong S. Evidence for collective spin dynamics above the ordering temperature. Phys Rev B - Condens Matter Mater Phys [Internet]. 1996 Mar 1;53(10):6521–5. Available from: https://link.aps.org/doi/10.1103/PhysRevB.53.6521

120. Oseroff SB. Magnetic susceptibility and EPR measurements in concentrated spin-glasses: Cd1-xMnxTe and Cd1-xMnxSe. Phys Rev B [Internet]. 1982 Jun 1;25(11):6584–94. Available from: https://link.aps.org/doi/10.1103/PhysRevB.25.6584

121. en.wikipedia.org.

122. Hwang HY, Cheong SW, Radaelli PG, Marezio M, Batlogg B. Lattice effects on the magnetoresistance in doped LaMnO3. Phys Rev Lett [Internet]. 1995 Jul 31;75(5):914–7. Available from: https://link.aps.org/doi/10.1103/PhysRevLett.75.914

123. Sharma N, Nigam AK, Pinto R, Venkataramani N, Prasad S, Chandra G, et al. Giant magnetoresistance studies on La(0.8−x)RxSr0.2MnO3 thin films (R Pr, Nd, Gd, Ho). J Magn Magn Mater [Internet]. 1997;166(1):65–70. Available from: https://www.sciencedirect.com/science/article/pii/S0304885396004507

124. Fontcuberta J, Martínez B, Seffar A, Piñol S, García-Muñoz JL, Obradors X. Chemical tuning of the colossal magnetoresistance of ferromagnetic perovskites. Europhys Lett [Internet]. 1996;34(5):379–84. Available from: http://dx.doi.org/10.1209/epl/i1996-00467-y

125. Thomas RM, Ranno L, Coey JMD. Transport properties of (Sm0.7A0.3)MnO3 (A=Ca2+,Sr2+,Ba2+,Pb2+). J Appl Phys [Internet]. 1997 Apr 15;81(8):5763–5. Available from: http://aip.scitation.org/doi/10.1063/1.364719

126. García-Muñoz JL, Fontcuberta J, Suaaidi M, Obradors X. Bandwidth narrowing in bulk magnetoresistive oxides. J Phys Condens Matter [Internet]. 1996;8(50):L787–93. Available from: http://dx.doi.org/10.1088/0953-8984/8/50/003

127. Mahendiran R, Tiwary S, Raychaudhuri A, Ramakrishnan T, Mahesh R, Rangavittal N, et al. Structure, electron-transport properties, and giant magnetoresistance of hole-doped systems. Phys Rev B - Condens Matter Mater Phys [Internet]. 1996 Feb 1;53(6):3348–58. Available from: https://link.aps.org/doi/10.1103/PhysRevB.53.3348

128. Blasco J, García J, de Teresa J, Ibarra M, Perez J, Algarabel P, et al. Structural, magnetic, and transport properties of the giant magnetoresistive perovsk. Phys Rev B - Condens Matter Mater Phys [Internet]. 1997 Apr 1;55(14):8905–10. Available from: https://link.aps.org/doi/10.1103/PhysRevB.55.8905

129. Shannon RD. Revised effective ionic radii and systematic studies of interatomic distances in halides and chalcogenides. Acta Crystallogr Sect A [Internet]. 1976 Sep 1;32(5):751–67. Available from: http://scripts.iucr.org/cgi-bin/paper?S0567739476001551

130. http://jana.fzu.cz/.

131. Lee S-H, Seo J, You K-S, Nam S-Y, Ahn J-W. Calcium Ion Extraction from Blast Furnace Slags for the Synthesis of Pure Calcium Carbonate Polymorphs by Accelerated Carbonation. In: Proceedings of the 5th Asian Particle Technology Symposium [Internet]. Singapore: Research Publishing Services; 2012. p. 509–26. Available from: http://rpsonline.com.sg/proceedings/9789810725181/html/359.xml

132. Li JQ, Jin CQ, Zhao HB. Structural and physical properties of double-layered manganites La2-2xCa1+2xMn2O7 with 0.5≤x≤1.0. Phys Rev B - Condens Matter Mater Phys [Internet]. 2001 Jun 19;64(2):204051–4. Available from: https://link.aps.org/doi/10.1103/PhysRevB.64.020405

133. Reddy YS. Electrical transport and magnetoresistance of double layered CMR manganites R 1.2 Sr 1.8 Mn 2 O 7 (R = La, Pr, Sm). Mater Sci [Internet]. 2017 Jul 26;35(2):440–6. Available from: https://www.sciendo.com/article/10.1515/msp-2017-0048

134. Mahamdioua N, Amira A, Altintas SP, Varilci A, Terzioglu C. Structural and magnetotransport properties of the Y doped A-site deficient double layered manganites La1.2−x□0.2YxCa1.6Mn2O7. J Solid State Chem [Internet]. 2016;240:1–8. Available from: https://www.sciencedirect.com/science/article/pii/S0022459616301827

135. LUO G, LIU G, LI X, XIONG W, WU X. Structure and transport properties of (La1-x-yYy)2/3Ca1/3MnO3 with La-site vacancies. Trans Nonferrous Met Soc China [Internet]. 2007 Oct;17(5):992–5. Available from: https://linkinghub.elsevier.com/retrieve/pii/S1003632607602131

136. P Debye PS. Interference of irregularly oriented particles in x-rays. Phys Ziet. 1916;17:277–83.

137. Soylu Koc N, Altintas SP, Mahamdioua N, Terzioglu C. Cation size mismatch effect in (La1-yREy)1.4Ca1.6Mn2O7 perovskite manganites. J Alloys Compd [Internet]. 2019;797:471–6. Available from: https://www.sciencedirect.com/science/article/pii/S0925838819317438

138. Kozhina G, Mitrofanov V, Fedorova O, Fetisov A, Murzakaev A, Estemirova S. Grain growth kinetics, microstructure and magnetic properties of mechanically activated

Nd1−xCaxMnO3±δ manganites. J Alloys Compd [Internet]. 2021;864:158816. Available from: https://www.sciencedirect.com/science/article/pii/S0925838821002231

139. Moritomo Y, Kuwahara H, Tomioka Y, Tokura Y. Pressure effects on charge-ordering transitions in Perovskite manganites. Phys Rev B [Internet]. 1997 Mar 15;55(12):7549–56. Available from: https://link.aps.org/doi/10.1103/PhysRevB.55.7549

140. Guidara K, Dhahrp E, Joubert JC. X-ray diffraction, electrical and magnetic studies of solid solution La 0.6 Sr 0.4 MnO 3-δ □ δ (0.0 ≤ δ ≤ 0.2). Phase Transitions [Internet]. 1999 May 19;68(4):607–19. Available from: http://www.tandfonline.com/doi/abs/10.1080/01411599908224537

141. Abdelmoula N, Dhahri J, Guidara K, Dhahri E, Joubert JC. The effect of a cation radii on physical properties of doped manganites. Phase Transitions [Internet]. 1999 Dec 1;70(3):197–210. Available from: https://doi.org/10.1080/01411599908240684

142. Dhahri N, Dhahri A, Dhahri J, Hlil E, Dhahri E. Structure, magnetic and electrical transport properties of the perovskites La067−xEuxSr033MnO3. J Magn Magn Mater [Internet]. 2013;129–37. Available from: http://inis.iaea.org/search/search.aspx?orig_q=RN:44109606

143. Zhou T-J, Yu Z, Du YW. Large low-field magnetoresistance of a two-layered La2−2xCa1+2xMn2O7 polycrystal. Phys Lett A [Internet]. 2001;282(3):209–14. Available from: https://www.sciencedirect.com/science/article/pii/S0375960101001827

144. Venkataiah G, Prasad V, Venugopal Reddy P. Influence of A-site cation mismatch on structural, magnetic and electrical properties of lanthanum manganites. J Alloys Compd [Internet]. 2007 Feb;429(1–2):1–9. Available from: https://linkinghub.elsevier.com/retrieve/pii/S0925838806003781

145. Rodriguez-Martinez LM, Attfield JP. Cation disorder and size effects in magnetoresistive manganese oxide perovskites. Phys Rev B [Internet]. 1996 Dec 1;54(22):R15622–5. Available from: https://link.aps.org/doi/10.1103/PhysRevB.54.R15622

146. Rodriguez-Martinez LM, Attfield JP. Cation disorder and the metal-insulator transition temperature in manganese oxide perovskites. Phys Rev B - Condens Matter Mater Phys [Internet]. 1998 Aug 1;58(5):2426–9. Available from: https://link.aps.org/doi/10.1103/PhysRevB.58.2426

147. Vanitha P V., Arulraj A, Santhosh PN, Rao CNR. Effect of Cation Size and Disorder on the Structure and Properties of the Rare Earth Cobaltates, Ln 0.5 A 0.5 CoO 3 (Ln = Rare Earth, A = Sr, Ba). Chem Mater [Internet]. 2000 Jun;12(6):1666–70. Available from: https://pubs.acs.org/doi/10.1021/cm990268t

148. Moritomo Y, Maruyama Y, Akimoto T, Nakamura A. Metal-insulator transition in layered manganites. Phys Rev B - Condens Matter Mater Phys [Internet]. 1997 Sep 15;56(12):R7057–60. Available from: https://link.aps.org/doi/10.1103/PhysRevB.56.R7057

149. Wang K, Song W, Yu T, Zhao B, Pu M, Sun Y. Colossal Magnetoresistance in Fine Particle of Layered-Perovskite La2—2xCa1+2xMn2O7 (x = 0.3) Synthesized at Low Temperatures. Phys status solidi [Internet]. 1999 Feb;171(2):577–82. Available from: https://onlinelibrary.wiley.com/doi/10.1002/(SICI)1521-396X(199902)171:2%3C577::AID-PSSA577%3E3.0.CO;2-0

150. Asano H, Hayakawa J, Matsui M. Two-dimensional ferromagnetic ordering and magnetoresistance in the layered perovskite. Phys Rev B - Condens Matter Mater Phys [Internet]. 1997 Sep 1;56(9):5395–403. Available from: https://link.aps.org/doi/10.1103/PhysRevB.56.5395

151. Chatterjee S, Chou P, Chang C, Hong I, Yang H. Lattice effects on the transport properties of Eu, and Pr). Phys Rev B - Condens Matter Mater Phys [Internet]. 2000 Mar 1;61(9):6106–13. Available from: https://link.aps.org/doi/10.1103/PhysRevB.61.6106

152. Laffez P, Tendeloo G Van, Seshadri R, Hervieu M, Martin C, Maignan A, et al. Microstructural and physical properties of layered manganites oxides related to the magnetoresistive perovskites. J Appl Phys [Internet]. 1996 Nov 15;80(10):5850–6. Available from: http://aip.scitation.org/doi/10.1063/1.363578